Index

Summary

Neutral beam injection is considered one of the most effective methods for plasma heating and current drive in fusion experiments around the world. The concept is straightforward: neutral atoms can penetrate through the confining magnetic field and, via collisions with plasma particles can heat the plasma and transfer momentum to sustain the plasma current.

ITER, the first fusion experimental reactor under construction in Cadarache, will be equipped with two Neutral Beam Injectors, each of them capable to inject into the plasma up to 16.5 MW, by accelerating negative hydrogen or deuterium ions up to energy of 1MeV. The thesis deals with the design the electrostatic accelerator of the ITER Neutral Beam Injector (NBI).

In particular, the thesis focuses on charged particle dynamics for multiple beams modelling, on the issues related to 1 MV dc insulation in vacuum, on the structural behaviour of brittle insulators. Finally, an active steering concept is introduced and its performance and technological issues are discussed.

An overview on the physics principles behind the operation of the existing ion sources is given in chapter one, as well as a discussion on the need of negative ions to produce a high energy and high power neutral beam. The electrostatic accelerator, which generates the high energy ion beam, is the second subsystem inside the NBI: chapter two discusses the main criteria adopted to design it and presents how different issues are reciprocally integrated its design.

Chapter three reports on the structural verification that has been carried out on the large ceramic insulator rings; in particular the R&D activities related to the fabrication of the large alumina insulator rings used for the bushing of the NBI will be presented. A statistical approach has been applied to evaluate the failure probability of the rings during the brazing procedure.

Chapter four explains results obtained on negative ion beam simulation. A Monte Carlo Code has been applied to benchmark the experimental results obtained by the Japanese facility; moreover, a new code to evaluate beam divergence is presented.

Finally, Chapter five presents a conceptual design of an Electron Dump & Steering System (EDSS). This subsystem is aimed to filter the electrons that are accelerated together with the negative ions by the electrostatic accelerator; moreover it should deflect the ions in order to deposit the NB power in different plasma regions. Two possible solutions have been analysed; for one of them, a deterministic approach to evaluate the heat flux deposited on the surfaces has been developed and implemented in an ANSYS® routine.

The EDSS study can be considered as the last step of a virtual travel inside the NBI electrostatic accelerator where the conversion of electrical power into kinetic power takes place.

Sommario

Il riscaldamento mediante fasci di neutri è considerato uno dei più efficaci metodi di riscaldamento e sostentamento della corrente nei plasmi fusionistici di molti esperimenti mondiali. Il concetto è semplice: gli atomi neutri possono penetrare il campo magnetico, mediante collisioni con le particelle cariche, è possibile riscaldare il plasma e sostenerne la corrente.

ITER, il primo reattore sperimentale in fase di costruzione a Cadarache, sarà equipaggiato con due iniettori di neutri; ciascuno di essi sarà in grado di trasferire all'interno del plasma di ITER fino a 16.5 MW di potenza mediante l'accelerazione di ioni negativi di idrogeno o deuterio fino ad energie di 1MeV. Questa Tesi tratta il progetto di dispositivi inerenti la tenuta delle alte tensioni in vuoto per l'acceleratore elettrostatico dell'iniettore di neutri per ITER. In particolare, la Tesi si focalizza sulle problematiche legate alla modellistica dei fasci di particelle carichi, sui problemi legati all'isolamento delle alte tensioni in vuoto e sulle analisi strutturali relative ai materiali fragili per gli isolatori ceramici. Infine, un sistema attivo per la deflessione delle particelle cariche verrà presentato e discusso assieme agli aspetti tecnologici che lo riguardano.

Una panoramica dei principi fisici che governano le sorgenti a ioni negativi è fornita nel Capitolo 1 evidenziando la necessità di produrre un fascio di neutri ad alta energia e potenza. L'acceleratore elettrostatico, disposto a valle della sorgente, incrementa l'energia degli ioni negativi fino ad 1MV: il Capitolo 2 discute i principali criteri progettuali sottolineando l'interconnessione tra problemi fisici ed ingegneristici.

Il Capitolo 3 riporta le verifiche strutturali svolte sugli anelli isolatori di grandi dimensioni in materiale ceramico; in particolare verranno presentate le attività di ricerca e sviluppo riguardanti la fabbricazione degli isolatori di allumina per il passante multistadio dell'iniettore di neutri. Inoltre si è sviluppata una metodologia per calcolare la probabilità di rottura durante il processo di fabbricazione di tali isolatori.

Il Capitolo 4 spiega i risultati riguardanti le simulazioni del fascio di ioni negativi, un codice Monte Carlo è stato applicato per confrontare i risultati sperimentali, ottenuti da un acceleratore giapponese, con quanto stimato dai modelli numerici; inoltre sarà presentato nello stesso capitolo un nuovo codice in grado di calcolare la divergenza del fascio di ioni negativi considerando il problema della carica spaziale.

Infine il Capitolo 5 presenta uno studio concettuale di un dispositivo che è in grado di filtrare gli elettroni dal fascio di ioni negativi e contemporaneamente curvare leggermente la traiettoria di

quest’ultimi (EDSS). Due possibili alternative si sono studiate; per una di esse si è sviluppata, ed applicata, una routine ANSYS per il calcolo del flusso di potenza depositato sulle superfici materiali del EDSS mediante un approccio deterministico.

Lo studio del EDSS può essere considerato l’ultimo passo di un viaggio virtuale all’interno dell’acceleratore elettrostatico dell’iniettore di neutri in cui l’energia elettrica viene convertita in energia cinetica di un flusso di particelle cariche.

Introduction

Nowadays, more than in every other moment of our history, secure and sustainable energy sources are required for the development of humankind. As a consequence, researchers from all over the world are working to develop a range of environmentally acceptable, safe and sustainable energy technologies. Nuclear fusion is one of them. Nuclear fusion is the process that powers the sun and other stars - providing heat and light to sustain life on the Earth. While gravity confines the hot plasma in the stars, on the earth strong magnetic fields can be used to hold the plasma inside a chamber (magnetic confinement approach). To harness fusion power, light nuclei are forced together, undergoing reactions that produce a net energy gain. In order to make fusion happen (fig.1), the fuel has to be heated up to very high temperatures (in the order of 100 million degrees).

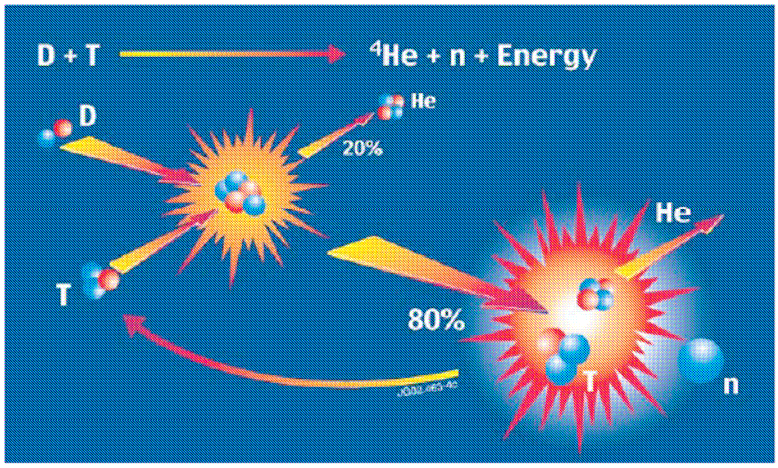

Figure 1 The basic physical process of the fusion reaction D+T [1]

The hot plasma produced in the fusion reactor should be confined and insulated in order to maintain the high temperature necessary to obtain a significant amount of fusion reactions. Magnetic confinement is one of two major branches of fusion energy research, the other being inertial confinement. The magnetic approach is more developed and is usually considered more promising for energy production.

The “Tokamak” has been so far the most successful concept of toroidal machines to confine fusion plasmas. Alternative concepts, like Reversed Field Pinch and Stellarator, are also developed to prepare for fusion power plants.

The primary fuels for nuclear fusion are deuterium and lithium: the need to use lithium comes from the absence of tritium on the earth so the following reactions could be used to obtain it inside the fusion reactor:

$$^{6}Li + n \rightarrow T + {}^{4}He + 7.7 \cdot 10^{-13} \qquad joule$$

$$^{7}Li + n \rightarrow T + {}^{4}He + n + 4.0 \cdot 10^{-13} \qquad joule$$

Figure 2 The reactions for tritium production [28]

Deuterium can be extracted from sea water and lithium is abundant in the earth's upper crust. In a power plant, lithium is used to breed tritium which fuses together with deuterium. Only 150 kg of deuterium and 2÷3 tonnes of lithium are needed for a full year of electricity supply for one million persons.

Fusion power plants will be particularly suited for base load energy generation to serve the needs of densely populated areas and industrial zones. They can also produce hydrogen for a "hydrogen economy". ITER is an international tokamak research project which is intended to be a key intermediate step between today's machines, aimed at studies of plasma physics, and future electricity-producing fusion power plants. It will build upon the results of research conducted with magnetic fusion devices built across the world in the last three decades and will be considerably larger than any of them.

On November 21st, 2006, seven parties (EU, USA, Japan, Russia, China, India, and Korea) formally agreed to fund the ITER project. The program is anticipated to last for about 30 years − 10 years for construction, and 20 years of operation − and cost approximately 10 billion Euro, which makes it one of the most expensive and ambitious modern technoscientific projects. It will be biult in Cadarache, France. It is technically ready to start construction and the first plasma operation is expected in 2018. The main goal is to produce approximately 500 MW of fusion power, sustained for up to 400 seconds (compared to a peak of 16 MW for less than a second obtained so far in the largest operating Tokamak, JET, in Culham, UK) by the fusion of about 0.5 g of deuterium/tritium mixture in its approximately 840 m^3 reactor chamber. ITER is the acronym for International Thermonuclear Experimental Reactor, but it also means "trail" or "path"in Latin, and this double meaning reflects ITER's role in harnessing nuclear fusion as a peaceful power source.

ITER will operate as a power amplifier, with a gain up to 10. It is thus necessary to provide a power in the range 50-70 MW to heat the plasma at the start, to sustain the burn and to drive the plasma current.

The Heating and Current Drive (H&CD) systems for ITER are an appropriate combination of Neutral Beam Injectors (NBI) and Radio Frequency (RF) H&CD antennas operating at the electron cyclotron (EC) and ion cyclotron (IC) frequency (see Figure 3).

They aim at providing an active control on all the key phases of the operating scenarios:

• the plasma temperature rise, while density is increased to obtain the requisite fusion power,

• the achievement of a steady burn,

• the control of the excursions around the operating point,

• the suppression of instabilities, and

• the achievement of a soft termination at the end of burn.

The neutral beam system consists at present of two heating and current drive (H&CD) injectors (being possible an upgrade to a third injector) and one diagnostic neutral beam (DNB) injector. Each H&CD injector will deliver a deuterium beam of 16.5 MW (total 33 MW), with energy of 1MeV, and will be able to operate for long pulses (up to 3600 s for “steady state” operation).

In order to realize an efficient and reliable Neutral Beam Injector (NBI) for ITER, a large amount of research & development, both on physics and engineering sides it is required. For this reason, a Neutral Beam Test Facility is foreseen to be built in Padova. The facility has the goal to address and solve the main physics and engineering issues related to this system.

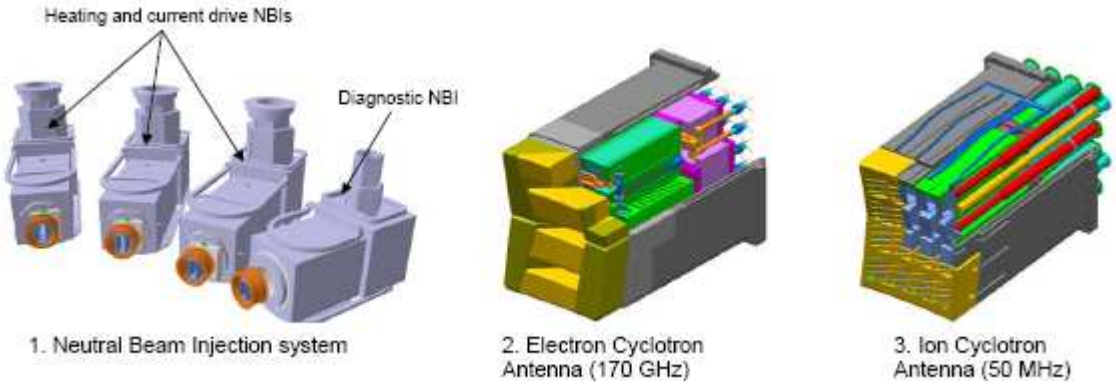

Figure 3 Overview of the Heating & Current Drive systems [3].

This thesis is focused on the design of the high voltage accelerator and addresses a range of design issues.

An overview on the physics principles behind the operation of the existing ion sources is given in chapter one, as well as a discussion on the need of negative ions to produce a high energy and high power neutral beam. The electrostatic accelerator, which generates the high energy ion beam, is the second subsystem inside the NBI: chapter two discusses the main criteria adopted to design it and presents how different issues are reciprocally integrated its design.

Chapter three reports on the structural verification that has been carried out on the large ceramic insulator rings; in particular the R&D activities related to the fabrication of the large alumina insulator rings used for the bushing of the NBI will be presented. A statistical approach has been applied to evaluate the failure probability of the rings during the brazing procedure.

Chapter four explains results obtained on negative ion beam simulation. A Monte Carlo Code has been applied to benchmark the experimental results obtained by the Japanese facility; moreover, a new code to evaluate beam divergence is presented.

Finally, Chapter five presents a conceptual design of an Electron Dump & Steering System (EDSS). This subsystem is aimed to filter the electrons that are accelerated together with the negative ions by the electrostatic accelerator; moreover it should deflect the ions in order to deposit the NB power in different plasma regions. Two possible solutions have been analysed; for one of them, a deterministic approach to evaluate the heat flux deposited on the surfaces has been developed and implemented in an ANSYS® routine.

The EDSS study can be considered as the last step of a virtual travel inside the NBI electrostatic accelerator where the conversion of electrical power into kinetic power takes place.

Chapter 1: Framework of the PhD activities, the Neutral Beam Injector for ITER

1.1 Neutral beam heating principles

High power neutral beams for heating high temperature plasmas are required to develope controlled thermonuclear fusion as an energy source. The ion sources used for such Neutral Beam Injection (NBI) systems are characterized by high energy (several hundred keV) and high current (several tens of A), and consequently by high power (several tens of MW). The term ion source in this thesis indicates the ensemble of:

1. A plasma source, where the plasma is generated;
2. An extractor, where the ions are extracted from the plasma by means of an electric potential, forming an ion beam;
3. An accelerator, where the ion beam is accelerated.

This terminology is in agreement with most of the literature, since the early times of research activities on this topic. Nevertheless, in some documents the assembly here introduced is referred to as “beam source” while the term “ion source” indicates only the plasma source.

The injected beam energy is tuned on the expected penetration depth inside the target plasma, which depends on the plasma density. Beam energy has increased from about 20 keV for the first experiments on injection into magnetically confined plasmas in 1974 up to about 500 keV at present, as the target plasma size and temperature have become larger and larger. In a future fusion reactor the beam energy would be up to 2 MeV.

The neutrals are created by a charge-exchange conversion from an ion beam, but at higher energies, above 100 keV, the neutralization efficiency for positive ions decreases drastically while remaining at around 60% for negative ions [7].

Thus large scale, positive ion sources were developed in the 70s and 80s when the required beam energy was below 80 keV, followed by negative ion source development for the high energy NBI system aimed at reactor-sized fusion machines.

In the following, a short summary of the theory of neutral beam heating and the technical background of neutral beam generation is given.

The characteristics of an ion beam are determined by the ion source plasma and the accelerator. Thus, for example, the ion beam current is determined by the plasma density, the plasma electron temperature, the extraction voltage and the extractor geometry. The beam emittance is determined

by the plasma density distribution, the plasma ion temperature and the extraction geometry. The beam composition is clearly determined by the composition of the plasma. The physics of the ion source is thus largely plasma physics.

The production of a neutral beam and its dynamics are best understood by subdividing the processes into successive steps, as shown in Figure 4:

• Generation of a powerful ion beam;

• Neutralization of the ion beam;

• Propagation of the neutral beam to the main plasma.

The generation of a powerful ion beam is generally accomplished in a very well known way mutuated from accelerators in atomic and nuclear physics: positive or negative hydrogen ions are electrostatically extracted from a suitable plasma source and accelerated to energies of several tens of kV. The essential difference to accelerator beams is the much higher beam current (tens of amperes) necessary to achieve the required power (several MW) and consequently the much larger beam cross sections (several thousands of cm^2). This extrapolation from the level of milliamperes to tens of amperes, while maintaining a reasonable beam quality, has been obtained as a consequence of a number of distinct achievements:

• The generation of large-area, uniform, quiescent plasmas for ion extraction (arc and RF sources);

• The subdivision of the beam into many beamlets by using electrodes with multiple apertures;

• The discovery of simple ways of controlling the direction of individual beamlets in order to yield the desired overall beam focal properties;

• The development of the technical means of cooling and protecting the delicate electrodes against high voltage breakdowns.

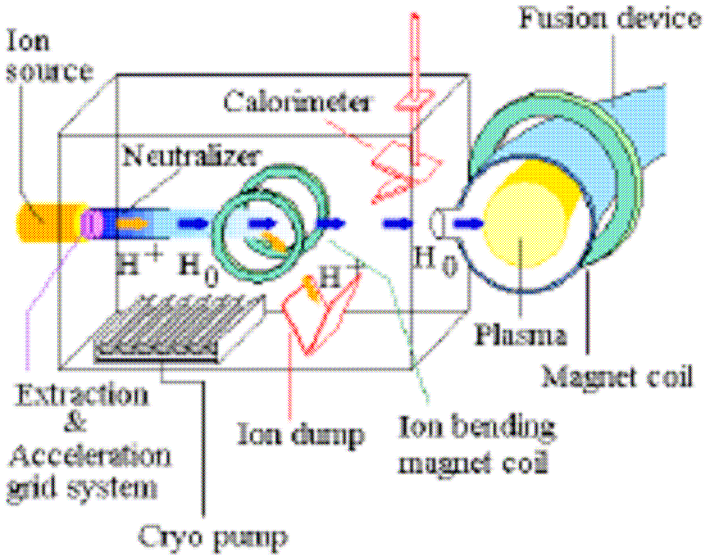

Figure 4 Neutral beam generation and scheme [6]

Charge neutralization of the ions occurs by charge-exchanging collisions of the fast ions with the neutral hydrogen molecules present in the neutralizer. Cold gas is used to create a certain gas target density inside the neutralizer for the conversion of the ions into neutrals.

The interaction of fast neutral atoms with the plasma of ITER includes the following physical processes, the last three of them occurring simultaneously:

• Ionization of the fast neutral atoms by collisions with plasma electrons and ions;

• Drift motion of the fast ions in the magnetic field;

• Collisions of the fast ions with plasma ions and electrons, giving rise to slowing down and scattering;

• Charge exchange collisions of the fast ions with background neutral atoms.

All these processes together determine the local input rates not only of particles and energy (power and particle deposition profiles), but also of toroidal momentum and toroidal current.

1.2 The need of a negative ion beam

Positive ion beams, neutralized by charge-exchange on gas targets, have been used in many experiments to produce the required high power neutral beams. But this is limited to energies below 80-100 keV/nucleon, due to the rapid drop of the charge exchange cross section with energy, while beam energies in the 200-1000 keV/nucleon range are needed in larger fusion devices. One of the inherent limitations of neutral injection, using positive ions, is that the efficiency of the neutralization rapidly drops with increasing beam energy; this aspect will be clarified in sec.1.6 where the neutralizer features will be presented. On the contrary, for the negative ion beam the low binding energy of the additional electron (0.75 eV) enables an easy detachment of this electron, so the neutralization efficiency stays at about 60%, even for the highest energies. Therefore, for larger experiments as ITER, which need energies up to 1 MeV, negative ion beams must be developed.

1.3 The negative ion beam production

The development of negative ion-based systems for fusion is progressing steadily, addressing and solving the issues found when increasing the required performance, and year after year there is an increasing confidence in this promising field: in 1992 the first complete negative ion-based beamline produced 100 kW of 100 keV D_0 beams in the framework of a collaboration between JAERI and CEA, 16 A of H^- were produced at Nagoya in 1994, and 40 mA H^- beams were accelerated to 700 keV at JAERI in 1995 [8]. After these successful small power injectors, large

negative ion-based systems have been installed on the Tokamak JT60-U and on the stellarator LHD, that achieved maximum parameters of 400 keV, 17.4 A and 180 keV, 34.5 A, respectively [9 10 11]. A negative ion-based system with two 1 MeV, 40 MW ion beamlines is proposed for ITER [12,13] . Thus, a large negative ion source current of 40 A is needed: the present design foresees 20 mA/cm2 D^- current density, high performance electrostatic accelerators and efficient neutralizers to convert the D^- beam into D_0. It will be shown that the attractive feature of negative ions, their low electron affinity, is a drawback when production or acceleration is considered: firstly it is difficult to attach this additional electron; secondly many negative ions are destroyed ("stripped") by collisions with plasma or neutral particles before being extracted from the sources or accelerated to the final energy. The present high performance has been obtained in particular from large caesium seeded sources.

The fundamental processes which lead to this kind of negative ion production are well known: surface and volume production. As far as the negative ion production by surface reactions on the plasma grid is concerned, the probability of electron capture during backscattering of hydrogen atoms or ions to the plasma grid depends on the work function of the surface, on the affinity of the electron and also on the velocity of the impacting ions.

$$H, H_n^2 + wall \rightarrow H^- \qquad \textbf{(1)}$$

The negative ion yield per H impact on a wall can be predicted by eq.(2)

$$Y\left(H^-/H\right) = \exp\left(-\frac{\phi - A}{C \cdot v_\perp}\right) \qquad \textbf{(2)}$$

where C is a constant, $v_\perp$ is the perpendicular velocity of the impacting ions to the wall, and $\phi - A$ represents the energy difference between the Fermi level of the surface and the affinity level; it should be as small as possible to enhance the electron capture probability. The most widely used method to lower the surface work function ϕ is to cover a metal with caesium. The optimal amount of caesium was found to be about 0.6 monolayers that corresponds to $3.3 \cdot 10^{14}$ atoms of Cs per cm^2. For tungsten, for example, the work function is reduced from 5.25 eV to 1.45 eV by the introduction of caesium. For the surface conditions which are found in most caesiated sources, the expected yields Y (H−/H) or Y (H−/H+) are in the $10^{-2} \div 10^{-1}$ range, in agreement with experiments. The surface process has been very efficiently used to produce intense negative ion sources.

The volume production is the alternative reaction to produce the negative ions inside the beam source. It is given by a dissociative attachment of electrons to H molecules, described in eq.(3):

$$H_2 + e^- \rightarrow H_0 + H_- \qquad \textbf{(3)}$$

The cross-section of this reaction is enhanced when the hydrogen molecules are in high vibrational states, nevertheless the experimental results show that the introduction of Cs drastically increases the production of the negative ions, so the surface reactions (and the contribution of Cs) are fundamental to obtain the high current required in the neutral beam injectors.

The most common ion sources based on this volume reaction are the "tandem sources", as illustrated in Figure 5. They feature two regions separated by a magnetic filter, the "driver" and the "extraction chamber". The driver contains the arc filaments (tungsten) which emit the primary electrons; H_2 gas is fed into this region. A number of permanent magnets are mounted on the source walls and create the multi-cusp configuration for plasma confinement. Another set of magnets is used to create the magnetic filter near the plasma grid.

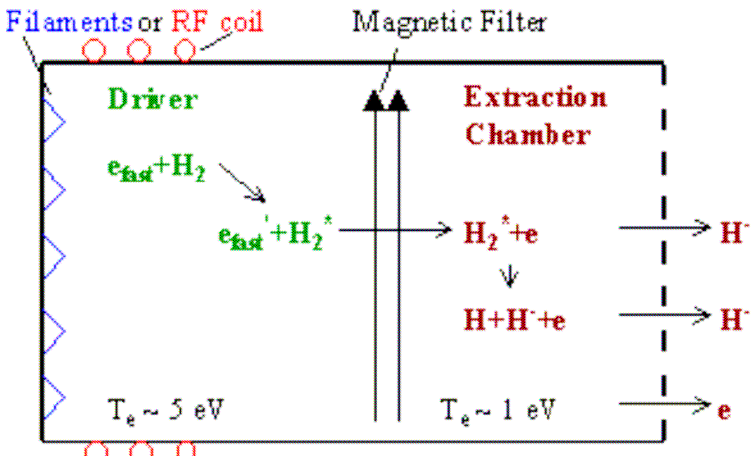

Figure 5 Schematic of a "volume plasma source".

The main limit for negative ion production is the extracted current: in fact, with positive ions the electric field, inside the plasma sheath near the wall, pushes the positive ions toward the wall or toward the holes of the plasma grid. The situation is reversed with negative ions: the electric field acts both on the negative ions and on the electrons hampering the exit of negative charges from the plasma. From the design point of view, this aspect has important consequences on the gap lengths, dimension and number of holes in the grids. Figure 6 compares two grids respectively for positive and negative ion beam, the segments L and L' are comparable. It can be noted that the hole

diameter in the positive ion source is smaller in comparison with the negative one: this aspect will be clarified in section 2.2 where the concept of perveance will be introduced and discussed.

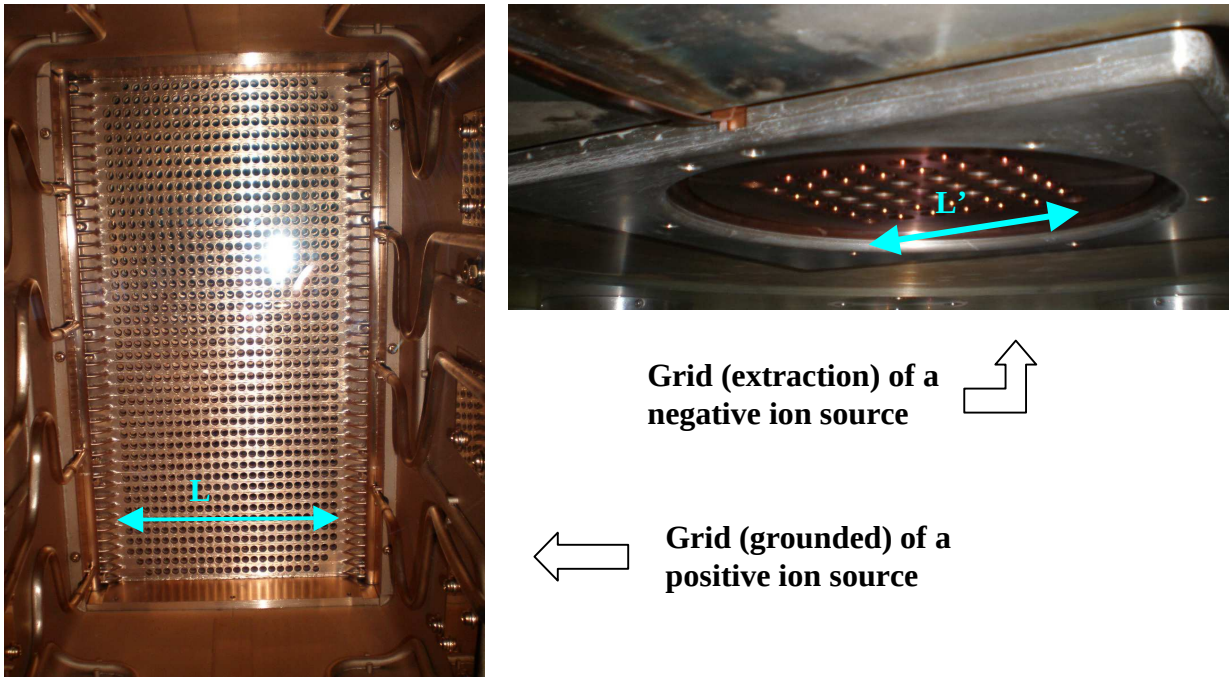

Figure 6 Comparison between the grids of the positive and negative ion source, L≈ L'. Photos kindly supplied by JAEA NBI group.

The "reverse" electric field in the sheath causes further complications in the design of the negative ion source; in order to extract the required negative current, it is necessary to provide a strong magnetic field in front of the plasma grid to filter the electrons from the main plasma; moreover, the plasma grid should be positively polarised with a suitable voltage to repel the positive ions that are present inside the plasma.

Figure 7 shows the negative ion beam extraction and acceleration in a simulation that considers only one beamlet. The plasma source (on the left) is negatively polarized, the grid voltages increase progressively going toward the grounded grid (on the right).

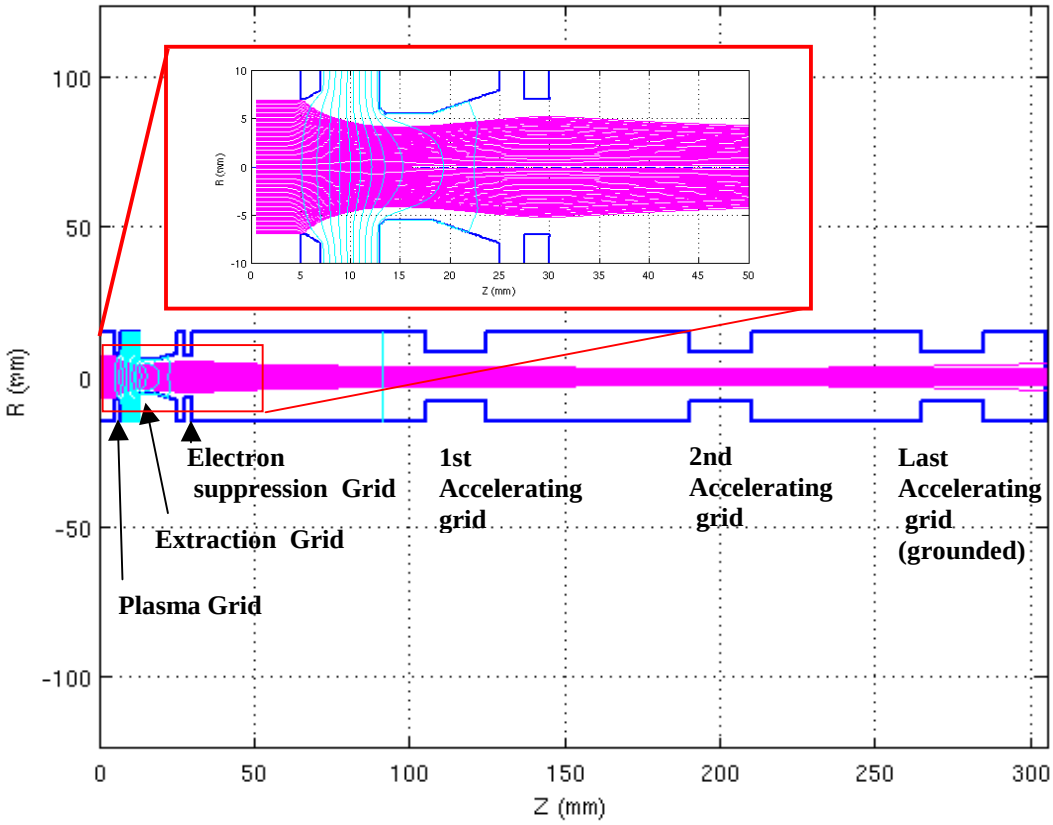

Figure 7 The accelerating grids and the negative ion beam extraction and acceleration

1.4 The two concepts for the NBI Ion Source

The generation of a powerful ion beam first requires a suitable hydrogen plasma source, which should present the following characteristics:

•A typical ion flux density of a few tents of milliamperes per cm^2 over an area of several thousands of cm^2 in order to provide the required tens of amperes per source;

• Sufficient uniformity in space (< 10%);

• Sufficient stability over long pulses (tens of minutes range);

• As high a content of atomic ions as possible;

• A sufficiently low content of impurity ions;

• A reasonable efficiency in term of electric power and hydrogen gas consumption.

When cesium is seeded into the ion sources, the situation changes dramatically [17, 18, 19]:

• The negative ion yield is increased by a factor of 3÷5;

• The stray electron current ratio drops from 10÷100 in pure sources to 1÷5;

• The production of negative ions in Cs seeded ion sources increases linearly with increasing arc or RF power, and no experiment has yet revealed saturation.

There are basically two different concepts: Arc sources and Radio Frequency (RF) sources.

1.4.1 Arc Sources

In an arc discharge, source electrons are emitted from a hot cathode and accelerated by a DC voltage of typically 100 V into the source, where ionization of the gas molecules leads to the desired arc plasma. Numerous configurations, differing in the way of optimizing the ionization efficiency of the fast electrons have evolved over the last 25 years [15]. The arc source (Kamaboko) proposed by the Japanese team for the ITER NBI system foresaw to adopt a cylindrical plasma chamber, several permanent magnets were embedded in the circular wall (see Figure 8) , they were positioned at each azimuthal position in order to confine the plasma inside the source by a multicusp magnetic configuration.

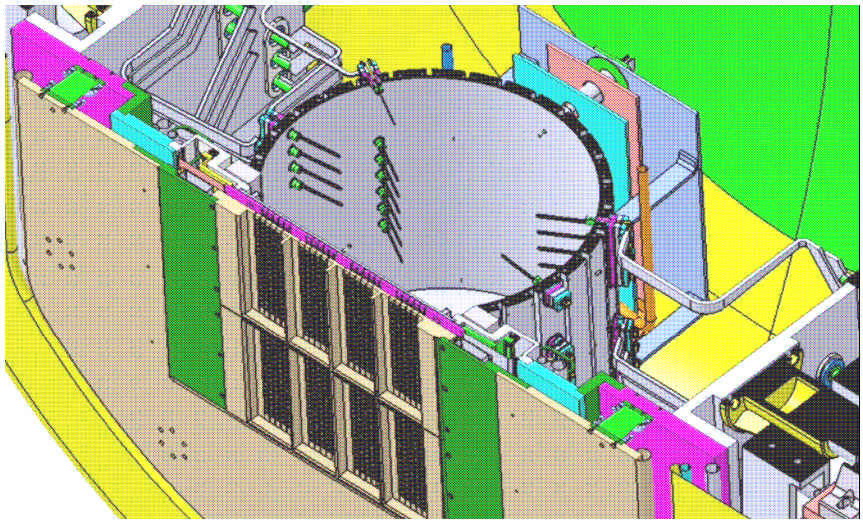

Figure 8 Kamaboko Arc driven source lay-out

1.4.2 RF Sources

The RF source utilizes the oscillating electric field, generally induced by a RF coil, for the necessary acceleration of electrons in order to create the source plasma. A typical frequency for RF sources is 1 MHz, and typical RF powers 100 kW [16]. RF sources have many advantages over the arc sources, such as:

– Long lifetime due to the absence of filaments having a limited thermal cycle time,

– Low cost due to the possibility of electrically insulating the RF generators from the high potential of the plasma source

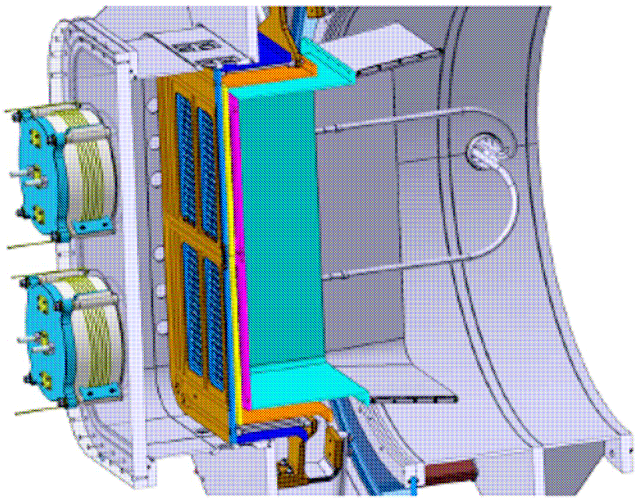

Figure 9 Radio Frequency ion source (overview). [14]

– Better control, during beam modulation, of the extracted ion current due to the fast response of the ion density in the source to changes of the RF input power; this makes active beam current control possible;

– Simplicity of the source (less electrical connections compared to arc sources), making remote handling easier.

Due to these advantages, an RF source has been recently chosen as the reference design for the 1 MeV negative ion injectors of ITER. A picture of a RF ion source is shown in Figure 9.

1.5 Negative ion extraction and acceleration

To get sufficient power efficiency, the large current required for fusion can only be achieved via electrostatic acceleration.

Three steps in acceleration can be distinguished:

• Electrostatic extraction of the ions from the source

• Full energy acceleration by 2 or 5 steps (up to 1 MeV as foreseen for ITER).

Besides the difficulties expected with high voltages, in particular electrical breakdowns with high capacitive energy dissipation, the design requires an in-depth assessment of negative ion extraction and acceleration processes.

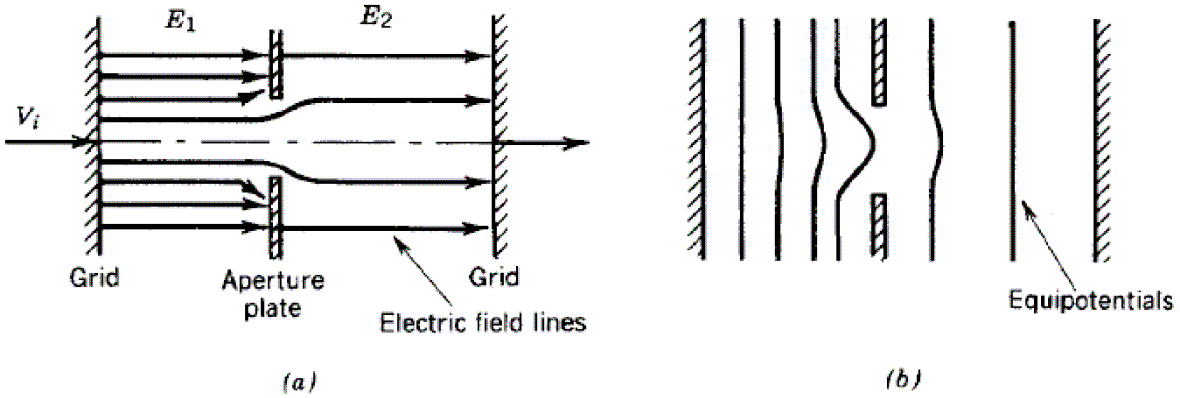

Figure 10 Electrostatic aperture lens, electric field (a) and equipotential lines (b). [20]

The principle that controls electrostatic acceleration and beam focussing can be understood with the aid of Fig.11. The physics describing the accelerated beam has some common points and definitions with geometric optics [20], the hole illustrated in Figure 10 can be compared with a thin lens. The hole is drilled across a plate which separates two regions: the first one has a strong electrostatic field; instead the second one is characterized by an electric field with the same direction but with lower amplitude. The beam extracted from the grid on the left side is accelerated toward the electrode on the right with a defocusing action (see Figure 11)

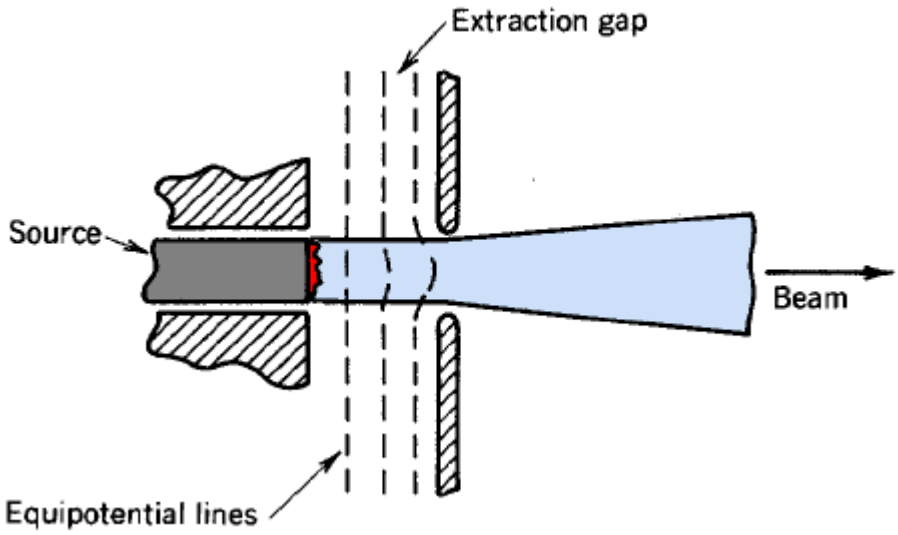

Figure 11 The negative (defocusing) lens [20]

A suitable choice of voltage and gaps between the aperture plates (grids) can be used to focus and to transfer the energy to the extracted beamlet.

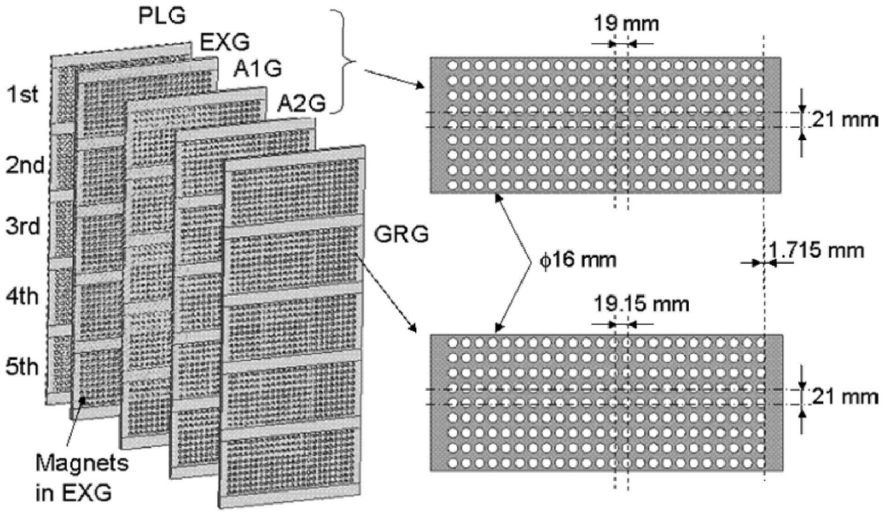

Figure 12 A typical set of accelerating grids [11]

An ion beam is typically composed of several beamlets and each of them is extracted from the ion source separately from the others. This is achieved by assembling a set of carefully aligned grids (see Figure 12), in which cylindrical or conical apertures are drilled. These grids are polarized at various voltages, to achieve the desired beam energy. The geometry of the accelerating channels

and the gaps between the grids are carefully designed to control beam optics. The first grid ("plasma grid") separates the source plasma from the accelerator. In the second grid, often called "extraction grid", permanent magnets are inserted in order to deflect the stray electrons and to prevent them from being further accelerated. This magnetic field breaks the axial symmetry of the acceleration channel.

In Figure 13 the main features that influence the quality of the beam optics are shown, in detail it is possible to distinguish:

1. The perveance effect is related to the influence of spatial charge on the beam divergence
2. The presence of the magnetic field for an accelerated beam implies a permanent deflection of the beam
3. An aperture displacement can deflect the beam path, this effect is particular evident if the displacement concerns the first stages
4. The beamlet-beamlet interaction is mainly due to the spatial charge effect between each beamlet
5. A compensation for the beam aiming can be obtained by a local modification of the equipotential lines, suitable plates can be typically inserted downstream the extraction grid.

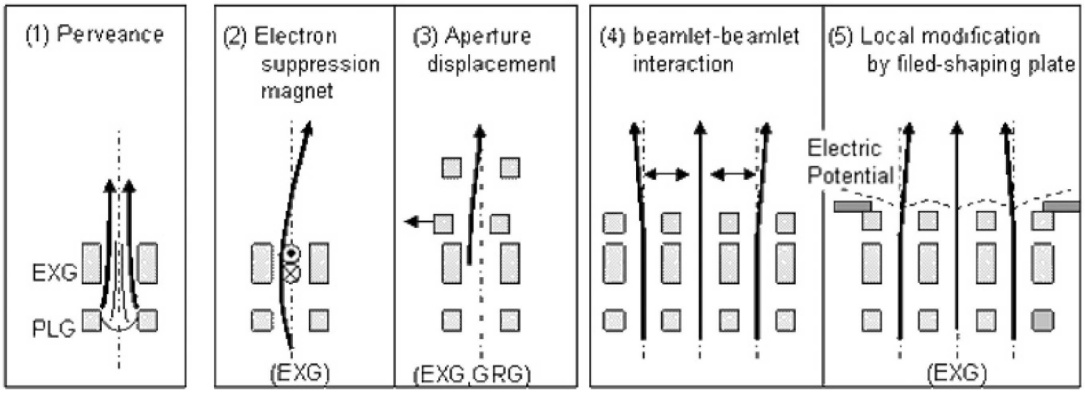

Figure 13 Main causes that influence beam optics [11]

In order to increase the filter field inside the source, a DC current can flow through the plasma grid in the y direction: the superposition of this magnetic field with the field produced by the permanent magnets inside the source and embedded in the extraction grid produces a magnetic field that isn't uniform in space (see Figure 14), resulting a non-uniform beam with aberration. This aspect could lead to deposit the neutral beam power inside the device or in the duct connecting the NBI with the ITER chamber and as a consequence, to decrease the lifetime of the injector reducing the power transferred to the ITER plasma.

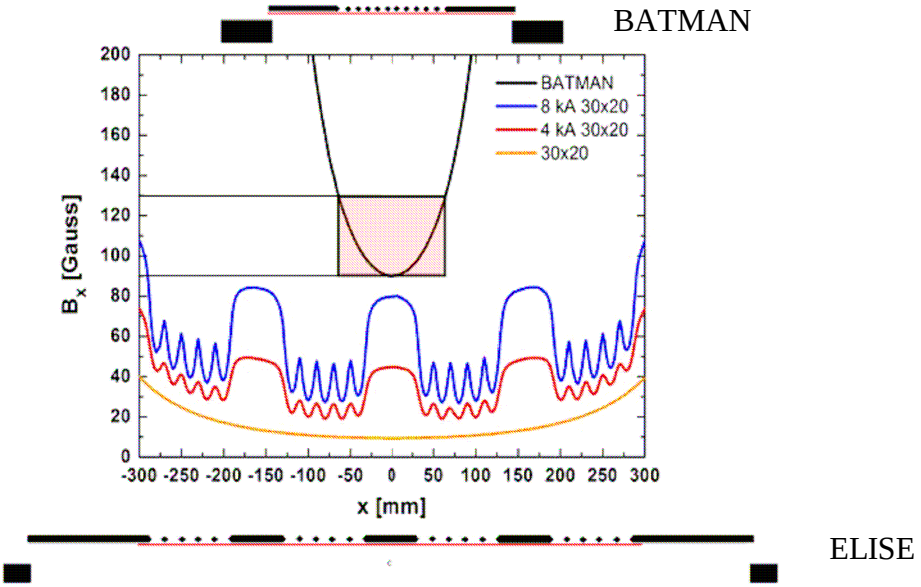

Figure 14 Simulation of the horizontal magnetic field in the extraction area before the plasma grid (along the red lines). The figure compares the magnetic field of BATMAN (only permanent magnets) with the field of ELISE, (the latter is the superposition of the permanent magnets and the current that flows inside the plasma grid) [52]

1.5.1 The two concepts for MeV negative ion acceleration: MAMuG and SINGAP

The development of the accelerator of the ion beam up to energies in the MeV range has a mostly technological nature; it is certainly the major issue today. Two concepts have been considered:

• The reference concept, the “Multi Aperture-MUlti Grid” (MAMuG) accelerator (see Figure 15), accelerates the ions to high voltage in several intermediate steps, each having the same aperture pattern as the plasma and extraction grids. This requires several multi aperture grids at intermediate potentials, the power supplies to feed them and water cooling to each grid. This system stems from positive ion accelerator concepts and features long and narrow acceleration channels from the source to the last acceleration stage.

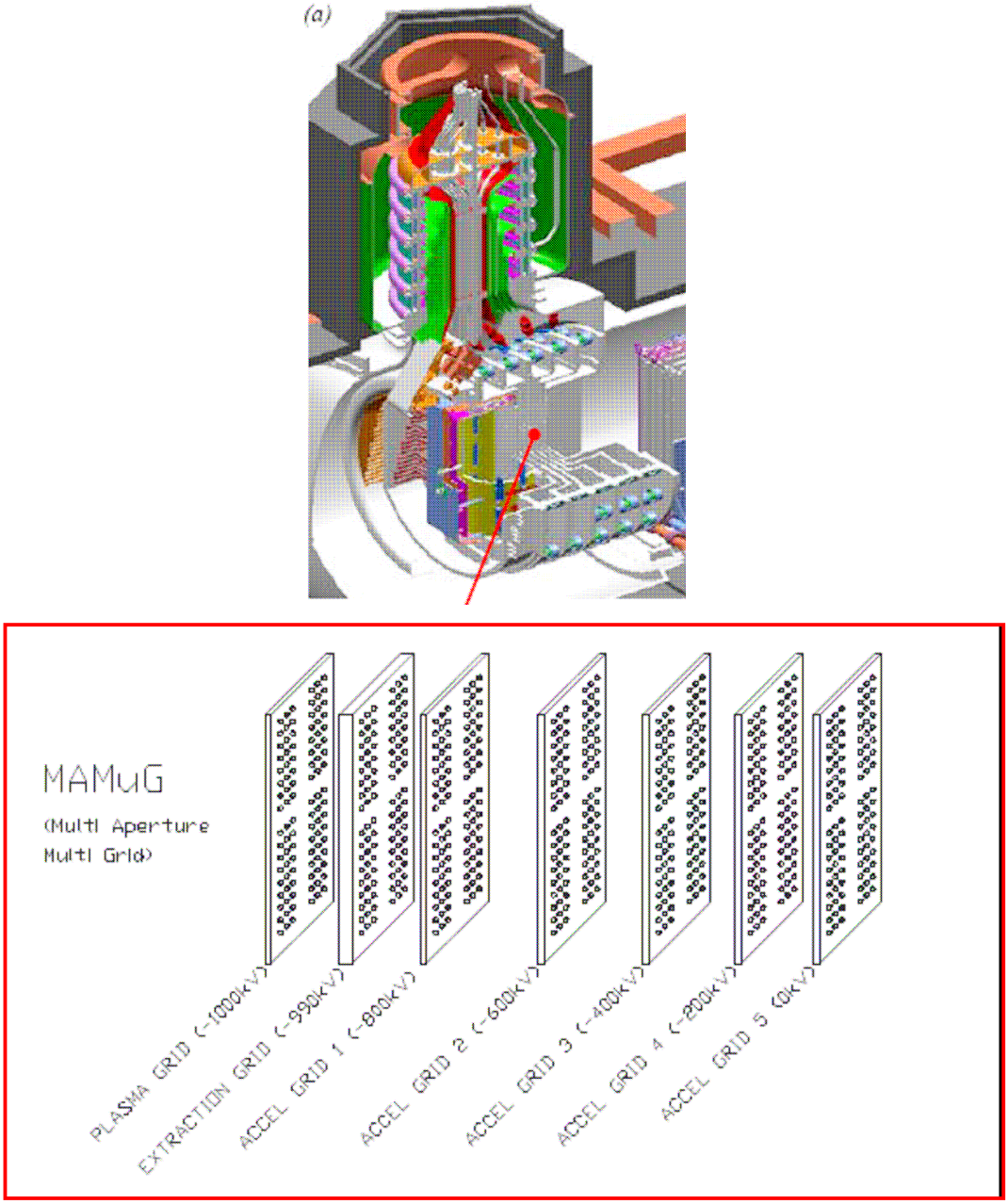

Figure 15 MAMuG grids scheme [29]

• The European alternative concept, the “SINGle Aperture-SINgle GAP” (SINGAP) accelerator (see Figure 16), pre-accelerates the 1280 beamlets to 20-50 keV, and then accelerates them to the final energy in one single step through large apertures in the final (ground potential) electrode [22 23]. SINGAP would allow reducing the gas load in the accelerator and greatly simplifying the design of the accelerator, power supplies, and HV transmission lines, but some difficult issues should be faced: the high voltage generation (in the class of 1MV accelerators) by a single gap device is nowadays the main problem related to the technical aspects of such accelerator; moreover,

a large number of full gap energy electrons are accelerated together with the negative ions. The presence of high power carried by electrons inside the neutralizer can compromise such component and its work. In case of MAMuG the presence of the intermediate grids can be exploited to deposit the electron power deflecting them in vertical direction by the permanent filter magnets embedded inside the source.

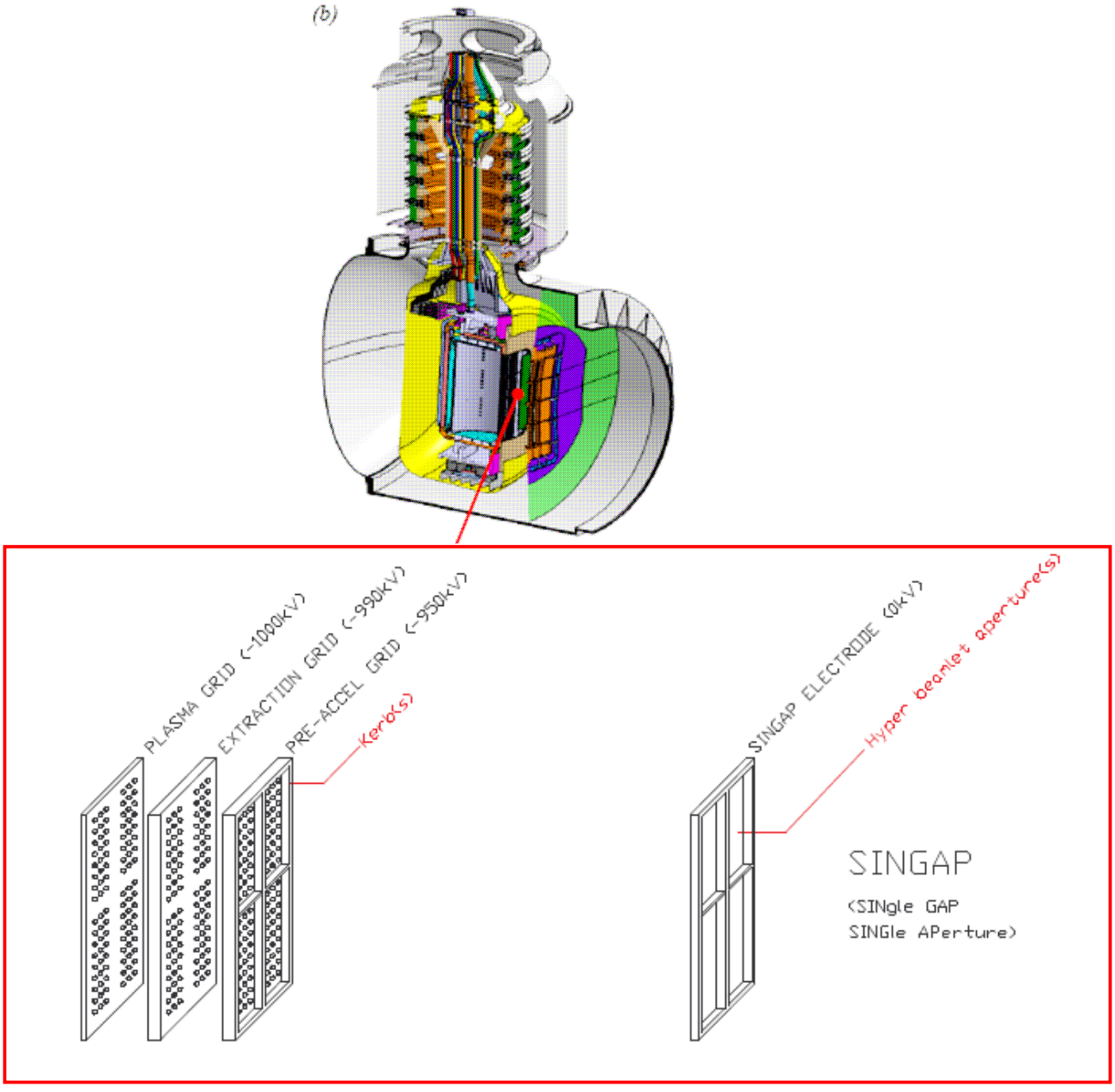

Figure 16 SINGAP grids scheme [29]

1.6 Negative ion neutralization and Residual Ion Dump (RID)

Negative ion neutralization is relatively easy due to the low affinity of the additional electron of only 0.75 eV. The neutralizer should:

• provide high neutralization efficiency;

• operate with the lowest possible gas input, in order to limit the stripping losses of the negative ion beam in the accelerator as well as the re-ionization losses of the neutralized beam;

• prevent injection of additional impurities into the tokamak;

• require the lowest possible additional power;

• have a long service life and a high reliability.

All negative ion-based neutral beam projects are based at present on the use of gas neutralizers. The gas neutralizer is based on collisional detachment:

$$\underline{H}^- + H_0 \rightarrow \underline{H}_0 + H^- \qquad \textbf{(4)}$$

(the fast particles are underlined). Unfortunately, several reactions compete with that. The main competitor is the ionization of fast neutrals:

$$\underline{H}^0 + H_2 \rightarrow \underline{H}^+ + e^- \qquad \textbf{(5)}$$

The optimum neutralization rate η_{MAX} is, in first approximation, a function of $r = \sigma_1/\sigma_2$ the ratio of the cross sections of the dominant reactions above:

$$\eta_{MAX} = f(r) \qquad \textbf{(6)}$$

Since both dominant reactions correspond to the same physical phenomenon (electron detachment), r and η_{MAX} are practically independent of the beam energy for energies above several tens of keV; actually the red line of Figure 17 shows a constant value of efficiency for beam energy greater than 100 kV. A gas neutralizer is a technically simple and passive system with a reasonably high efficiency. It has a major drawback: the required high additional gas load which increases the pumping requirements in large beamlines by a factor of 2 or more. In that sense the optimisation carried out on specific devices without neutralization has to consider this aspect in order to match as much as possible the real scenario.

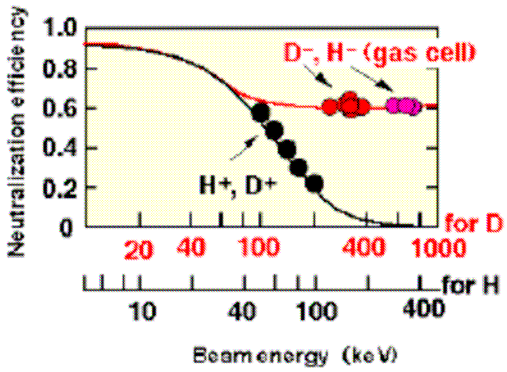

Figure 17 Neutralization efficiency for positive and negative ions.

The fraction of charged beam that exits from the neutralizer is proportional to 1-η. A residual ion dump (RID) is necessary to filter the negative ions. It is positioned downward the neutralizer and uses an electrostatic field to deflect the negative ions toward suitable panels.

The RID structure consists of five vertical dump panels, a support frame, manifolds and headers for the water coolant supply in order to cool the panels where the residual ions deposit their energy.

A good efficiency of the residual ion dump is important in order to avoid depositing the beam power inside the duct that connects the NBI to the fusion reactor vacuum vessel.

Downward of the RID a V shaped calorimeter is positioned, necessary to intercept the beam in order to test the NBI and to measure the characteristics of the beam without reaching the ITER vacuum chamber.

1.7 The Neutral Beam Injector for ITER

In Fig. 19 the layout is shown for the heating and diagnostic NBI: it can be noted how the diagnostic injector doesn't transfer tangential momentum to the ITER plasma, because it should merely provide a H_0 beam at 100kV mainly for spectroscopy measurements.

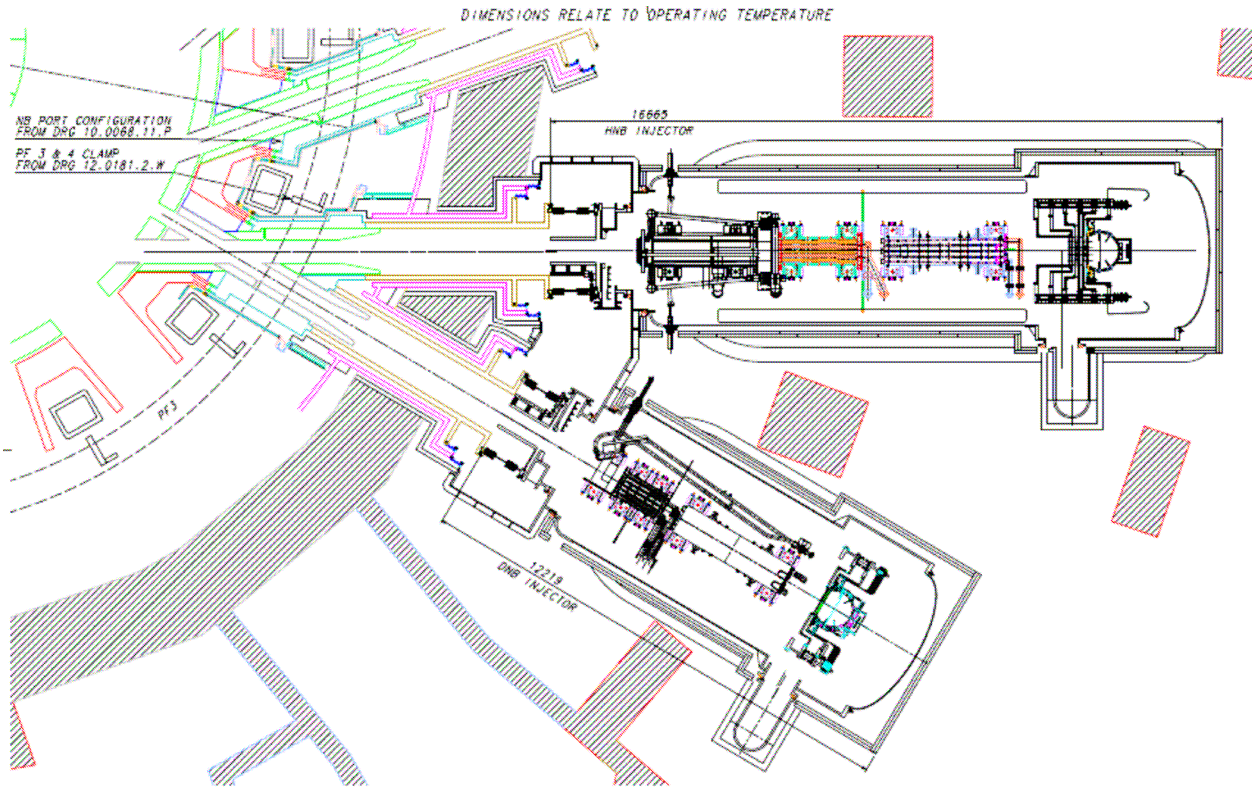

Figure 18 ITER Heat and Diagnostic NBI plan layout [25]

The ITER H&CD NBI (fig. 19) is based on the acceleration of Hydrogen or Deuterium negative ions up to 1 MV.

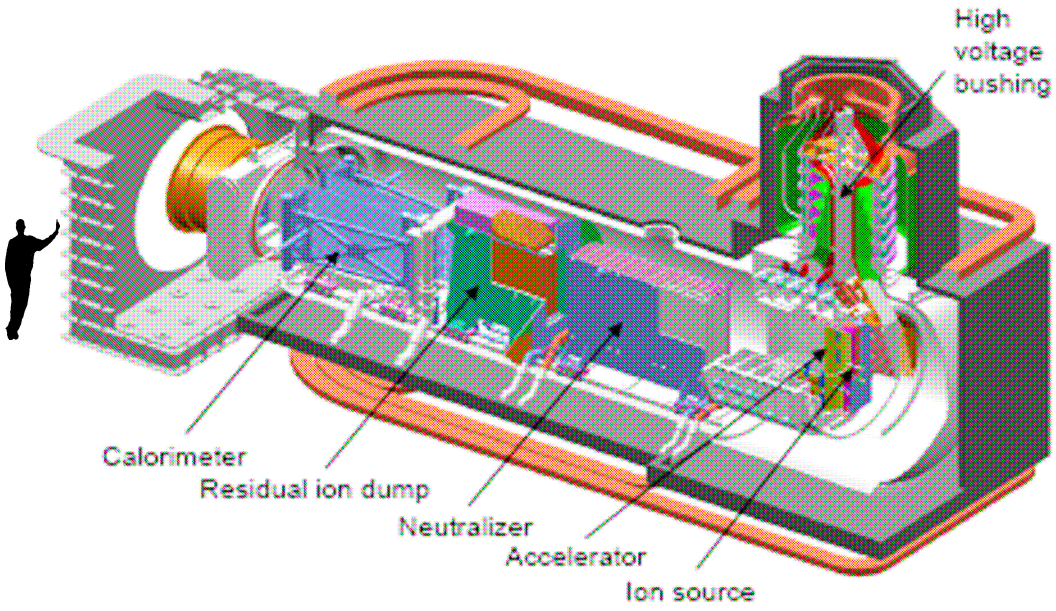

Figure 19 Overview of the NBI for ITER

Each Injector of the ITER Neutral Beam system will deliver a power up to 16.5 MW and guarantee steady operation for one hour in H or in D. To fulfil these requirements, the NBI must provide a current up to 40 A of negative ions accelerated up to 1 MV.

Isotope	H, D
Extraction Area	2000 cm^2
Ion current	40 A
Total Voltage	1 MV
Extraction Voltage	~10 kV
RF Power	720 kW (8 x 90 kW)
Pulse lenght	3600 s

Table 1 Main parameters of ITER NBI [25]

The high particle energy depends on the need to deposit the NB power in deeply inside the ITER vacuum chamber. The pulse length has been chosen in order to be compatible with the duration of the ITER operation

The most important components of the ITER NBI are:

• A high voltage bushing, that acts as a 1 MV feed-through for power supplies, cooling lines and diagnostic cables;

• An ion source, that provides the negative hydrogen or deuterium ions (H- or D-);

• An accelerator, that accelerates the ions up to the potential of 1 MV;

• A neutralizer, that transforms the negative ions into neutrals;

• A Residual Ion Dump (RID) that dumps the remaining negative and positive ions still present in the beam.

A calorimeter that measures the power of the neutral beam; this component is always active in the Test-bed Facility, while it can be open and closed in the ITER NBI, depending on the operation phase.

The functionality of the whole system depends on the performance of each component listed above, nevertheless the components appear linked like a cascade: the functionality of the upstream parts is poorly influenced by the downstream ones; this means that the R&D activities can be carried out on the single parts step, by step starting from the bushing and ending to the calorimeter.

1.7.1 The ITER NBI requirements

The neutral beam injection must be optimised to provide:

- High overall efficiency of beam delivery to the plasma; the ratio between the power of the accelerated neutrals and the electric power that supplies the beam generation and acceleration should be maximized.
- The required beam power profile into the ITER plasma, while limiting the power deposition onto the surfaces of the beam line components within safe design limits, in order to avoid damages and aging effects,

The on-axis and off-axis current drive is to be achieved by tilting the beam axis vertically as shown in fig. 20.

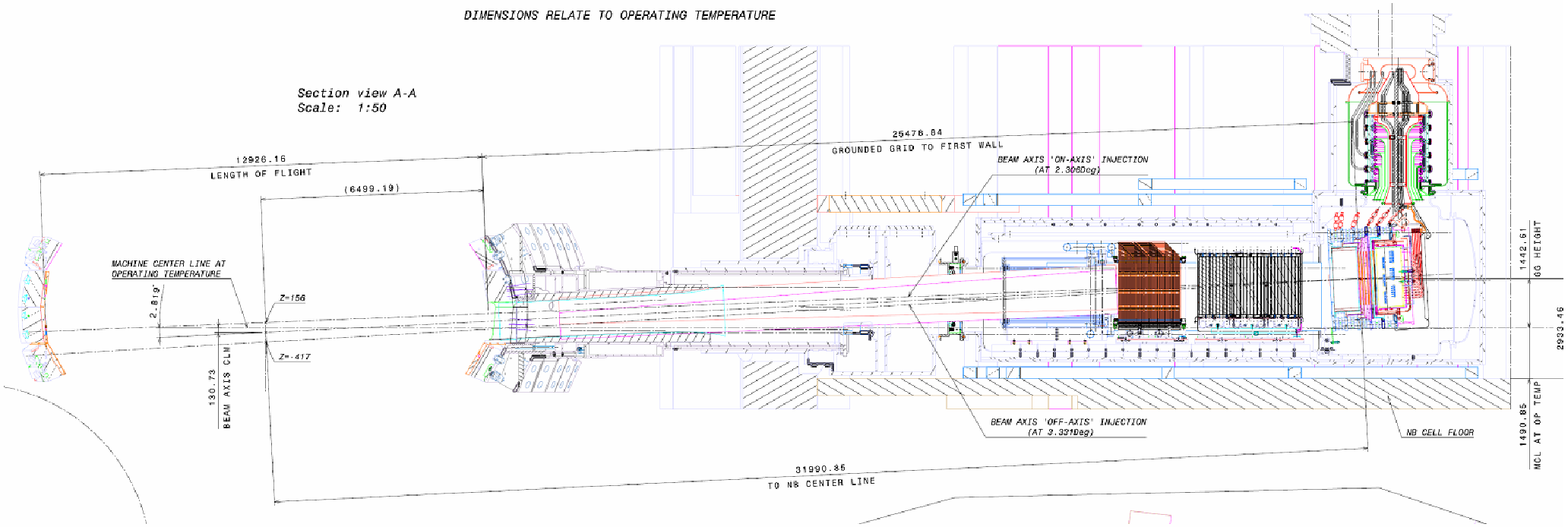

Figure 20 Beam NBI Vertical Cross Section [25]

The required injection can be achieved by tilting the beam axis vertically by the inclination angles listed in table 2

On-axis inclination angle	2.306°
Middle inclination angle	2.818°
Off-axis inclination angle	3.331°

Table 2: ITER's tilting angle requirements

In order to guarantee the required total tilting angle, a mechanical system has been developed, that should slightly rotate the whole beam source. This requirement severely complicates the design of the flexible connections that feed the beam source: for this reason, a valid alternative solution has been developed. It consists of an active steering system, which will be presented in chapter 6.

1.8 The Megavolt Test Facilities at JAEA

The Megavolt Test Facilities (MTF) installed at the Japanese Atomic Energy Agency (JAEA) laboratory of Naka is nowadays a reference point for the technology of the high voltage electrostatic accelerators. High voltage tests and negative ion beam generation are the main features that the device can offer; the experimental results obtained by the MTF have been extremely important to develop the ITER NBI accelerator. The MTF is the result of a long tradition based on positive and negative ion accelerator research: the experience of the NBI group at Naka is considered a reference in the R&D activities related to the ITER NBI.

The MTF is a vacuum insulated accelerator composed by five stages, fed through a high voltage bushing. A Kamaboko arc driven ion source produces a negative ion beam that is intercepted by a suitable instrumented calorimeter. Neutralizer and RID aren't present.

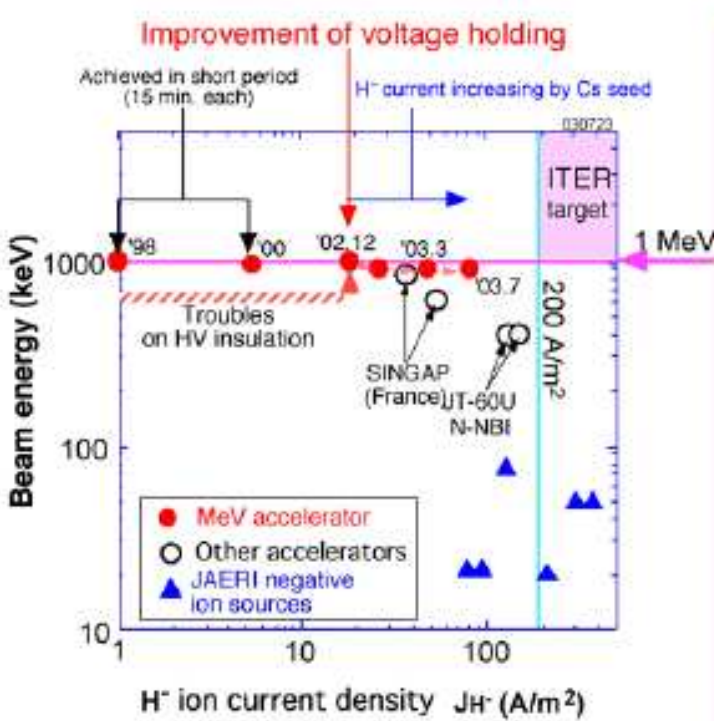

Figure 21 A summary of the negative ion sources performance compared with the ITER NBI requirements [31]

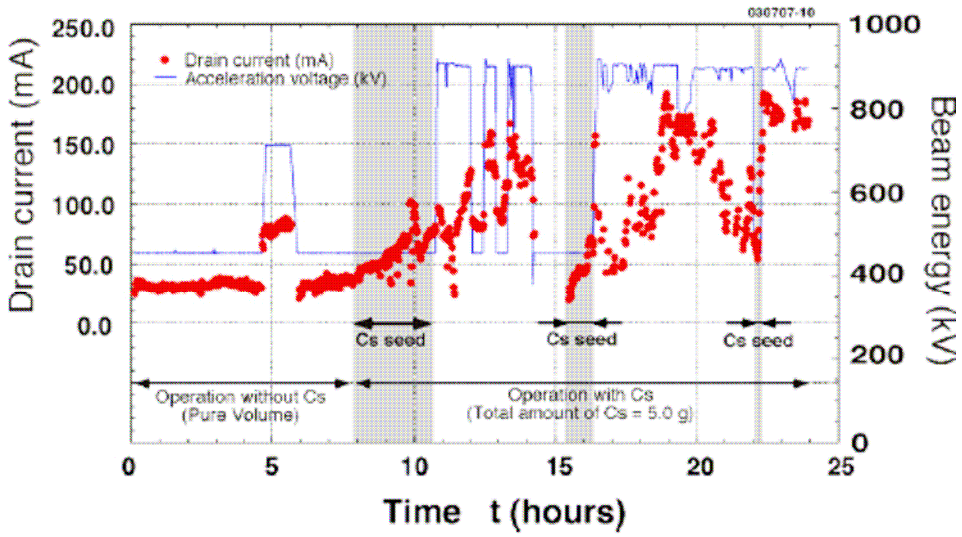

Figure 22 A time record of an acceleration test, current and voltage evolution [34]

Figure 21 and Figure 22 are a summary of the main results obtained in the framework of the research for the ITER NBI; it is possible to notice how the MTF results are the closest to the ITER NBI requirements. The whole device is placed inside a concrete bunker (see Figure 23) in order to limit the x-rays produced by the electrostatic accelerator: the x-rays are present during the conditioning phase and, in particular, during the beam generation.

Figure 23 Removable top Concrete x-ray shield. Photo kindly supplied by JAEA NBI group.

The 1MV acceleration represents the relevant target for such kind of accelerators; the insulating problems are present not only inside the vacuum of the accelerator, but also on the outer side where the pressurized SF6 gas prevents the risk of discharge both for the bushing and power supply (see Figure 25). Figure 24 shows the bushing and the accelerator used in the MTF.

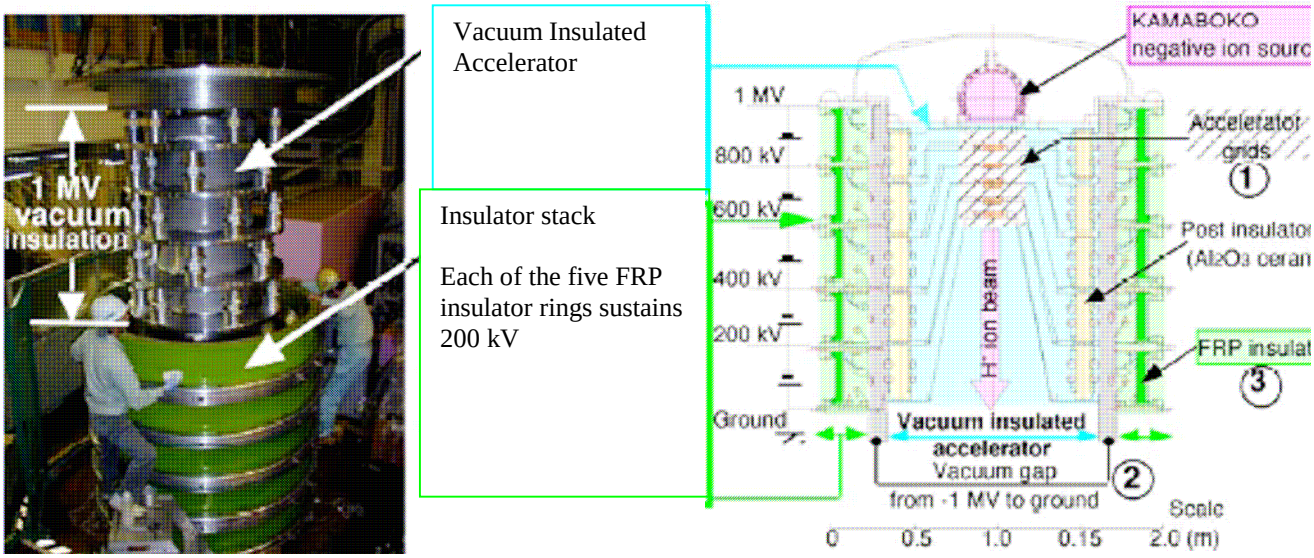

Figure 24 JAEA MTF Vacuum insulated accelerator [31]

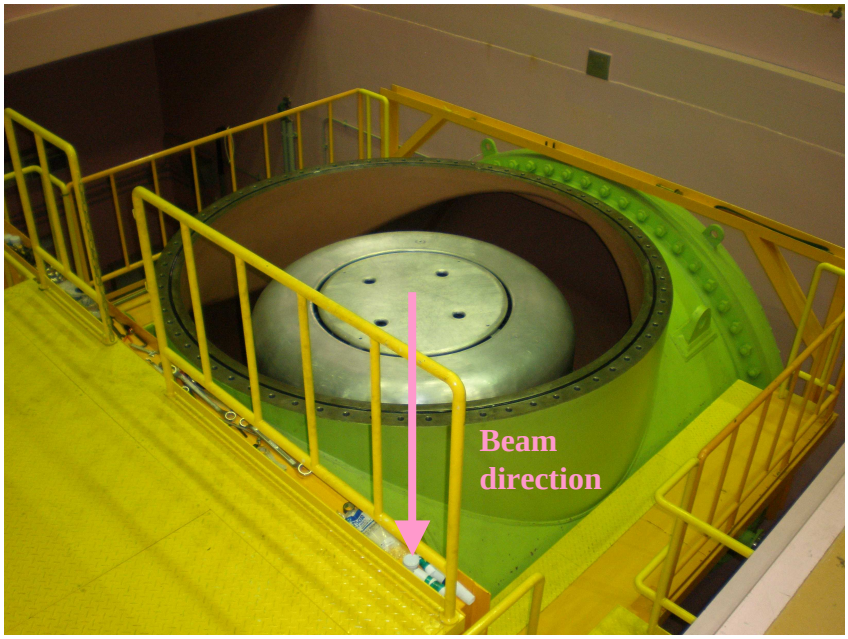

Figure 25 The SF6 tank and the electrostatic screen at the -1MV potential. Photo kindly supplied by JAEA NBI group.

The vacuum boundary that insulates the main structure of accelerator from the SF6 gas is a FRP (fibres reinforced epoxy) insulator column consisting of a stack of 5 FRP insulator rings. The dimensions of each ring are 1.8 m diameter and 0.33 m height, and hence, the overall size of the FRP insulator column is 1.8 m diameter and 1.9 m height [34].

The acceleration grids are insulated by vacuum and their support structures are made of alumina, these insulators are also mechanical components because they suspend the whole accelerator which is placed inside the bushing (see Figure 26).

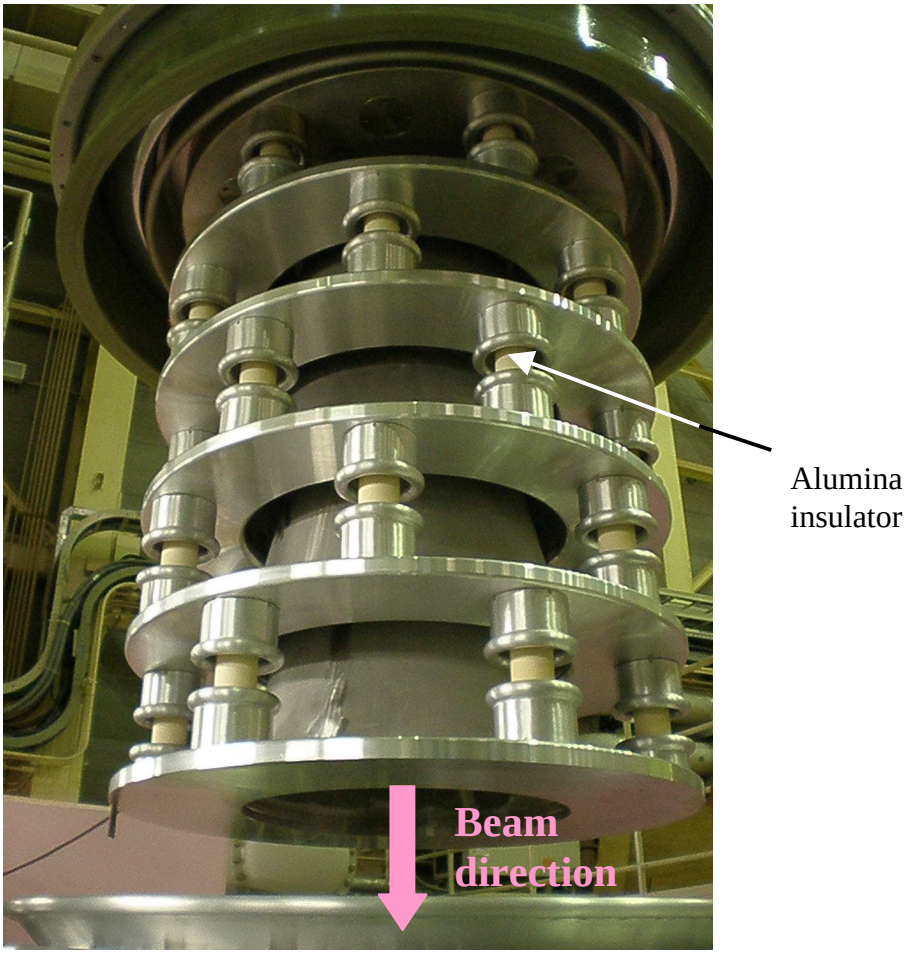

Figure 26 VIBS (Vacuum Insulated Beam Source). Photo kindly supplied by JAEA NBI group.

Only the parts crossing the vacuum gap are metal rods to apply the electric potential to each acceleration grid. The accelerator main structure is insulated and sustained from the FRP insulator column, the FRP rings (green parts in Figure 24

Figure 24) are compressed by the weight of the source and by the effect of the SF_6 external pressure (6 bar) that acts against the vacuum inside the accelerator.

The KAMABOKO negative ion source is mounted on the top flange at –1 MV (see Figure 27).

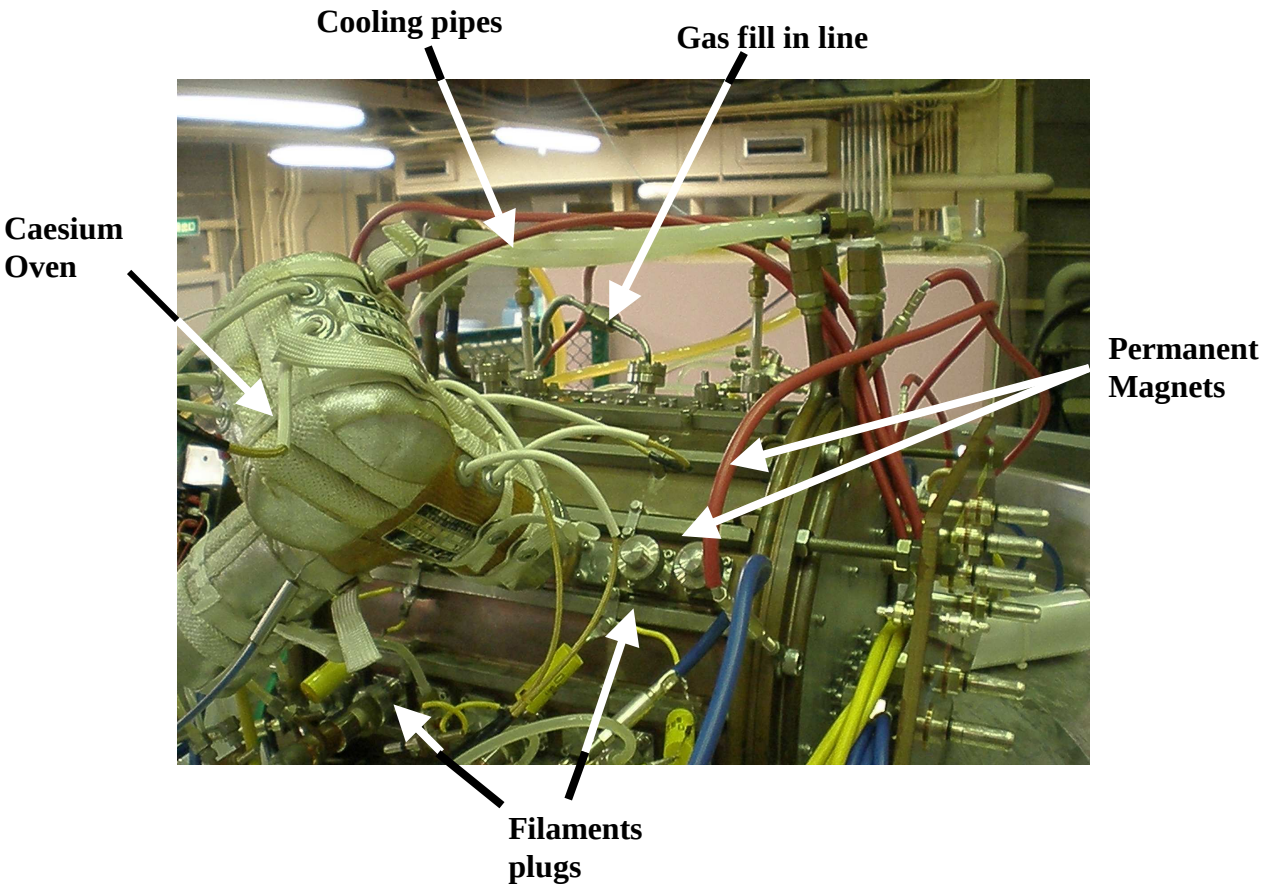

Figure 27 Kamaboko ion source and components. Photo kindly supplied by JAEA NBI group.

It is a filament ion source that has produced a negative ion current density up to 14.6 mA/cm^2. The extracted H- ions are directly injected into the accelerator. The H- ions are progressively accelerated by the potential applied to each acceleration grid, to increase their energy by 200 keV in each acceleration gap between grids.

The accelerator can sustain the voltage of 1 MV for 8,500 s continuously without breakdown [34].

Although the stable production of the -1MV ion beam has been demonstrated several times, the repeatability of the results is strictly related to the cleanliness and the aging of the material employed on the vacuum side, in particular the emission of carbon compounds from the FRP rings is the relevant aspect in the high voltage holding capability for the MTF. As well, good and safe conditioning is necessary to guarantee a stable high voltage level. Pressure, voltage, emission of particles by spectroscopy and X-ray production are the quantities that the operator of MTF controls during conditioning.

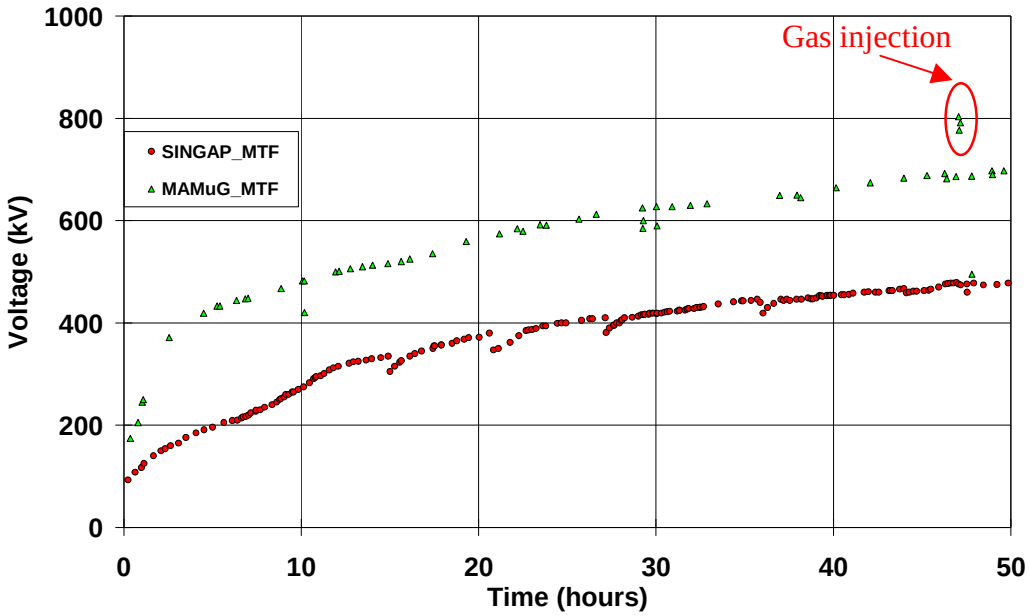

Figure 28 Conditioning plots, Voltage vs. time. [48]

Conditioning is carried out by increasing manually the voltage step by step. In Figure 28 a typical conditioning curve is shown for MAMuG and SINGAP configurations. The MTF has a multistage Crofton-Walton generator connected to a resistive voltage divider; the stable negative ion production is due to the coupling between the characteristics of the high voltage accelerator and the power supply limit. A suitable interlock is placed in the 800 kV stage: the power is cut off if the current collected by this stage exceeds 15-50 mA; the choice of this limit is a compromise between the possibility of damaging the surface of the accelerator during breakdowns and the conditioning time.

The information obtained by the Japanese team has been the basic element behind the final choice of the MAMuG configuration for the ITER NBI. The main reason is strictly related with the voltage holding capability. Figure 28 shows the conditioning diagram for the two configurations applied to MTF: it is possible to appreciate the limited high voltage holding capability of SINGAP. These experimental results are very relevant because they were obtained in the same device, so it appears that the difference in behaviour is only related to the accelerating configuration. This topic will be discussed among the high voltage holding issues in section 2.3.

Chapter 2: General criteria employed in the design of the 1MV accelerator

2.1 The road map to the accelerator design

The heating and current drive performance of the Neutral Beam are strictly related to the characteristics (1MeV, 40 A) and quality of the electrostatically accelerated Negative Ion Beam.
Achieving a high quality of negative ion beam usually means to produce good beam optics, i.e. guarantee suitable beam aiming and emittance.
The need of depositing the beam power in different zones inside the vacuum chamber implies to develop a suitable steering system that allows tilting of the negative ion beam during operation.
Limits on dimensions and the interaction between neutron radiation and insulating materials also contribute to identify the general requirements that influence the accelerator design.
The accelerator design, that implies a close collaboration between physicists and engineers, is still an open issue, because the physics of some processes which happen during operation, haven't been well consolidated yet. Some design criteria appear nowadays to be improved: a typical example in that sense are the voltage holding issues discussed in detail in section 2.3. For these issues the engineers can identify solutions that satisfy the requirements as well as possible, referring to the present knowledge. Sometime, in order to get more confidence and reliability, it is also proposed to explore new solutions and to carry out specific experimental tests.
However design choices and experimental tests to support the design are to be carefully planned considering the targets and the available funds and time.
A pragmatic approach based on specific experimental tests sometimes could not completely satisfy the knowledge process: in that sense, the result of an experimental campaign could be a semi-empirical formula; so a lot of questions that naturally arise during experiments might not have a rapid answer; nevertheless the collected data could be directly applied in the design reducing the time and costs for R&D activities.
The high voltage issues, as well as the mechanical and technological aspects related to the fabrication of the NBI parts, are a good example where the design of a prototype is the result of a process that starts from physics principles and from data obtained by dedicated experimental tests.
The following paragraphs concern the criteria adopted in the design of the high voltage accelerator. The information obtained by the physical studies is the starting point. They can be divided into two branches: the first one concern the design of the grids, the second one identifies the plasma-source

parameters that should be guaranteed to generate the desired beam. In this work the second point has been intentionally omitted, nevertheless a lot of material can be obtained in the literature.

Figure 29 is a flow chart that summarizes the flow of information between each NBI design task. As explained in section 2.2, the beam simulation is very complex because many codes should be used and simplifications and assumptions should be accepted; in that sense, the highlighted box in Figure 29 consist of a group of analyses that should be well coordinated in order to supply the required information.

The first point developed in the framework of physics activities has been the definition of the reference geometry for the accelerator: the beam divergence has to be limited by a suitable choice of the gaps between the grids and hole diameters. In order to simplify the design of the power supply systems, the acceleration potentials are equally subdivided between zero and the maximum level: this means that acceleration gaps must decrease along the beam direction. The thickness of the grids and the hole diameter can be calculated by bi-dimensional codes that solve the Poisson's equation but stripping reactions should be considered for a correct evaluation of the electrostatic field inside the accelerator.

The geometry of plasma and extraction grid (EG) and the gap between them are important parameters; the quality of the beam is strictly influenced by the extractor design: a displacement of 0.1 mm for the EG, due to thermal expansion or incorrect assembly, can influence the beam divergence; on the other hand imprecision or displacement of the other grid seems not to be so important [30].

The second point, developed in the framework of physics activities, has been the design of the electron suppression system. Some permanent magnets are embedded inside EG, to deflect the co-extracted electrons toward such grid; in this way it is possible to filter the electrons from the negative ion beam: the electron heat flux depends on the magnet configuration and position. For this reason, the magnets should be designed and integrated in the EG together with the active cooling lines that control the grid temperature.

The design of the grids together with the voltage drops are the input parameters for the electrostatic and mechanical analyses; the voltages and the plasma source parameters are the main input for the power supply design. The technological aspects related to the fabrication of such grids must be considered the very beginning: it is advisable to carry out the grid design in close collaboration with the manufacturers, because fabrication technologies can constrain some relevant choices in the design. The voltage hold-off capability, the structural and thermo-mechanical verifications are the last design step.

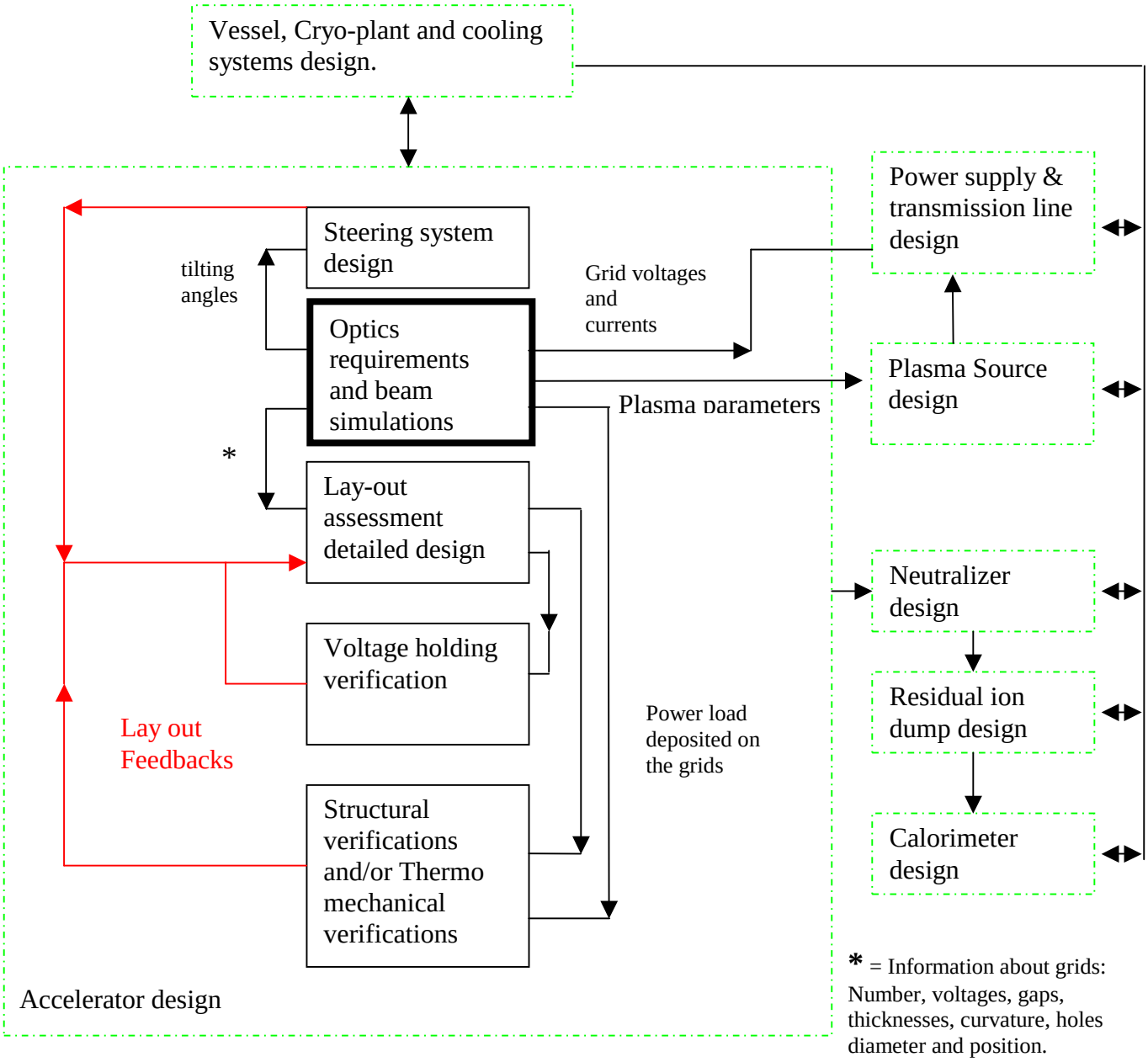

Figure 29 Information Flow chart for the NBI accelerator design.

The diagram of fig. 29 also underlines the relationships that link the activities defining the design of the electrostatic accelerator. It is worth noting, that no feedback link is foreseen toward the “optics requirements”: it means that the aim of the accelerator is to produce a negative ion beam with suitable characteristics, and all the other design choices should be subordinated to the beam requirements.

2.2 Physical models and numerical tools

The correct design of the extraction system plays an important role in the overall performance of the beam injection system because the primary positive or negative ion beam receives its final status at the level of the extraction system: suitable numerical models are thus required to predict the behaviour of the accelerated beam and to supply the information necessary to carry out the detailed design.

2.2.1 An overview on beam physics and numerical models

The formation of the ion beam occurs through electrostatic extraction and acceleration of the ions to the desired energy. The principle of the electrostatic lens introduced in chapter 1 allows understanding the physical reasons that undergo the functionality of the whole accelerator.

The processes that allow the formation of the beam are schematised in Figure 30. They start in the plasma source: the power produced by the RF drivers passes to the plasma inside the expansion chamber and the magnetic filter region, that divides the expansion region from the extraction one, allows minimizing the flux of electrons while improving the negative ion extraction. The main production of H- comes from the reaction on the PG surface where the deposition of a caesium mono-layer sustains the negative ion production, then the negative ions are accelerated downstream the PG.

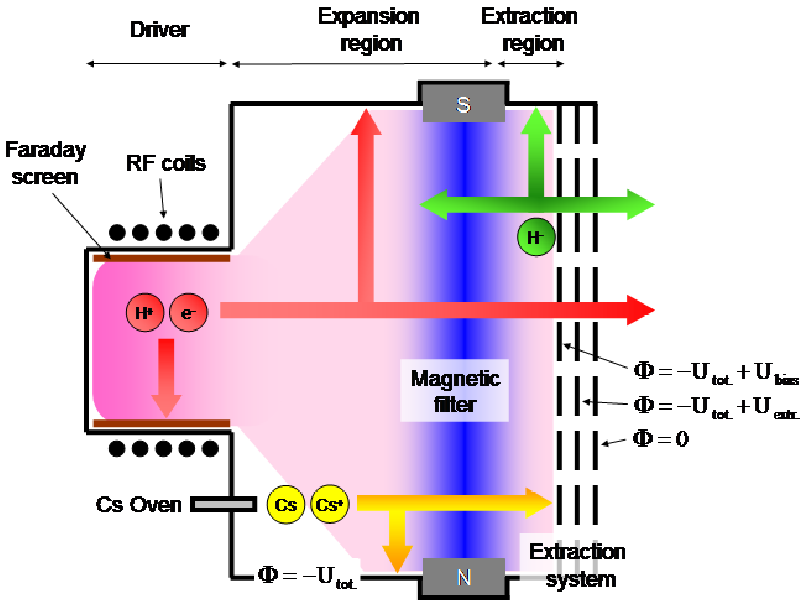

Figure 30 Physical processes inside the source [4]

A self-consistent simulation of the process described above appears quite impossible at the moment, because the scale lengths that characterise the phenomena appear quite different, so more than one code is necessary to simulate the plasma source.

Instead the physics of the ion beam downstream the PG is better understood; in that sense the simulations of the beam appear more straightforward than the simulations of the plasma processes that happen inside the source, where the transport process from the drivers, the presence of a magnetized plasma and the "chemistry" of the negative ion production severely complicate the numerical simulations. This is the reason why the experimental approach, based on tests for the ion source plays nowadays a dominant role in the research for the NBI.

Several approaches allow simulating the charged beam: the beam extraction and acceleration can be simulated by Particle In Cell codes (PIC) bi-dimensional or tri-dimensional Monte Carlo codes, the stripping reactions can be included by following several ways. Nevertheless the main difficulty in beam simulation is the meniscus computation: the meniscus (see Figure 31) is a curved equipotential surface, whose radius is determined by the self-consistent space-charge of ions and from which the ions are extracted [37].

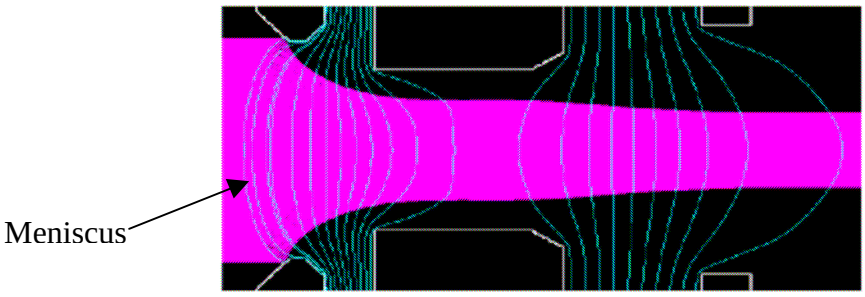

Figure 31 Analysis of a beamlet with the code SLACCAD

In chapter 5, EAMCC (Electrostatic Accelerator Monte Carlo Code) developed by G. Fubiani [56] has been used to compare the MTF experimental results with the numeric one.

It is important to remember that the accelerated beam is composed by several species (e^-, H^- , H_0, H^+, H_2^+) and that a significant fraction of the negative ions can be stripped in the accelerator, losing their second electron by collisions with the neutral gas: the cross section for this reaction is large: $10 \div 15$ cm^2 at E (H^-) < 20 keV, while the gas density in the pre-accelerator is in the $10^{13} \div 10^{14}$ cm^{-3} range.

The beam simulation can start downward the meniscus. The general equations that can be used in beam simulation are listed in (7): the first equation is the law of motion with relativistic formulation

where $\gamma = \left(1 - \frac{v^2}{c^2}\right)^{-0.5}$. The second one is Poisson's equation, the fourth one is Ampere's law, and the last expression of (7) takes into account the reactions that can occur inside the beam.

$$\begin{cases} \dfrac{d}{dt}\left(\gamma \cdot m_k \cdot \overline{v_k}\right) = q_k \cdot \left(\nabla U + \overline{v_k} \wedge \overline{B}\right) \\ \nabla^2 U = \dfrac{\sum q_k \cdot n_k}{\varepsilon_0} \\ \overline{J_k} = q_k \cdot n_k \cdot \overline{v_k} \\ \nabla \wedge \overline{B} = \mu_0 \cdot \sum \overline{J_k} \\ \nabla \cdot \left(n_k \cdot \overline{v_k}\right) = \sum_{i \neq k} n_k \cdot n_i \cdot < \sigma > \end{cases} \qquad \textbf{(7)}$$

The cross section effect, underlined in Figure 32, is sometimes computed by a dedicated simulation: the main contribution is related to the stripping reactions that imply a loss of beam current inside the accelerator. These losses can reach 20÷40% of the H- extracted current and degrade the overall performance of the system; a good way to reduce them is to decrease as far as possible the pressure inside the accelerator. The stripping losses can be evaluated by computing the background gas density distribution; the simulations for the density distribution can be carried out by simple one dimensional calculations (see Figure 32) that take into account the conductance calculations along the beam direction or alternatively it can be calculated by Monte Carlo gas flow codes: in this way it is possible to evaluate the 2 or 3 dimensional density field inside the accelerator.

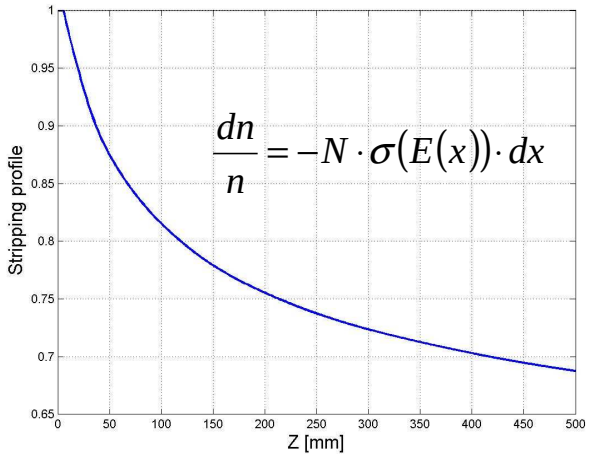

Figure 32 A typical Stripping profile along the beam direction

The effect of the stripping reactions can be considered by multiplying the right side of Poisson's equation by a suitable coefficient in the range 0÷1.

The electrostatic field inside the accelerator can be obtained by solving Poisson's equation (8) and the particles law of motion; in this case the solution will not satisfy Ampere's law. Nevertheless, the magnetic field produced by the current is one order of magnitude lower than the magnetic field produced by the permanent magnets embedded inside the source and PG.

$$\nabla^2 U = \frac{\left(e \cdot n_e + q \cdot n_i\right)}{\varepsilon_0} \tag{8}$$

By adopting a 1D model, it is possible to evaluate the weight of the extracted electrons on the computation of the right side of Poisson's equation (7) .In this model the beam is composed by negative ions and electrons, the ratio between the current of H- and electrons has been assumed equal to one. In case of absence of stripping losses the ratio Je/Ji remains equal to one along the beam direction.

$$\overline{J_e} = e \cdot n_e \cdot \bar{v}_e \qquad\qquad \overline{J_i} = q_i \cdot n_i \cdot \overline{v_i} \tag{9}$$

By these assumptions, the right side of Poisson's equation can be re-written as shown in (10),

$$\nabla^2 U = n_i \cdot q_i \cdot \frac{\left(1+\alpha\right)}{\varepsilon_0} \quad \text{where} \quad \alpha = \frac{n_e \cdot q_e}{n_i \cdot q_i} = \frac{J_e}{J_i} \cdot \frac{v_i}{v_e} \tag{10}$$

Considering a relativistic formulation expressed by the energy equation (11), it is possible to evaluate the weight of the electrons on the right side of Poisson's equation: a little value of α implies a negligible effect of the electrons.

$$m \cdot c^2 \cdot \left(\gamma - 1\right) = q \cdot U \tag{11}$$

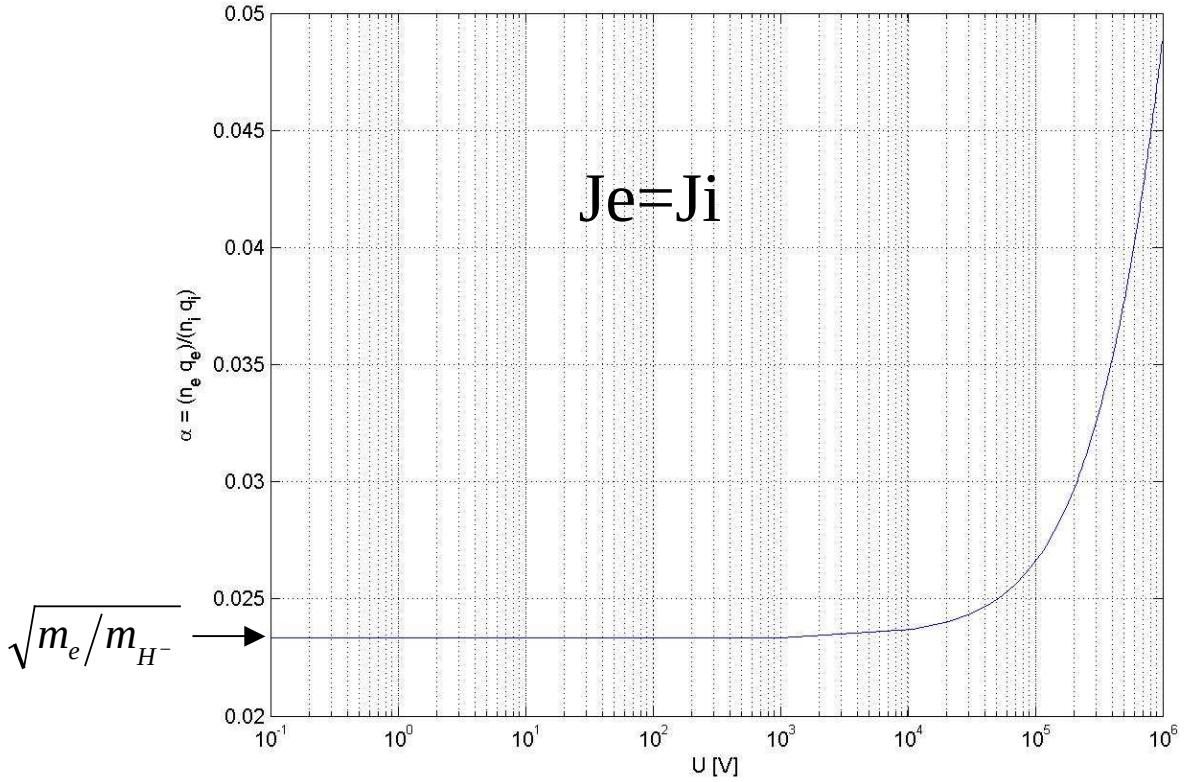

Figure 33 Electron effect on charged particle beam for the computation of right side of Poisson's equation

Figure 33 shows the relationship between α and the accelerating voltage: the evaluation has been done by a mono-dimensional approach considering that velocities are strictly related to the electrostatic potential. Figure 33 shows that the contribution of the electrons is negligible because α is lower than 0.025 in the extraction region.

This explains the reason why the simulation of the lonely H- can be done to evaluate the potential inside the accelerator; a multiplicative factor could be used to correct the computation. In any case the co-extracted electrons are mainly present between plasma and extraction grid, their effect is surely negligible downstream the extraction grid.

The most convenient way to obtain information about the beam behaviour consist of 2D (mainly axial symmetric) analyses, where the beam simulation can be obtained alternating the ray tracing and the Poisson's equation solver. The convergence of the equations is not straightforward, since oscillating solutions can appear.

Although the electron contribution can be negligible in the evaluation of the electrostatic potential, their presence plays a dominant role regarding the power load deposited on the extraction grid and their contribution is surely not negligible for the power supply design.

The simulation of the electrons can be done by 3-D Monte-Carlo codes (EAMCC) , which take into account the secondary emission and the backscattering of electrons. In the relevant energy range, 5÷10 keV, the probability of electron backscattering on a metallic surface can be as high as 30%. If the magnetic configuration of the suppression system is not appropriate, an electron can escape after one or two reflections and can be accelerated downstream. On the other hand, the low energy implies a small Larmor's radius which prevents them from progressing far along the accelerator.
EAMCC performs the integration of the particle motion inside the accelerator; the code allows evaluating the currents on the grids by counting the charges that impact on the grids, as well as the heat flux on the area. The heat flux deposited on the surface can be evaluated by dividing the surface in many pixels: the flux on each pixel is obtained dividing the total power deposited on the pixel by the area of the pixel. This procedure implies that a good evaluation of the heat flux can be done if the number of particles involved in the simulation is quite high; this number has to be compared with the pixel dimension and with the desired spatial resolution. Typical values adopted in the simulation foresee a pixel dimension of 0.25x0.25 mm and a number of primary particles larger than 200k.

2.2.2 A deterministic approach to evaluate the heat flux deposited on the surfaces

An alternative way to estimate the heat power load deposited on the surface has been developed by using ANSYS®. In this approach each single beamlet has been described as a flux tube which undergoes a deflection due to the magnetic field, under the hypothesis of a laminar beam. The power load on the surface intercepting the flux tube can be therefore estimated by the map transform of the flux tube section. For this purpose, the surface has been divided in several portions (24 portions in Figure 34) and for each one the particle density and velocity distribution has been evaluated by a simple expression and the power load derived accordingly.
The starting point for each portion of the flux tube has been assumed on a region where the particle velocity is known. The end point of each trajectory is on a plane that contains the hit surface.

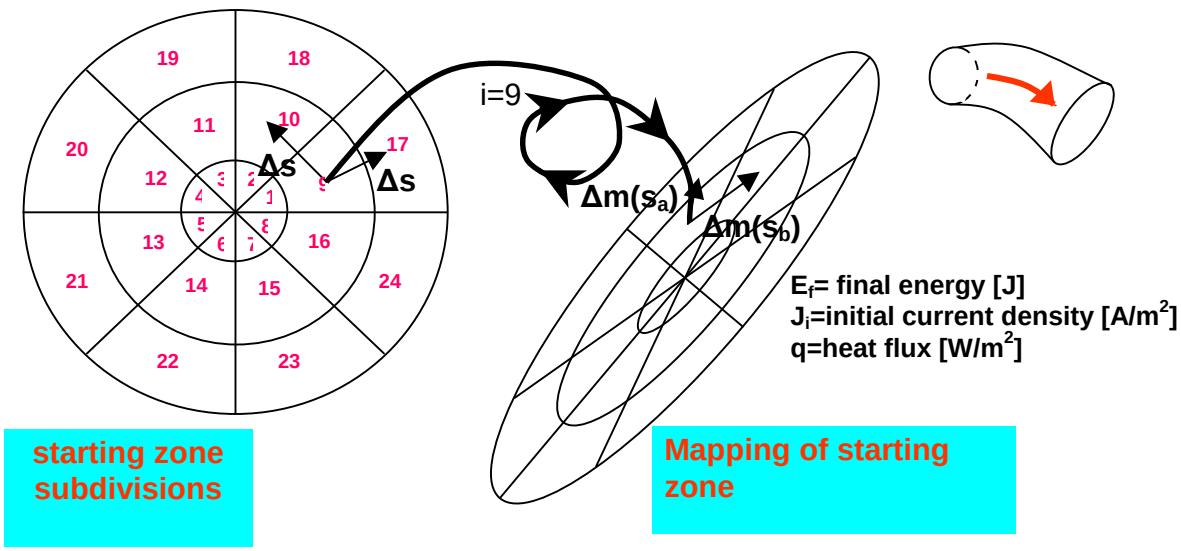

Figure 34 Heat flux computation by Jacoby matrix

By calling S and T the starting surface and the final surface where the power is deposited, each point of S has been mapped to $t = m(s) \in T$ as shown in the scheme in Figure 34. The heat flux per unit surface q [W/m^2] can be evaluated as:

$$q = E_f \cdot \frac{j_f}{e} \qquad (12)$$

E_f is the kinetic energy evaluated at the final surface considering the relativistic effects; it results:

$$E_f = m \cdot c^2 \cdot (\gamma - 1) \qquad (13)$$

The Jacobian factor R of the map $t = m(s)$ can be used to evaluate the ratio between a small area in S and its image on T; it can be easily computed numerically by using eq.(14)

$$R = \frac{\left\| s_b \wedge s_a \right\|}{\left\| \Delta m(s_b) \wedge \Delta m(s_a) \right\|} \qquad (14)$$

where s_a and s_b are points of S adequately near to s_i, and $\Delta m(s_a)$ and $\Delta m(s_b)$ are the respective images.

The current density j_f in (12) can be evaluated from the current density in the "starting zone" j_s and by using charge conservation (15)

$$j_{if} \cdot A_{if} = j_{is} \cdot A_{is} \tag{15}$$

The subscripts "i" indicate the subdivision in areas. Computing the Jacoby's factor for the i-th subdivision, eq. (15) can be rewritten:

$$j_{if} = j_{is} \cdot \frac{A_{is}}{A_{if}} = j_{is} \cdot \frac{\left\| s_b \wedge s_a \right\|}{\left\| \Delta m(s_b) \wedge \Delta m(s_a) \right\|} \tag{16}$$

Combining (12) with (13) and (16), we obtain eq.(17):

$$q_i = m \cdot c^2 (\gamma_i - 1) \cdot \frac{j_{is}}{e} \cdot \frac{\left\| s_b \wedge s_a \right\|_i}{\left\| \Delta m(s_b) \wedge \Delta m(s_a) \right\|_i} \tag{17}$$

It is worth noting that, because of the magnetic field, electron trajectories can focus resulting in hot spots (Figure 35). This effect is seen in the model as $R \to \infty$, (see eq.(14)).

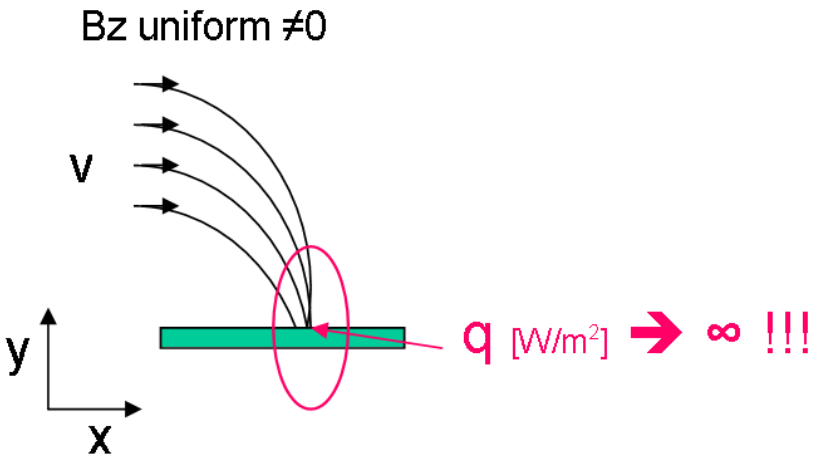

Figure 35 Example of hot spot due to electron focusing

A better calculation of the power load can be performed by taking into account the effect of a non uniform particle energy distribution. A simple model to tackle this aspect is illustrated in Figure 36

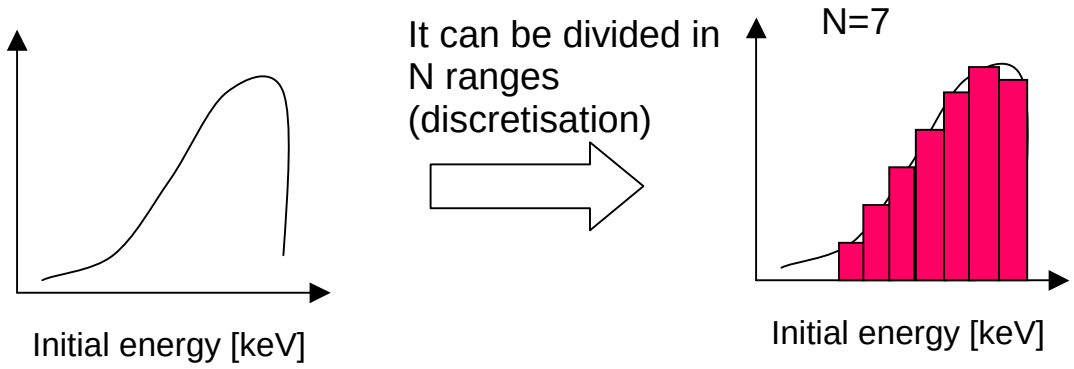

Figure 36 Energy distribution

As a consequence the heat flux has to be recalculated as:

$$q_i = m \cdot c^2 \cdot \sum_{k=1}^{N} (\gamma_{isk} - 1) \cdot \frac{j_{isk}}{e} \cdot \frac{\left\| s_b \wedge s_a \right\|_{ik}}{\left\| \Delta m(s_b) \wedge \Delta m(s_a) \right\|_{ik}} \qquad \textbf{(18)}$$

The contribution of each energy range has to be computed separately and this means to increase the computing time against a better power load estimation.

2.2.3 Relevant quantities in the physics of the accelerated beam

The beam emittance

Emittance is a measure of the parallelism of a beam in a plane Zp normal to the beam direction z. The emittance allows us to compare the quality of beams for specific applications.
Beams with random components of transverse velocity have a spread in angle relative to the axis of propagation. It is possible to define the quantity by plotting the trajectory information in a suitable phase space called trace-space, where the horizontal axis identifies the particle position and the vertical one identifies the ratio between the transverse velocity and Vz; the emittance is proportional to the area filled by the points.
The definition of emittance comes from the necessity of identifying the disorder level inside a beam; actually a beam with good parallelism is easier to transport and to focus than one with large random transverse velocity components.
An ideal lens can focus a laminar beam to a point of zero dimensions. Figure 37 illustrates focusing by a lens of focal length *f* in the configuration space; the parallel incident beam has a half width x_0.

After deflection, the particles converge to a point at a distance *f* from the lens. Figure 37b is a phase space view of the same process. In this case the emittance is 0.

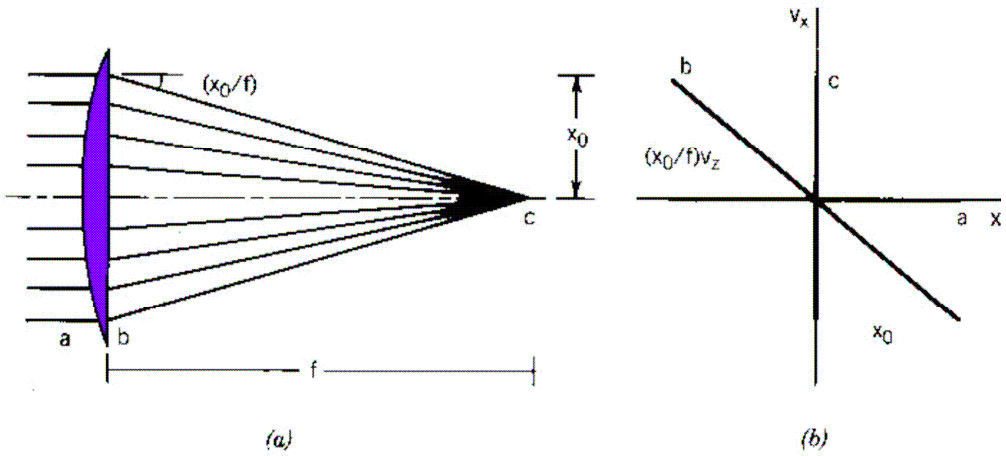

Figure 37 Focusing a laminar beam, relationship between trajectories and emittance diagram. [20]

Particles in a non-laminar beam have a random distribution of transverse velocities at a certain location this means that at the position x they have different values of v_x and a spread in direction. Because of the disorder of a non-laminar beam, it is impossible to aim all particles from a location in the beam toward a common point. Lenses can only influence the average motion of particles.
Figure 38-a shows the trajectories of a laminar focusing beam. Figure 38-b is a configuration space view of the focusing process for non-laminar beams. The beam has a uniform spread of transverse velocity, $\pm\delta v_x$, at all positions in the cross-section. The beam entering the lens is almost parallel; the average transverse velocities at all positions are equal to zero. Individual particles have inclination angles in the range $\pm\delta v_x/v_z$. Passing through the lens, particles acquire a convergence angle that sums with the angular spread. The best focus occurs at approximately a distance *f* from the lens. Figure 38b shows that the trajectories at the focus spread over a non-zero spatial width. The half width for the focal spot is $\delta \cong \Delta v_x \cdot f/v_z$ so the width of the focal spot is proportional to the transverse velocity spread of the incident beam [20].

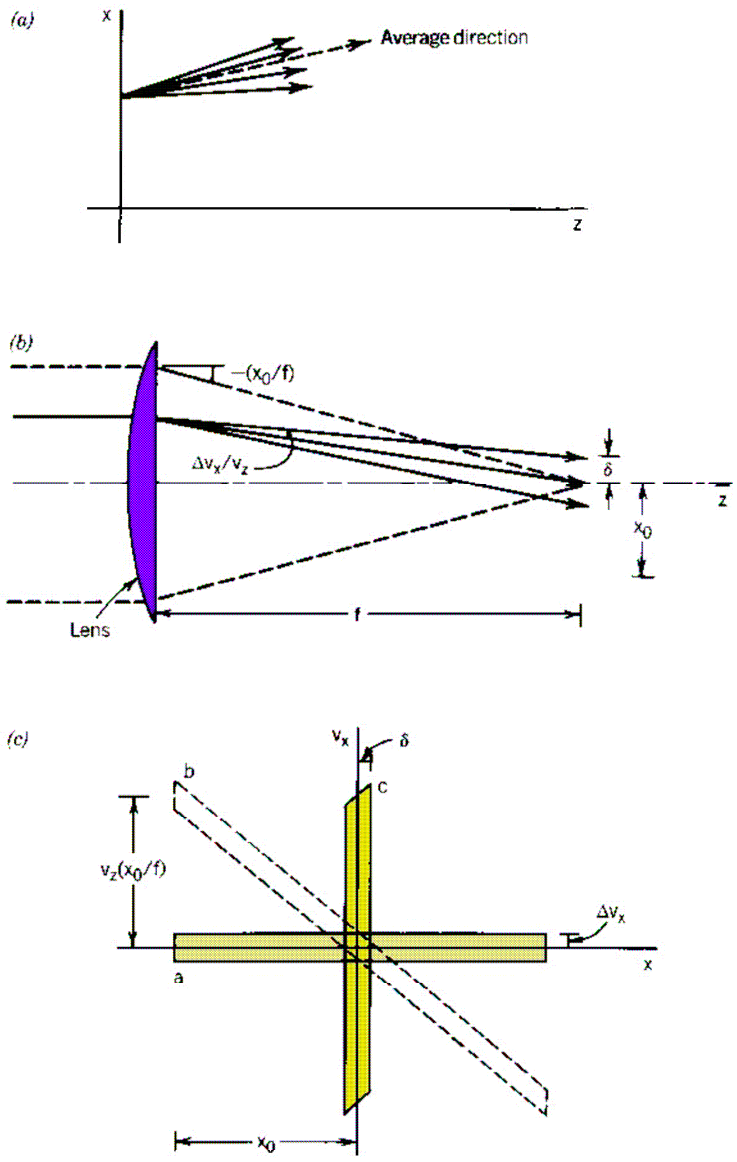

Figure 38 Example of focusing of a non laminar beam. [20]

In this example the beam emittance is represented by the yellow area of Figure 38c: a smaller phase area occupied by the beam implies a better quality of the beam; where the term quality means focusability or parallelism. The minimum phase-space volume of a distribution is determined by the characteristics of the beam injector. Processes that increase the phase-space volume are undesirable.

The adimensional parameters necessary to identify the physics of the accelerated beams

The Buckingham theorem can be used to identify the relevant adimensional parameters that describe beam physics.

The simple example shown in Figure 39 is sufficient to define the adimensional parameter that controls the motion of a particle in an electrostatic field without taking into account the spatial

charge effect: a sphere of radius R, placed at a distance L from a grounded plane, is kept to a fixed potential U; on the left side of the sphere there is an emitter of charged particles q, the particles are emitted with an initial velocity V_0 , they hit the horizontal plane at the coordinate X. The electrostatic field that determines particle motion can be calculated by solving Laplace's equation $\nabla^2 U = 0$.

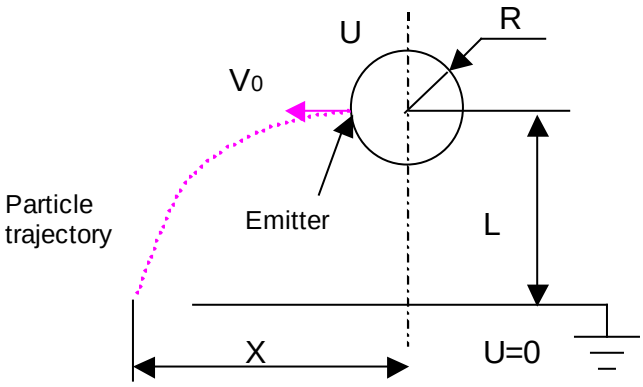

Figure 39 A particle trajectory for a generic electrostatic field

The coordinate X can be simply calculated by integrating the motion law for a charge particle in an electrostatic field with no space charge effect.

An alternative approach uses adimensional parameters; in this case the dimensional analysis can be useful to supply information about the physics that controls the phenomena.

$$X = f\left(M, v_0, q, U, R, L\right) \qquad \phi\left(X, M, v_0, q, U, R, L\right) = 0 \tag{19}$$

The aim of the problem can be expressed by eq. (19) respectively in explicit and implicit form.

The adimensional analysis is a technique to identify a suitable number of groups of adimensional quantities that could describe the physics phenomena starting from the implicit formulation as shown in (19).

In this case, each quantity is composed by the following absolute units:

- X $[kg^0\ m^1\ s^0\ A^0]$
- M $[kg^1\ m^0\ s^0\ A^0]$
- V_0 $[kg^0\ m^1\ s^{-1}\ A^0]$
- q $[kg^0\ m^1\ s^1\ A^1]$
- U $[kg^1\ m^2\ s^{-3}\ A^{-1}]$
- R $[kg^0\ m^1\ s^0\ A^0]$

- L [$kg^0\ m^1\ s^0\ A^0$]

Identifying an adimensional parameter means to find a suitable set of α_1, α_2, …., α_n exponents in order to obtain a group $\Pi = X^{\alpha_1} \cdot M^{\alpha_2} \cdot v_0^{\alpha_3} \cdot q^{\alpha_4} \cdot U^{\alpha_5} \cdot R^{\alpha_6} \cdot L^{\alpha_7}$ without any units. The search of α_i means to solve the linear and homogeneous system (20).

$$\begin{matrix} kg: \\ m: \\ s: \\ A: \end{matrix} \begin{bmatrix} 0 & 1 & 0 & 0 & 1 & 0 & 0 \\ 1 & 0 & 1 & 0 & 2 & 1 & 1 \\ 0 & 0 & -1 & 1 & -3 & 0 & 0 \\ 0 & 0 & 0 & 1 & -1 & 0 & 0 \end{bmatrix} \cdot \begin{Bmatrix} \alpha_1 \\ \alpha_2 \\ \alpha_3 \\ \alpha_4 \\ \alpha_5 \\ \alpha_6 \\ \alpha_7 \end{Bmatrix} = \begin{Bmatrix} 0 \\ 0 \\ 0 \\ 0 \end{Bmatrix} \quad \textbf{(20)}$$

The rank of the matrix (20) used in the adimensional analysis is 4, instead the number of variables of ϕ is 7, so the Buckingham's theorem [32] (and in particular the Rouché-Capelli's theorem) assures that 7-4=3 adimensional parameters exist that solve (20) and that describe the phenomena.
In this case we have ∞^3 solutions that can satisfy (20), nevertheless a reasonable choice is to assume $\Pi_1 = \frac{X}{L}$ and $\Pi_2 = \frac{R}{L}$, and the last group can be obtained by assuming that neither R nor L appear in the latter adimensional parameter. This means to add other two rows to (20), so obtaining (21)

$$\begin{bmatrix} 0 & 1 & 0 & 0 & 1 & 0 & 0 \\ 1 & 0 & 1 & 0 & 2 & 1 & 1 \\ 0 & 0 & -1 & 1 & -3 & 0 & 0 \\ 0 & 0 & 0 & 1 & -1 & 0 & 0 \\ 0 & 0 & 0 & 0 & 0 & 1 & 0 \\ 0 & 0 & 0 & 0 & 0 & 0 & 1 \end{bmatrix} \cdot \begin{Bmatrix} \alpha_1 \\ \alpha_2 \\ \alpha_3 \\ \alpha_4 \\ \alpha_5 \\ \alpha_6 \\ \alpha_7 \end{Bmatrix} = \begin{Bmatrix} 0 \\ 0 \\ 0 \\ 0 \\ 0 \\ 0 \end{Bmatrix} \quad \textbf{(21)}$$

The linear system (21) has ∞^1 solutions; this means to identify the last set of rational exponents α_i. The last adimensional parameter for the proposed problem is $\Pi_3 = \frac{M \cdot v_0^{\,2}}{q \cdot U}$ .It is possible to rewrite the implicit formulation for ϕ as proposed in (22)

$$\phi(\Pi_1, \Pi_2, \Pi_3) = 0 \tag{22}$$

A possible choice of Πi is $\Pi_1 = \frac{X}{L}$, $\Pi_2 = \frac{M \cdot v_0^{\,2}}{q \cdot U}$, $\Pi_3 = \frac{R}{L}$. In other words: for a fixed "shape factor" R/L the whole physics described by eq. (22) can be concentrated in the form shown in eq. (23)

$$\frac{X}{L} = f\left(\frac{M \cdot v_0^{\,2}}{q \cdot U}\right) \tag{23}$$

As said before the described problem doesn't take into account the space charge effect. When the contribution by the space charge effect is not negligible, the same analysis can be repeated adding J/ε_0 that is the ratio between the extracted current and ε_0, and d, which is the diameter of the emitting hole. So for a fixed shape factors that include the ratio between the diameter d of the emitting area and L, eq. (19) can be rewritten as shown in eq. (24)

$$X = f\left(M, v_0, q, U, R, L, d, J/\varepsilon_0\right) \tag{24}$$

In this case the number of independent adimensional parameters is 5; following the same dimensional analysis, it is possible to obtain eq. (25)

$$\frac{X}{L} = f\left(\frac{M \cdot v_0^{\,2}}{q \cdot U}, \frac{\varepsilon_0 \cdot U^{3/2} \cdot q^{1/2}}{J \cdot L^2 \cdot M^{1/2}}, \frac{R}{L}, \frac{d}{L}\right) \tag{25}$$

The results obtained in eq. (25) are general; the geometry can be always described by a finite number of adimensional ratios like $\frac{R}{L}$, $\frac{d}{L}$ etc. Instead, in the physics of the accelerated beam, the quantity $\frac{\varepsilon_0 \cdot U^{3/2} \cdot q^{1/2}}{J \cdot L^2 \cdot M^{1/2}}$ called "Perveance" is very important, because it evidences that it is possible

to obtain similar beams if the ratio $\frac{U^{3/2}}{J \cdot L^2}$ is kept; similar beams means beams with the same shape and convergence.

In general, any accelerator geometry can be identified by a conventional length L and by the "shape", where the shape is the group of adimensional ratios between spatial dimensions.

So for a certain shape the equation can be re-written as follows:

$$\frac{d}{D} = f\left(\frac{M \cdot v_0^{\,2}}{q \cdot U}, \frac{\varepsilon_0 \cdot U^{3/2} \cdot q^{1/2}}{J \cdot D^2 \cdot M^{1/2}}\right) \qquad \textbf{(26)}$$

where d is the beam diameter outside the accelerator, and D is the diameter of the emitter in the plasma grid.

Equation (26) suggests that the accelerator behaviour can be expressed by a surface or by several curves like those sketched in Figure 40.

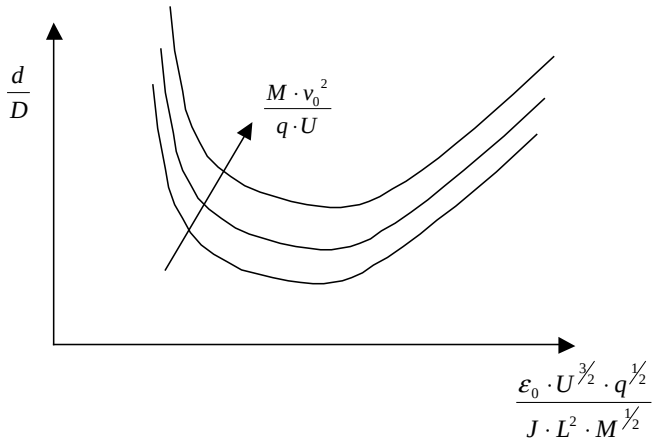

Figure 40 Map that characterizes the operational condition as a function of accelerator shape.

For a given extraction geometry there is an optimum match between the ion flux density delivered by the plasma generator and the electrostatic potential U. Because the matching condition for optimum beam divergence has to be met in every single aperture, the plasma generator should produce an ion flux density which is reasonably uniform in space and time.

Non-uniformities larger than 10% usually lead to a degradation of beam divergence.

The concept of perveance can be useful to explain the reasons why the characteristic dimensions of a negative ion source are larger than those of a positive ion source. Let us consider two accelerators with the same shape and same level of voltage, the first has a positive ion source, instead the second has a negative ion source. We know that the extracted current density in the positive ion source is

about 10 times higher than in the negative ion source, $J^+ \cong 10 \cdot J^-$; this means that, if the accelerators should work under nominal conditions with minimum beam divergence, the two values of perveance should be quite similar $\frac{\varepsilon_0 \cdot U^{3/2} \cdot q^{1/2}}{J^+ \cdot L_+^{\,2} \cdot M^2} \cong \frac{\varepsilon_0 \cdot U^{3/2} \cdot |q|^{1/2}}{J^- \cdot L_-^{\,2} \cdot M^2}$: this means that the reference dimensions L_+ and L_- have to satisfy $L^- \cong \sqrt{10} \cdot L^+$, quite in accordance with Figure 6.

2.3 Insulation criteria employed in the accelerator design

As mentioned in 2.1, the electrostatic high voltage accelerator is necessary to achieve the energy of 1MV for the neutral beam injected into the ITER plasma. Good performance of the high voltage accelerator depends on several conditions to be met in order to guarantee a reliable voltage holding, necessary for a stable beam generation.

The following sections describe the insulation design criteria for the spacers and the electrodes;

In particular, the aspect regarding the electrode design are analysed in depth because the processes that control insulation in vacuum across long gaps are still unclear.

It must be also highlighted that the accelerator design is driven by beam optic optimization and by thermo-mechanical requirements (e.g. presence of cooling pipes, electron dump shields, presence of cryo-pumps, etc.) rather than voltage holding aspects. The consequence is complex electrode geometry, as consequence the electrostatic design of the accelerator has to be addressed first to identify the most critical regions in terms of voltage breakdown risk and second to proceed with the local optimization of electrode geometry and material.

2.3.1 Vacuum insulation

The design criteria to identify the voltage holding capability of vacuum insulated systems are not so straightforward, although the vacuum is, in principle, the best insulating medium. Several physical phenomena can occur in a vacuum insulated system. The first quantity to be specified to verify the voltage holding capability of a device working in vacuum is the product between the residual gas pressure p and electrodes gap d.

The most known and consolidated theory used to study the low pressure gas discharge is the application of the Townsend criteria [33] which leads to the Paschen's curve. Figure 41 shows the experimental points obtained in hydrogen in plane parallel geometry with a gap of 270 mm; and in magenta the operating ranges for the ITER NBI accelerator are shown. The high negative slope of the left Paschen's curve side indicates that the pressure controlling has to be carefully controlled in order to keep everywhere the pd product below 0.06 Pa; on the contrary, a rapid degradation of the voltage holding capability happens due to the Townsend's discharge inside the residual accelerator background gas, this issues should be taken into account also in material choice: anomalous surfaces outgassing could lead to a breakdown.

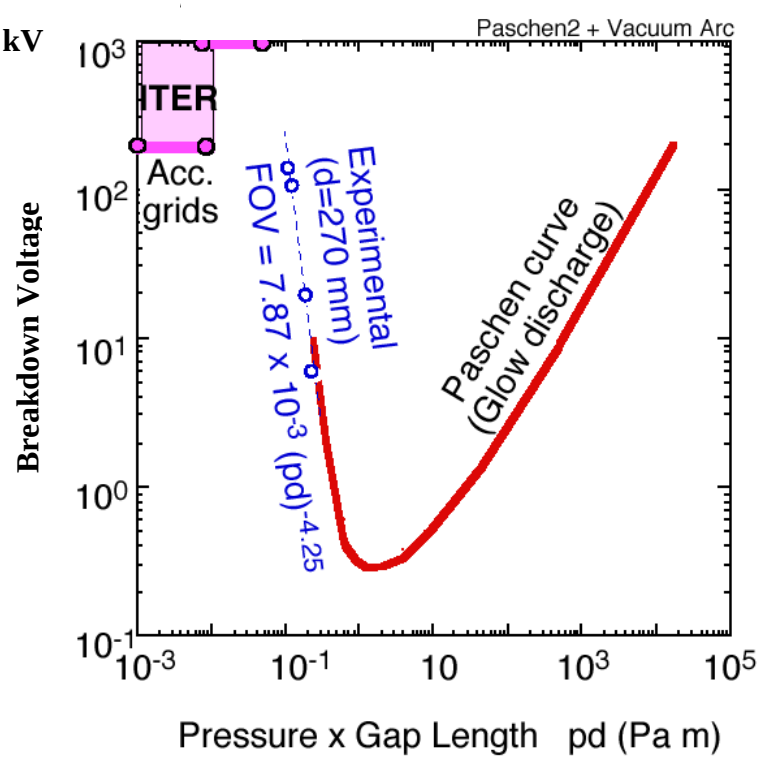

Figure 41 Paschen's curve for Hydrogen. Data obtained with a gap of 270 mm. The left side has been extrapolated to the lower pressure [25]

The gas discharge could be then considered as a fault condition, for the ITER NBI accelerator; for this reason the study of phenomena that control the NBI high voltage capability will be addressed in the following to understand the mechanism of insulation in high vacuum ($pd < 10^{-2}$).

The electric breakdown phenomena in high vacuum depend on the gap length between the electrodes. In the literature, the definition of long gap or short gap devices is not precise because the physics processes that control the discharge over long distance haven't been consolidated yet; nevertheless the "long gap" phenomena are suppose to occur when the distance between electrodes exceeds 5-8 mm [35].

The theory explaining the breakdown for short gaps is much better developed: in this case the basic initiation process is the emission of electrons from the cathode surface. The theory of field emission was proposed firstly in 1928 by R.H. Fowler and L. Nordheim [36]; it allows calculating the emission of electrons necessary to obtain the discharge across short gaps. Eq. (27) is a simplified version that allows evaluating the current density J [A/cm^2] extracted by the electric field E [V/cm], from a cathode, whose material has the work function ϕ [V]:

$$J \cong 8.0x10^{-5} \cdot \frac{E^2}{\phi} \cdot \exp\left(-6.42x10^{7} \cdot \frac{\phi^{3/2}}{E}\right) \qquad \textbf{(27)}$$

Further improvements have been necessary in order to take into account the thermo-ionic effect [42]. Formula (27) was used to validate the measured current in short gaps high voltage devices [43]. It is worth noticing that the electric field E in eq. (27) is the actual electric field on the cathode surface, determined by the surface irregularities. β takes into account this aspect $E = \beta \cdot E_0$ being E_0 the electric field of the ideally smooth electrode surface. The breakdown initiation process is due, for the short gap case, to a thermal instability occurring mainly at the cathode when the local current density J exceeds a limit. The thermal instabilities cause a disruption on the electrodes surfaces, and the vaporized material is thrown in the gap forming the discharge channel. In some case the thermal instability occurs at the anode surface. [43] (See Figure 42).

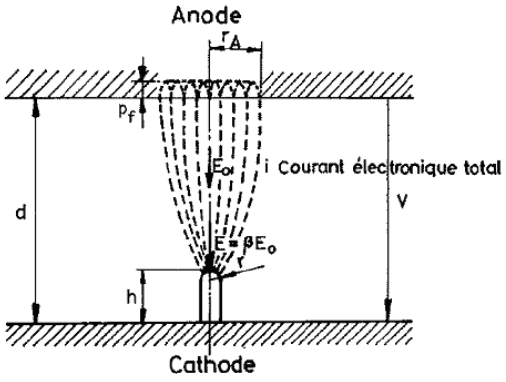

Figure 42 Geometric model for the chathodic electron emission and anode bombardament . [43]

When the electrons heat flux at the anode W_A reaches the limit W_{Amax} (which deepens on the anode material and its heat dissipation characteristic) the eq. (28) can be used to identify the maximum electric field.

$$W_A = \frac{i \cdot V}{\pi \cdot r_A^2} \approx \frac{h \cdot j \cdot E}{4 \cdot \beta^3} = \frac{h \cdot j(\beta, E_0) \cdot E_0}{4 \cdot \beta^2} \qquad \textbf{(28)}$$

The different behaviour (anode or cathode thermal instability) for the breakdown in the short gaps case depends on eq. (27) and (28), so the minimum electric field between the two formulas give the

electric field calculated. If we have two identical high voltage short gap devices that differ only for the cathode surface roughness (this means different value of β) it could happen that the breakdown initiation process appears at the cathode in case of large β and at the anode when β is small. for the same electrode condition (same β) in [43] it is demonstrated the existence of a critical distance above which the breakdown occurs due to the anode effect.

The short gaps case has been explained with particular detail and several improvements has been developed and implemented since 1928 [39, 41, and 42]; the common conclusion of these researches can be summarised as follow:

The initiation of breakdown is related to the electron current density extracted from the cathode: the Fowler-Nordheim's formula, eq. (27) , allows relating the current density with the electric field on the cathode surface; this means that the breakdown criterion is based on a limit on the electric field at cathode. The electrodes materials, the surface finishing of cathode, are important parameters defining such limit.

In the NBI accelerator, the short gaps situations appear in few positions, but in most cases the voltage applied is much lower than the breakdown level.

On the contrary, electrodes separated by large gaps (d > 10 mm), are majority involved for the NBI electrostatic configuration but a satisfactory theory that explains the physics controlling the breakdown is absent, this fact results the major issue for the NBI operation.

In fact, there are some experimental evidences, obtained mainly by plane parallel electrodes and following listed, that demonstrate why the theory based on eq. (27) can't be extended to large gaps cases:

1) The electric field necessary to obtain the breakdown is not constant with d (as foreseen in the short gap theory) but it follows eq. (29).

$$E_s \approx d^{\alpha-1} \quad \text{with } 0.3 < \alpha < 0.8 \qquad \textbf{(29)}$$

2) The pre-breakdown current decreases dramatically by increasing the gap (e.g. $I \approx 10^{-05}$ A with d=5 mm, $I \approx 10^{-09}$ A with d=6 cm) [45].
3) The pressure does not affect the results predicted by the short gap theory; instead, the experiments show a remarkable effect of the pressure in the long gap cases, the pressure sensitivity increasing with the gap length [45]. This practice it is commonly utilized to increase the voltage holding capability. As practical example, Figure 43 shows the pressure effect for the JAEA MTF in MAMuG configuration.

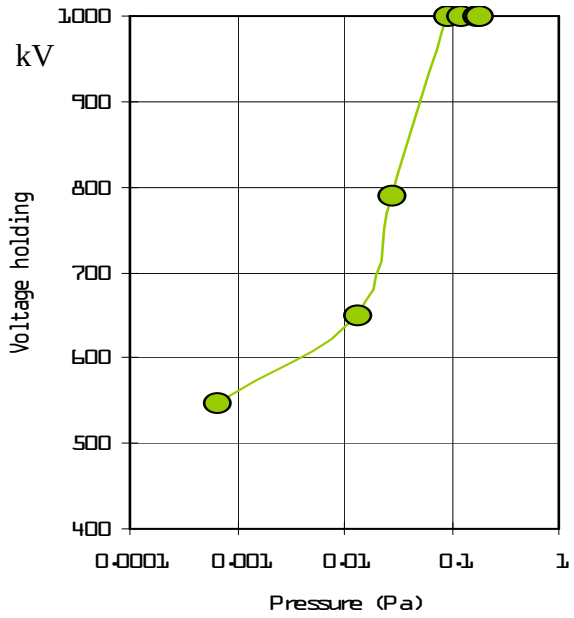

Figure 43 Pressure effect in a long gap device. [48]

Since the fifties, experimental data have been accumulated about the breakdown in vacuum with for large gaps L. Cranberg, observing that the breakdown voltage was nearly proportional to the square root of the gap length $V \propto d^{1/2}$, proposed that the breakdown would occur as a consequence of the detachment by electrostatic force of a clump of material loosely adhering to one electrode, but in electrical contact with it (see Figure 44). He assumed that the breakdown occurs when the energy W per unit area deposited by the clump exceeds a value C'. The quantity W is the voltage V multiplied by the charge of the clump. The latter is proportional to the field E at the electrode of origin, so that the breakdown criterion becomes simply:

$$V \cdot E \geq C \tag{30}$$

In the case of plane parallel electrodes where $E = V/d$ the criterion becomes: $V^2 \geq C \cdot d$, and $V \geq \sqrt{C \cdot d}$.

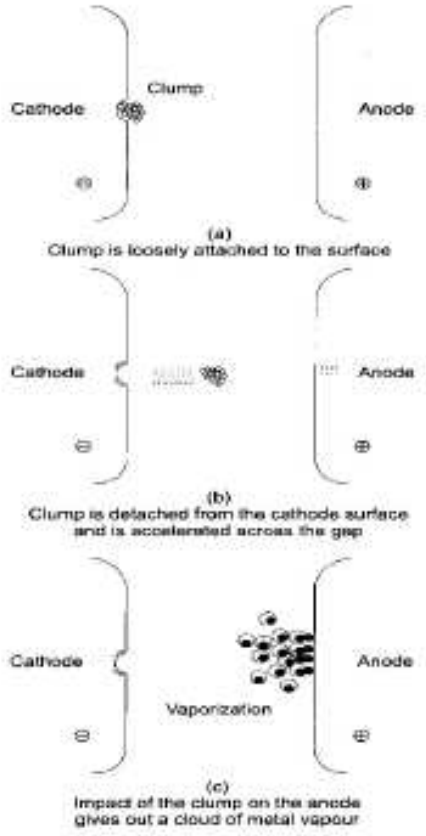

Figure 44 Clump mechanism for vacuum breakdown across large gaps

The relationship $V \propto d^{1/2}$ underlines actually the multistage structure (MAMuG) has been chosen for the ITER NBI: if we have the two systems showed in Figure 45 by simple algebraic consideration using the Cranberg's formula it is possible to understand how the subdivision in stages favours the voltage holding.

The Cranberg's approach leads to conclude how the multi-stage structure should have a voltage holding capability $N^{1/2}$ greater to the corresponding single stage one.

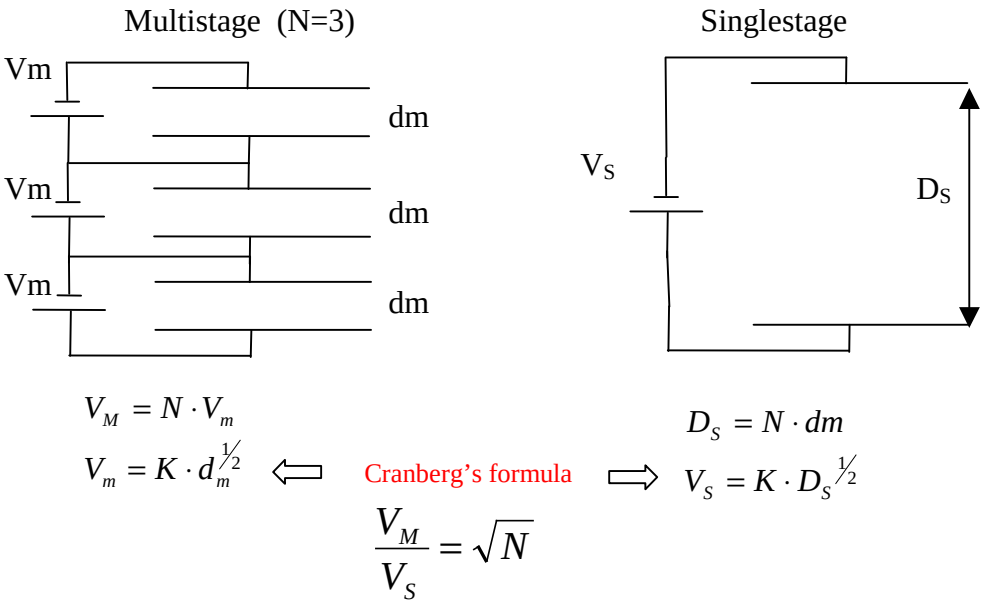

Figure 45 A simple model to compare a Single stage with a Multi Stage High Voltage device.

Although the Cranberg's explanation appears simple and useful to be directly applied in the design of a high voltage vacuum insulated system, when comparing the formula $V \propto d^{\alpha}$ with the experimental results, the exponent α is not exactly equal to ½ but it results in the range 0.5-0.625 [40,43]. Nowadays the Cranberg's proposal can't be accepted as self consistent theory, because there are still some open points concerning the physics of the process:

1) The value of C is quite difficult to be predicted from theory, it should take into account the physics of the microscopic clump formation and detachment, and as well the impact on the opposite electrode should be modelled to obtain the coefficient C.
2) A regenerative process for the clumps is necessary; in fact the micro discharges occur independently even if the voltage is decreased with respect to the maximum voltage reached.
3) The theory does not explain the above mentioned pressure effect.

Nevertheless, the matter transport phenomena at the pre-disruption phase (demonstrated by experiments in which breakdown has been induced by the deliberate particle insertion between electrodes) associated to the $V \propto d^{1/2}$ law makes the micro-particles theory as the best available candidate for the long gap case.

More recently, it has been observed [35] that at voltages in the MV range (d ≈ 30 cm) the breakdown voltage curve $V \propto d^{1/2}$ appears to saturate and the pre-breakdown current remain at very low values. Actually the breakdown event results simply a matter of time. Upon than observation, breakdown mechanism is supported to be related to the energetic electrons (hundred of KeV) hitting

the anode and penetrating deeply below the surface; in this way, the surface dissipation is difficult by gas desorbtion, particle detachment and heat conduction mechanism. A thermal instability can take place, with the occurrence of micro explosion at the anode surface. Such hypothesis solves also the issues of the regenerating process for the clumps, the weak point of the Cranberg's theory.

Finally the special case of the long-gap breakdown characterized by large pre-breakdown currents, typical of "industrial vacuum" (i.e. presence of pollution and impurities on electrodes) has been treated by Van Atta et al. [39,43]: they suggest a breakdown mechanism based on the regenerative interchange of charged atomic particles between cathode and anode, a chain reaction in which particles emitted from one electrode produce, upon impact onto the other electrode surface, particles of opposite sign. Breakdown occurs when the regeneration coefficient, product of the yields for the generation of secondary particles at the respective surface exceeds the unity. This hypothesis has been considered by other researchers [43] but they found that the secondary emission yields coefficients are much low to sustain a chain reaction.

As previously stated, Cranberg's theory appear the most suitable basis for the electrodes design; such theory has been also improved to take into account the electrodes curvature [43] leading to the formulation shown in eq. (31), being E_C the electric field at the cathode and E_A the electric field at the anode.

$$V \cdot E_C \cdot E_A^{2/3} < C \qquad \textbf{(31)}$$

To complete the overview of the mechanism governing the breakdown, an important quantity should be addressed and understood in the NBI electrostatic accelerator design: the area effect. In fact in the NBI accelerator, the electrodes at different potential have a very large area extension, approximately tens m^2.

The experimental results suggest that increasing the electrodes area the breakdown voltage decrease, Rohrbach [43] shows the empirical formula of eq. (32) to predict this effect:

$$V_{A1} = V_{A2} \cdot \left(\frac{A_2}{A_1} \right)^{\mu} \qquad \textbf{(32)}$$

where V_{S1} and V_{S2} are respectively the breakdown voltages for plane parallel electrodes with area S_1 and S_2, μ is a coefficient variable with the gap length and with the electrodes materials.

As matter of fact, very recent results in MTF of Naka have shown that the voltage breakdown difference between SINGAP and MAMuG cannot be explained only by the original Cranberg's relationship. Actually if we consider the voltage ratio, from Figure 28, it is possible, at the end of

conditioning procedure, to calculate from the experimental results $V_M / V_S \approx 1.32$ being V_M and V_S the maximum voltages obtained respectively by MAMuG and SINGAP; while the application of eq. (30) leads to $V_M / V_S \approx 1.87$.

If we compare the last accelerating and more stressed stages of MAMuG and SINGAP, we can consider as first approximation the electrode gaps equal to the grid gaps, in Figure 46, are show two sketch with the respective formulas that has been used to obtain eq. (33)

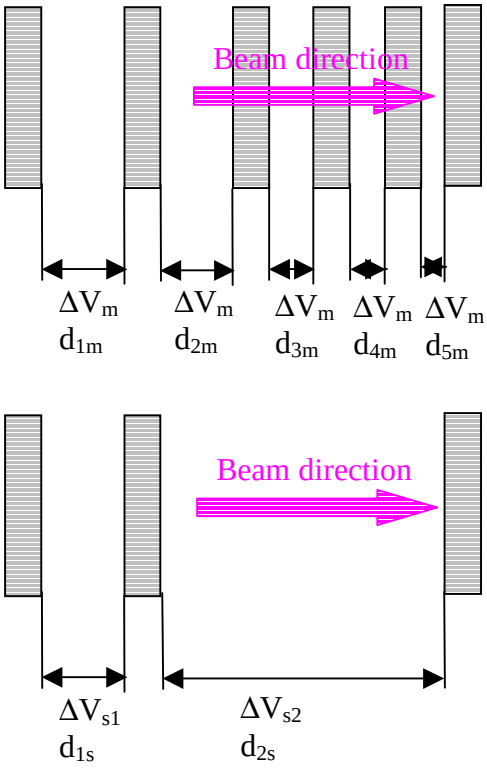

MAMuG

$$\Delta V = 5 \cdot \Delta V_m$$

$$\Delta V_m = K \cdot \sqrt{d_{5m}}$$

SINGAP

$$\Delta V_{S1} = 4 \cdot \Delta V_{S2}$$

$$\Delta V_{S2} = K \cdot \sqrt{d_{2S}}$$

$$\Delta V_S = \frac{5}{4} \cdot \Delta V_{S2}$$

Figure 46 A simple model to compare a Single stage with a Multi Stage High Voltage device to study the experimental results of the MTF.

$$\frac{\Delta V_M}{\Delta V_S} = \frac{5 \cdot K \cdot \sqrt{d_{5m}}}{\frac{5}{4} \cdot K \cdot \sqrt{d_{2S}}} = 4 \cdot \sqrt{\frac{d_{5m}}{d_{2S}}} \approx 1.87 \qquad \textbf{(33)}$$

The difference between the experimental and numerical results could be attributed only to the remarkable difference of the areas for the two electrodes configuration (SINGAP and MAMuG) being the other experimental conditions identical. As a matter of fact, the simple eq. (32) refers to

two planes electrodes with the same gaps and materials, so it isn't directly applicable to complicate multi electrodes geometries.

The area effect should be instead taken into account combining the statistical Weibull's formula with eq. (31) it leads to eq. (34), a similar approach has been proposed by [78]. In this way a generic configuration could be studied, under the point of view of the breakdown probability.

The meaning of the probabilistic approach is based on idea to ideally subdivide the electrode surfaces in several elementary areas dA. The ends of each particle trajectories identify two points on the electrode surfaces where the electric field E_C and E_A (electric field at cathode and anode respectively) can be reciprocally related and used in the formula of breakdown probability obtained by the Weibull's distribution:

$$P_b = 1 - \exp\left[-\int_A \left(\frac{V \cdot E_C \cdot E_A^{2/3}}{C} \right)^m \cdot dA \right] \qquad \textbf{(34)}$$

where C is the quantity that causes a breakdown probability of 0.632 on a couple of faced electrodes whose area is equal to unit. The coefficient m is the Weibull's module, taking into account the statistical dispersion of the data; it is easy to demonstrate that eq. (34) is compatible with eq. (32) and $m = 3/(8 \cdot \mu)$: actually if we have two system, x and y, composed by two plane parallel electrodes differing only for the electrode areas, eq.(34) leads to eq.(35) in case of equal breakdown probability.

$$\left(V_X \cdot E_{CX} \cdot E_{AX}^{2/3} \right)^m \cdot A_X = \left(V_Y \cdot E_{CY} \cdot E_{AY}^{2/3} \right)^m \cdot A_Y \qquad \textbf{(35)}$$

eq. (35) can be written as shown in eq (36) in case of same electrode gaps d_x=d_y it:

$$V_X^{8 \cdot m/3} \cdot A_X = V_Y^{8 \cdot m/3} \cdot A_Y \qquad \textbf{(36)}$$

The previous equation is compatible with eq.(31) . Further details about the statistic approach will be discussed in sec 2.4 where the same approach will be used to carry out the structural analyses about the ceramic insulators.

In a complex multi electrode system the association E_C and E_A could appear not univocally defined, but if we consider the possibility to exchange charge particles from the electrodes surfaces starting with zero velocity, the eq.(23) (Chapter 2) shows that the ratio X/L is univocally defined by the electrodes shapes (see Figure 47). Although we don't know exactly the particle (clump) mass, if we assume that the initial velocity is zero, we can affirm that the trajectory doesn't depend on voltage or particles mass; therefore, each point on the electrode surfaces has a corresponding image which doesn't depend on mass or applied voltage V.

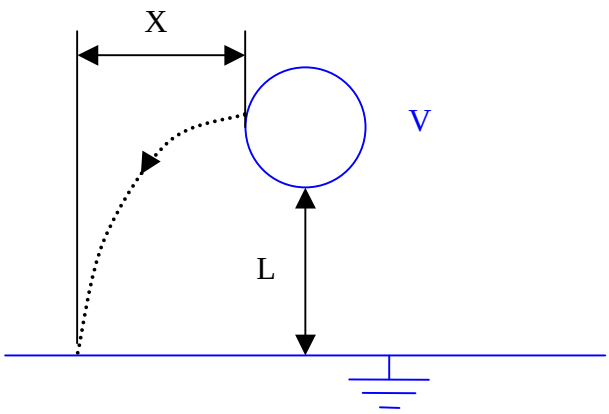

Figure 47 Univocal correlation between cathode and anode for a simple electrode configuration.

The procedure to validate the eq. (34) is to compare several results obtained with different geometries and to check if the Weibull's coefficients C and m are constant; being fixed all the other "boundary condition" , e.g. materials , surfaces treatments, pressure and conditioning procedure.

As mentioned before, another important factor that allows reaching higher voltages in a large gap system is the pressure effect. Figure 48 shows the pressure influence for three gap lengths. It is worth noting that in range pd= 10^{-2}-10^{-1} [Pa·m] there is a maximum in voltage holding. The data represented by the green and blue curves have been obtained at Naka in the MTF experiment with SINGAP configuration and without VIBS, although electrodes configuration is far from being simple.

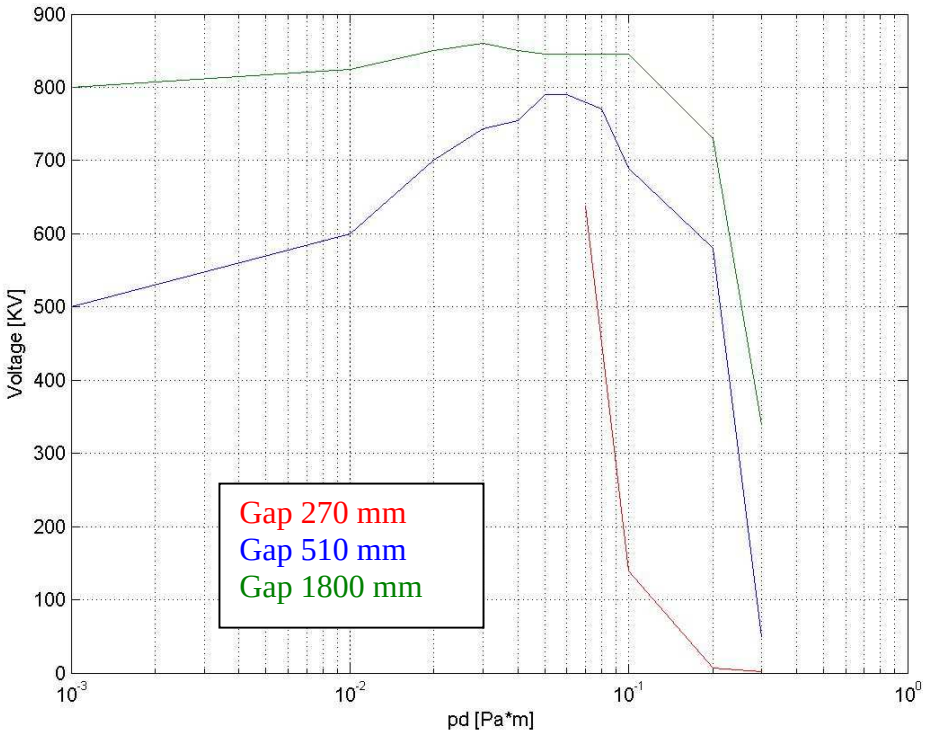

Figure 48 Pressure effect for three gap length [79, 25]

The conditioning process is the treatment to increase the voltage from zero up to the maximum. The procedure consists to apply the voltage step by step (see Figure 49). The current at each step reach a limit; as mentioned above, the long gap case is characterized by very low currents that flow thought the electrodes (< 10^{-7} A), nevertheless repetitive random micro-discharges appear raising the voltage: this phenomenon is compatible with the clumps hypothesis, where the micro-particles transfer energy and electric charge across the electrode gaps.

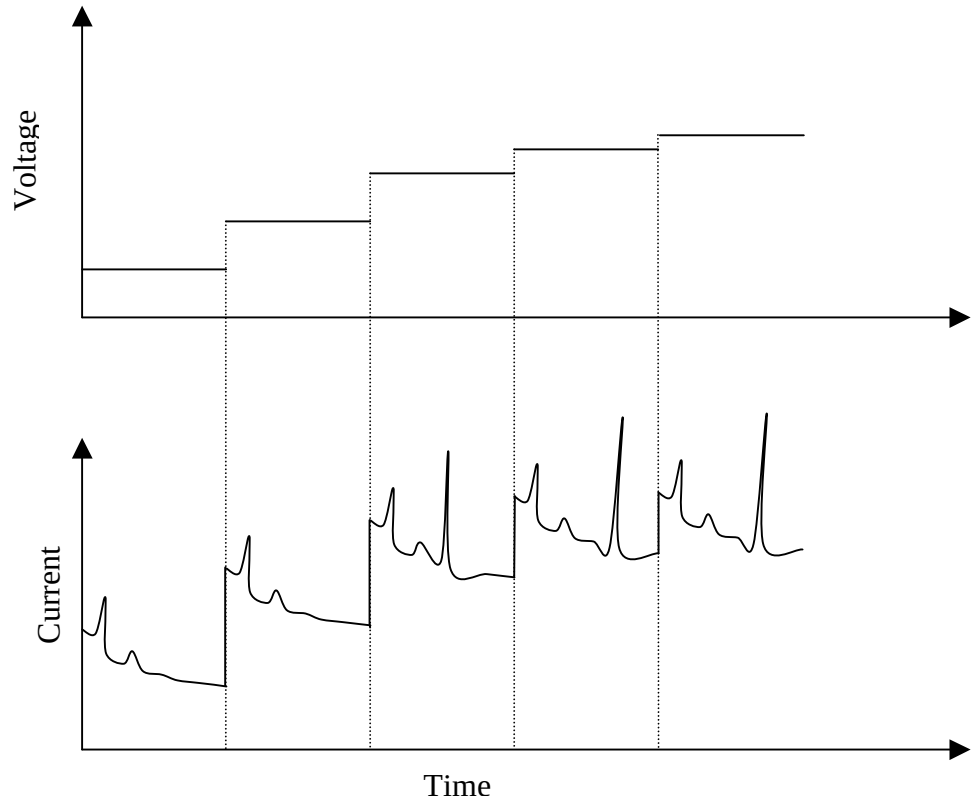

Figure 49 A schematic illustration of the conditioning procedure

In practice the conditioning operation, is composed of a first conditioning phase at low pressure where the DC voltage is applied slowly, typically for several hours before to reach the limit (corresponding approximately to the Cranberg's $V = K \cdot \sqrt{d}$ theory); then a gas inflow allows (H or He) allows to reach quickly the maximum. An example of this procedure is shown in the MAMuG plot of Figure 28, after 46-47 hours of conditioning at lower pressure the gas injection allows to increase the breakdown voltage from 650 to 800 kV in few time.

2.3.2 Solid insulation

Any high voltage system adopts solid insulators to separate different environments, or to support high potential electrodes. The accelerator for the ITER NBI utilizes several solid insulators made of high purity alumina, to withstand (200kV) in each accelerating stage, in order to reach the voltage of -1MV by 5 stages. The voltage hold-off capability of such solid insulators placed in vacuum is commonly less than that of a vacuum gap of similar dimensions and it depends upon many parameters: the material choice, the geometry, and the surface finish, the interface between the insulator and the electrodes, the vacuum level, the presence of ionized particles; as matter of fact, insulation breakdown occurs mainly along the surface. The surface flashover is widely assumed to begin with the emission of electrons from the cathode triple point [51].

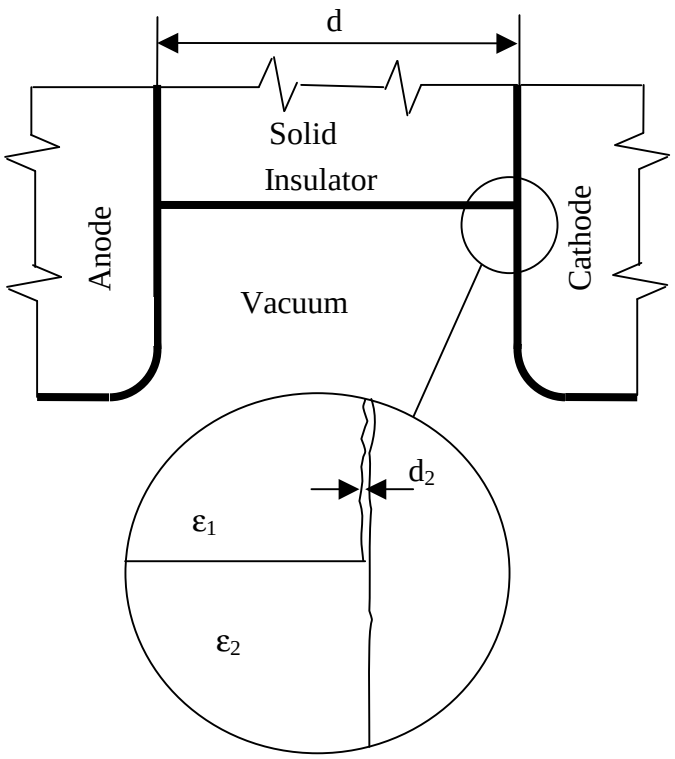

Figure 50 A sketch of the triple point junction

The triple point, shown in Figure 51, is the interface where insulator, cathode, and vacuum are in close proximity: the electric field at this point is intensified in comparison with the electric field in the presence of vacuum only. In order to understand this critical aspect, a simple model can be used starting from Figure 50: the interface between insulator and metallic electrode isn't a perfect contact, small and irregular gap always existing between the materials. A simplified electric model

consists of two plane parallel capacitors connected in series: the first one has a gap length $d_1 \approx d$ and a permittivity ε_1; the second one is characterized by d_2 and ε_2 respectively.

The electric field in the small vacuum gap is amplified by a factor equal to the ratio $\varepsilon_1/\varepsilon_2$: in this case, with an insulator made of alumina, the ratio is about 10. But the effective geometry is more complex and needs numerical approach. In appendix A the FEM approach to simulate the triple junction is discussed with more detail.

The mechanism [51] that explains the discharge in such configuration, is an electron cascade along the insulator surface (see Figure 51): the electrons emitted from the triple junctions strike the surface of the insulator producing additional electrons by secondary emission, some of these secondary electrons will again collide with the insulator surface producing tertiary electrons and so on until the breakdown occurs. This phenomenon is commonly called Secondary Electron Emission Avalanche (SEEA).

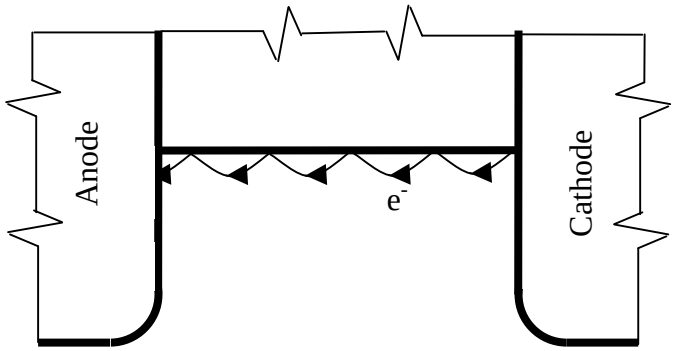

Figure 51 Scheme of the most confirmed mechanism about the surface flashover

The big amount of charge on the insulator surface causes distortion of equipotential lines and the non-linearity of the described phenomena implies not only several difficulties to simulate the physics that controls the discharge, but also a time dependent mechanism that influences the voltage holding of the whole system, including a memory effect as concern the conditioning procedure. Some authors [51] suggested a model where the layer of adsorbed gas that normally cover the ceramic surface plays an important role in the formation of the discharge; the electron avalanche extracts the trapped gas forming a substrate of partially ionised gas around the insulator, positive ions drifts toward the cathode to enhance the formation of electrons from the triple point. The trigger for the breakdown along the surface of a solid insulator is the particles emission from the triple points. As concern the design point of view the criteria adopted are essentially two:

1) To limit the electric field at the triple point: the limit of 0.1MV/m [53] has been considered for the triple point between alumina and stainless steel, for DC application in steady state. It

is interesting to note that the angle between ceramic surface and electrode influences the electric field at the triple point and as consequence the voltage holding [51]. In the electrostatic accelerator of ITER cylindrical ceramic insulators have been adopted.

2) To limit the tangential electric field on the ceramic surface. A conservative limit of 1MV/m [53] has been considered along the insulator surface. It is important to observe that the limit should decrease with insulator diameter [43].

The ceramic-metal junction should be well designed; particular attention shell be paid in order to avoid the presence of voids in the interface ceramic-metal, e.g. with the use of a compliant layer.

The simple insulator, as shown in Figure 51, surely has a rather low voltage hold-off capability: a possible solution to increase the performance of such system is the application of a couple of electrostatic shields on both electrodes. The role of the shields is to reduce the electric field at the triple junctions. Although the previous explanation involves only the emission of electrons at the cathode, it has been demonstrated that also the anode in some circumstances can initiate the discharge, thus it is necessary to shield all the triple junctions both for cathode and anode as well.

An example of electric shield is shown in Figure 52, (the equipotential lines are in red) it is possible to see that the shields reduce the dielectric stress at the triple junctions but, in the central part of the ceramic insulator, the electric field is intensified.

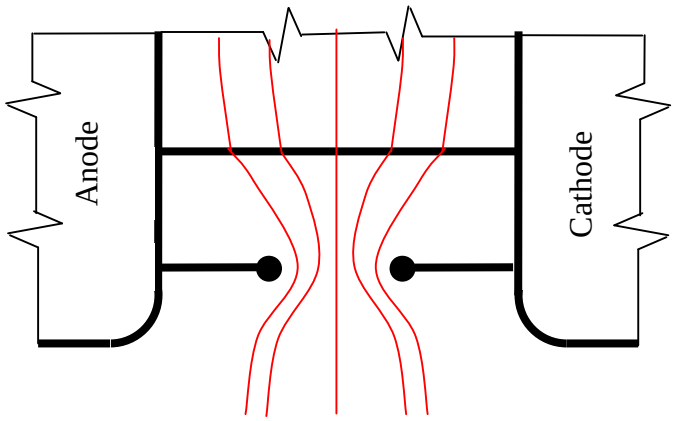

Figure 52 A proposal of electrostatic shield to screen both the triple junctions

Application of the triple junction shielding is shown in Figure 53, where the numerical results of the electric field distribution in the MTF without VIBS are reported.

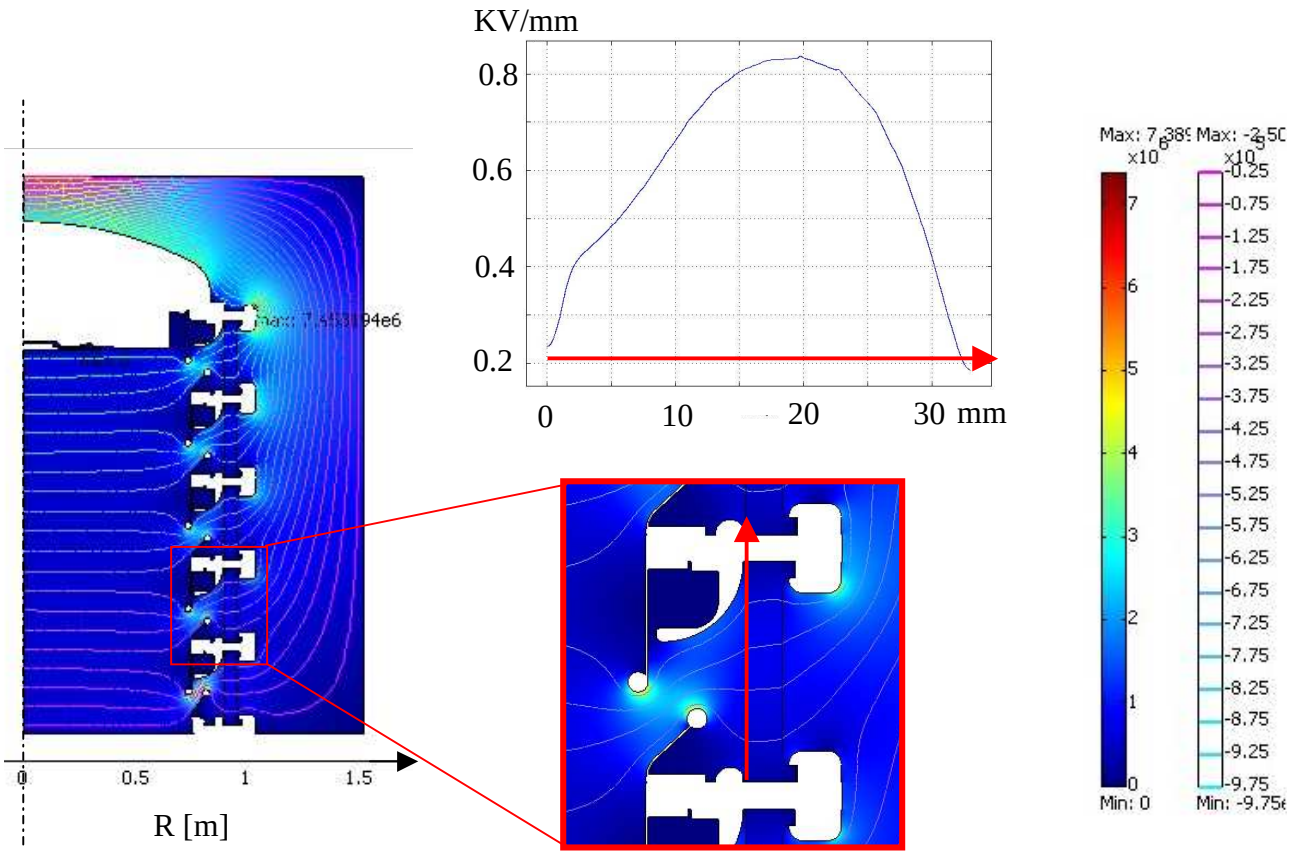

Figure 53 The electrostatic shields in the MTF (design information kindly supply by JAEA NBI group).

It can be noted that the electrostatic shields are not symmetric at the top and at the basis of the FRP rings, because in this case it has been preferred to improve the shield effect at the cathode.

2.4 Mechanical design criteria and analyses

The mechanical analyses performed for the accelerator at RFX have been mainly focused on the thermo-mechanical aspects related to grid cooling and the design of electrical insulators.
With the first activities, suitable cooling circuits have been identified to guarantee the extraction of the power deposited on the grids, also with simulations of the coupled hydraulic and thermo-mechanical behaviour of the grids. The grids made of OFHC Cu have been verified against the oligo-cyclic fatigue and a substantial work has been devoted to identify a suitable criterion to evaluate the fatigue life for these components [47]. It is also important to remind that the aperture displacements due to grid heating strongly influence the quality of the beam; suitable apertures pre-offsets can be foreseen to compensate for this phenomenon, but the results of numerical analyses and physics simulation should be also supported by experimental campaigns.
The following sections concern the design of electrical post-insulators and the related procedure generally applicable to brittle components. The criteria and procedures have been developed to carry out in particular the analyses of alumina post insulators that sustain the 5 acceleration stages and of the large 200 kV insulating rings inside the 1MV bushing connecting the accelerator to the high voltage transmission line.
The 1 MV high voltage bushing for ITER NBI is composed of five stages each of them insulated by means of concentric rings respectively made of fibre-reinforced plastic and advanced ceramic material brazed to metal plates.
The fabrication of large ceramic rings, having outer diameter of about 1.6 m and brazed to metal plates, is a technological challenge for the present knowledge, capabilities and production lines of manufacturers all over the world.
The main efforts during the PhD period have been dedicated to studies, thermo-mechanical analyses and optimisation of large ceramic rings during the brazing procedure.

Design of brittle ceramic components by statistical approach

Ceramic materials are generally brittle, and nominally identical specimens of brittle materials may exhibit large variations in the fracture stress. The main differences between ceramic and metallic materials are the large dispersion of ceramic material strength and the absence of plastic stress redistribution for brittle components. If the same local criterion used for metallic materials is applied to verify a ceramic component, the required safety factor would not be guaranteed, being strongly affected by the statistical presence of defects in the volume of the brittle material.

An approach based on the volume stress integrals is typically proposed to verify the ceramic materials [57].

On the basis of experimental tests on a limited number of specimens uniformly loaded in simple tension or pure bending, the probability of failure can be calculated for structural members of different sizes and shapes and under completely different loading conditions. The tool for accomplishing this is fracture statistics. The first important contribution to this subject was given by Weibull in 1939 [58] and his theory is still the basis for most calculations in this field. He exploited the analogy between a stressed brittle structure and a loaded chain, which breaks when the strength of its weakest link is exceeded. The equations for the Weakest Link Theory (WLT) can be obtained dividing the stressed component in infinitesimal volumes; each volume has a failure probability $(\Delta P_f)_i$, so the survival probability is $(Ps)_i = 1 - (\Delta P_f)_i$; the overall probability of survival Ps is the product of the individual probabilities of survival Ps_i,

$$Ps = \prod_i Ps_i = \prod_i \{1 - (\Delta P_f)_i\} \cong \prod_i \exp\left[-(\Delta P_f)_i\right] = \exp\left[-\sum_i (\Delta P_f)_i\right] \quad \textbf{(37)}$$

The failure probability in the infinitesimal volume (ΔPf)i can be expressed by the product between the failure probability in the unit volume $f(\sigma)$ and the infinitesimal volume dV, so $(\Delta P_f)_i = f(\sigma) \cdot dV_i$. Thus the probability of failure of the whole component is given by (38)

$$P_f = 1 - P_S = 1 - \exp\left[-\int f(\sigma) \cdot dV\right] \quad \textbf{(38)}$$

In the case of a unit volume subjected to a uniform stress field eq. (38) can be simplified

$$P_f = 1 - \exp[-f(\sigma)] \quad \textbf{(39)}$$

The failure probability $P_f(\sigma)$ is an increasing monotonic function of σ, as well the $\frac{\partial P_f(\sigma)}{\partial \sigma}$ is the distribution function for the material strength (see Figure 54).

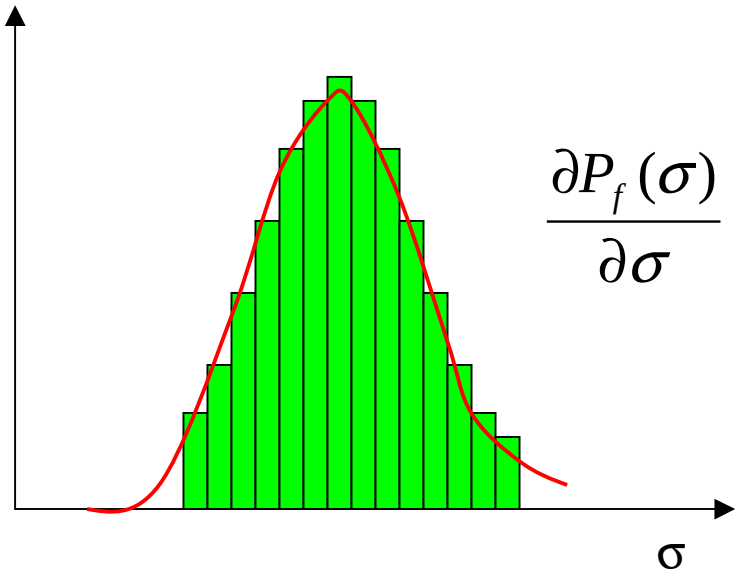

Figure 54 Example of distribution function for the mono-axial strength of ceramic material

At first one might be inclined to expect this function to be Gaussian. Actually it is possible to demonstrate that the Gaussian distributions are incompatible with the WLT.

By deriving eq. (34) we obtain eq.(40):

$$\frac{\partial P_f}{\partial \sigma} = f^{|}(\sigma) \cdot \exp[- f(\sigma)] \qquad \textbf{(40)}$$

If eq.(40) was the Gauss's distribution, it should be $\frac{\partial P_f}{\partial \sigma} = A \cdot \exp\left[- a \cdot (\sigma - b)^2\right]$; but the latter is incompatible with eq.(39), because if $f^{|}(\sigma)$ is a constant (equal to A), $f(\sigma)$ cannot be a quadratic function. Weibull introduced the distribution function that satisfies the previous requirement: he assumed $f(\sigma) = (\sigma/\sigma_0)^m$. In this case there are two parameters that describe the material: σ_0 and m, the first one is the stress that corresponds to a failure probability of 0.632=1-exp (-1) for a unit volume subjected to a uniform mono-axial stress field, while the second one is the Weibull's module. So eq. (41) becomes

$$P_f = 1 - P_S = 1 - \exp\left[- \int \left(\frac{\sigma}{\sigma_0} \right)^m \cdot dV \right] \qquad \textbf{(41)}$$

The distributions of failure probability $\frac{\partial P_f}{\partial \sigma}$ are shown in Figure 55 for different values of m and σ_0.

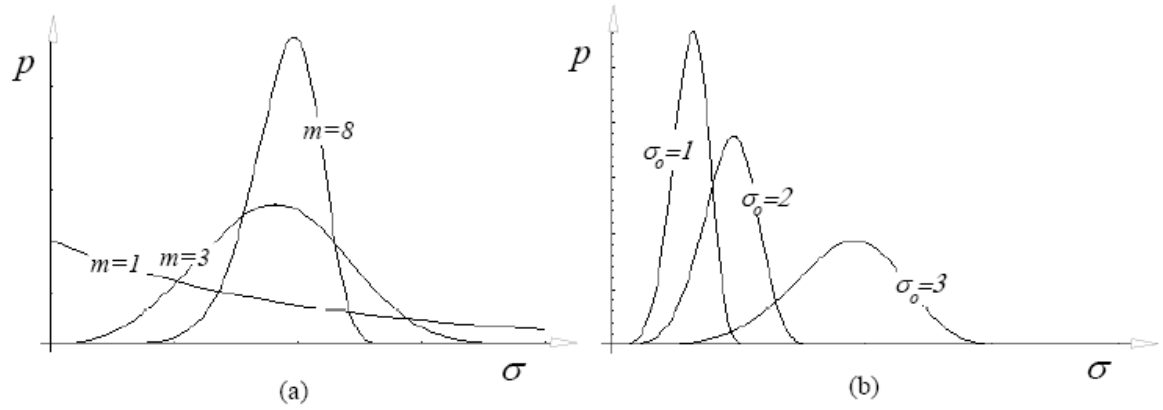

Figure 55 Weibull's distributions: influence of s_0 and m

It can be noted that higher values of m imply lower dispersion of σ: from the numerical point of view this means to amplify the local effects of the stress field in the failure probability calculation eq. (41) ; in other words the limit $m \to \infty$ corresponds to the punctual criterion discussed above.
On the other hand, the proposed approach takes into account the spread in the strength that is strictly related to the size and distribution of flaws and defects inside the material.

Fracture mechanics, using a deterministic field approach, affirms that the necessary condition to propagate a defect with initial dimension equal to "a" is (considering only the first mode) $K_I \geq K_{IC}$.

The coefficient K_I is representative of the stress field amplitude in proximity of defect, while K_{IC} is the correspondent limit dues to the material.

This inequality can be rewritten, in case of a defect that does not interact with the others, as follows:

$\sigma\sqrt{\pi \cdot a} \geq K_{IC}$, where σ is the mono-axial stress that would be present if the defect would not exist.

If in the unity volume there are several defects with different dimensions and oriented to be stressed by first opening mode, the failure stress in the unit volume is reported in eq.(42)

$$\sigma = \frac{K_{IC}}{\sqrt{\pi \cdot a}} \qquad \textbf{(42)}$$

Where "a" is the largest dimension of the defects that are contained in such volume.

Combining Weibull's equation (41) with eq. (42) it's possible to obtain a new expression, where P is not the failure probability but the probability that a defect whose dimension is larger than "a" exists inside the unit volume.

$$P = 1 - \exp\left[-\left(\frac{K_{IC}}{\sigma_0 \cdot \sqrt{\pi \cdot a}} \right)^m \right] \quad \textbf{(43)}$$

So $\frac{\partial P}{\partial a}$ represents the statistical distribution of defects dimension inside the material. Figure 56 shows a possible distribution evaluated for Alumina with m=10 and σ_0= 312 MPa for 1 mm^3.

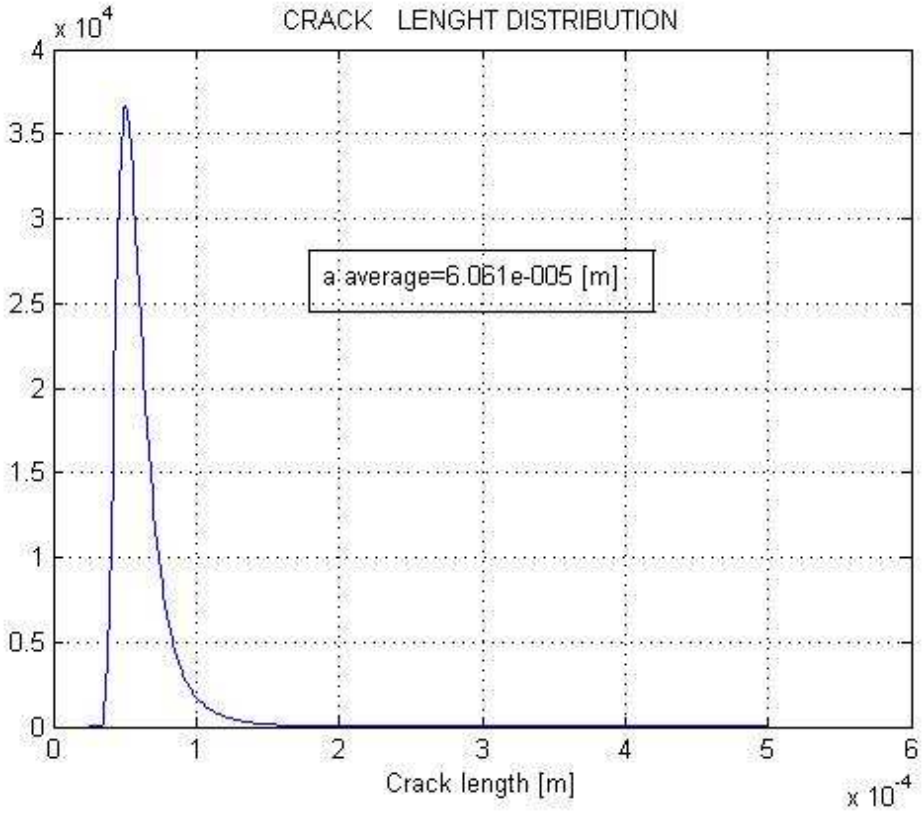

Figure 56 Crack length distribution estimate

The average dimension of the defects can be simply evaluated by the first moment of the cracks distribution:

$$a_{average} = \int_0^{\infty} a \cdot \frac{\partial P}{\partial a} \cdot \partial a \quad \textbf{(44)}$$

In this case the average cracks dimensions should be 0.06 mm and this result seems consistent with experimental observations [59,60].

Up to now we have considered only the mono-axial stress field, while in reality the stress field can be multi-axial. In order to take into account this aspect, the Principle of Independent Actions (PIA) has been adopted for the calculation of failure probabilities. The stress tensor is transformed into its three principal stresses and each of the three principal stresses is assumed to act independently [57 and 62]. Thus equation (38) is transformed into eq (45):

$$P_f = 1 - \exp\left[-\int \left(\frac{\sigma_1}{H(\sigma_1)\cdot\sigma_0} \right)^m + \left(\frac{\sigma_2}{H(\sigma_2)\cdot\sigma_0} \right)^m + \left(\frac{\sigma_3}{H(\sigma_3)\cdot\sigma_0} \right)^m \cdot dV \right] \qquad \textbf{(45)}$$

where σ_i i=1,2,3 are the principal stresses, and H(σi) is a function considering that compression stresses lead to lower failure probability than tensile stresses. H is equal to 1 if σi >0 otherwise $H(\sigma_i)$=-8 .

The design based on the proposed criterion requires the knowledge of m and σ_0; these parameters should be obtained by specific tests on materials. The material properties should be obtained from available statistical data of mechanical strength or with proper mechanical tests on small samples, as indicated by Standards for qualification of advanced ceramic materials [67-77].

Numerical models to simulate the brazing between ceramic and metal

Although the procedure to evaluate the ceramic failure probability is well consolidated, several numerical and practical complications come from the analyses of metal-ceramic brazed connections.

In brazing only the added brazing alloy melts and the base material is wetted in its solid state by the liquid brazing alloy. A prerequisite for brazing is a good and uniform wetting of the base materials by the brazing alloy.

During the brazing process the components are heated under vacuum up to the melting temperature of the brazing alloy and then cooled down to room temperature. The difference between thermal expansion coefficients of metal and ceramic is the cause of thermal stresses in both materials during the cooling phase and of residual thermal stresses at room temperature.

Then the stress field inside the ceramic material is the superposition of the stress field induced by the external loads and the residual thermal stresses arising during the brazing procedure.
This is the reason why the complete numerical analysis of the brazing cycle (heating and cooling) has to be carried out.
The following three phases are considered for simulations:

• heating of the detached parts with free thermal deformations up to the maximum temperature;
• coupling of nodes at the brazed sections as displaced after heating;
• cooling down of the “brazed” model.

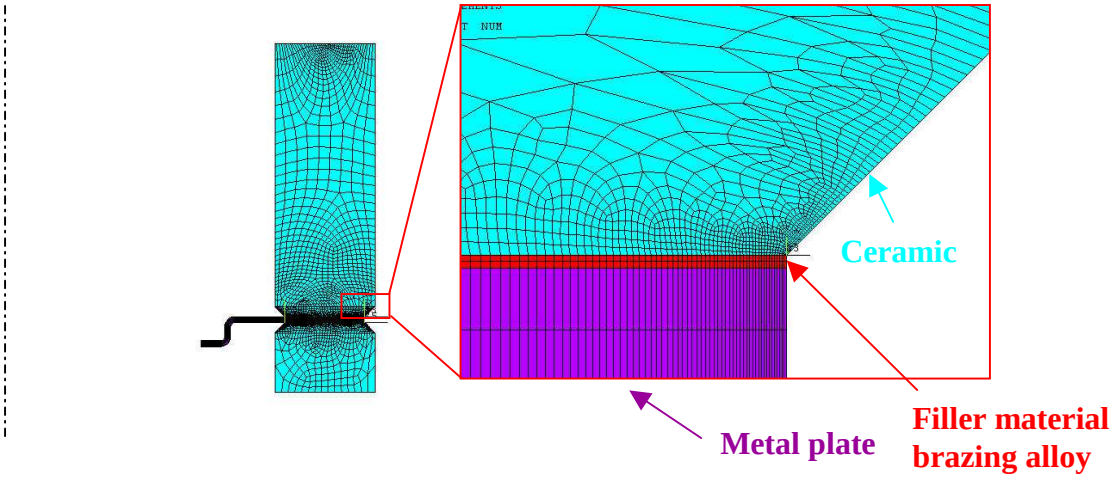

Figure 57 2D axial symmetrical model adopted to simulate the brazing procedure for the large ceramic rings inside the NBI bushing

The 2D axial symmetrical ANSYS® model that has been adopted to simulate the brazing procedure between the alumina rings and the kovar plate is shown in Figure 57; the model and the related results will be introduced and described with more detail in section 4.2. A suitable routine has been developed in order to couple the nodes at the interface between the different materials and to run several step by step analyses through the whole brazing cycle shown in Figure 58.

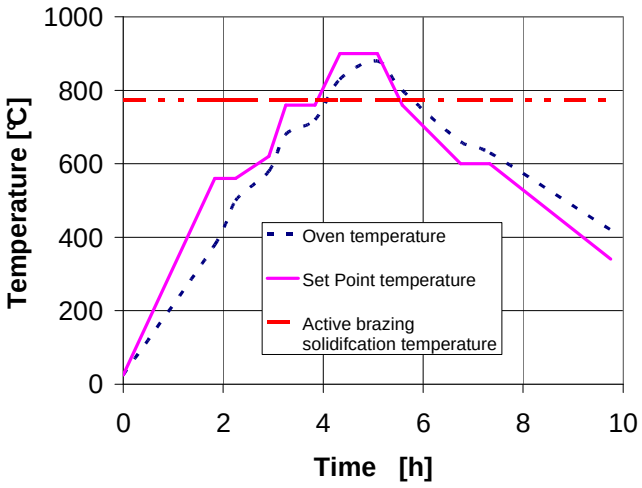

Figure 58 Brazing cycle, temperature vs. time

For each step it is possible to evaluate the stress field and the failure probability by eq. (45).

A simple 1D model illustrated in Figure 59 can be used to understand how the material proprieties influence the stress field in each part.

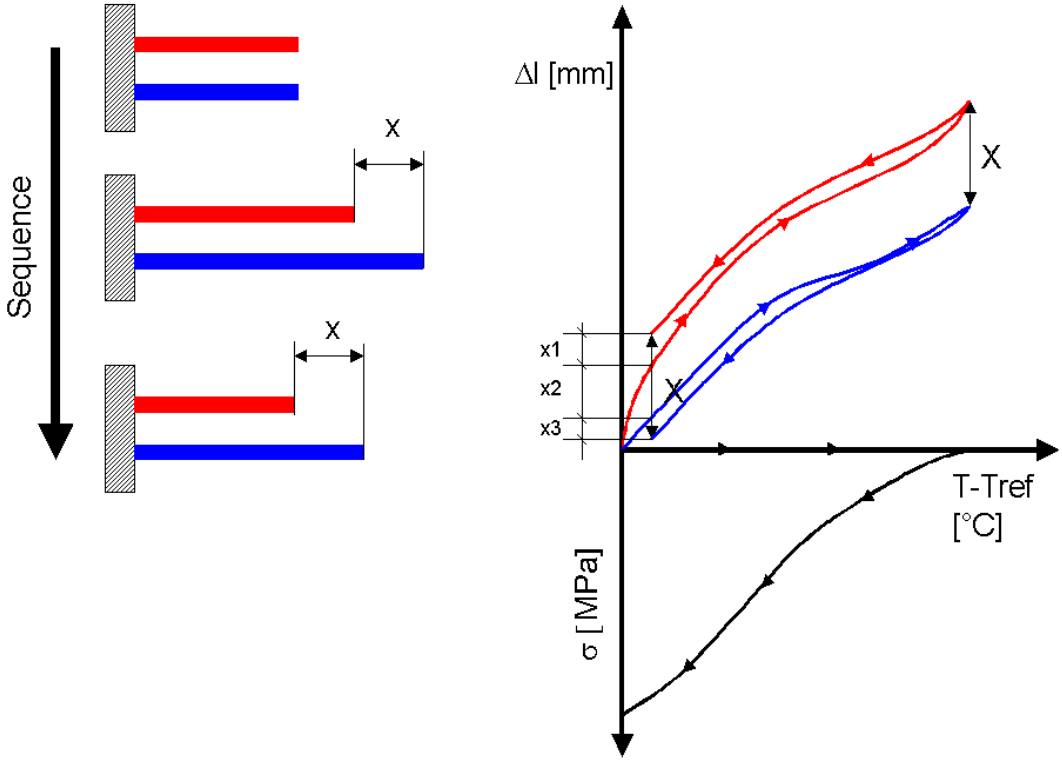

Figure 59 A simplified 1D model to determine the influence of material parameter in the stress field

The cantilever bars showed in Figure 59 are made with two different materials and they have the same initial length at room temperature. When the temperature increases up to the melting point of the filler material the bars have different displacements $\Delta l = l_0 \cdot \alpha(T) \cdot (T - T_{ref})$ because the

materials have different thermal expansion coefficients α, being the thermal expansion coefficients evaluated by the secant method starting from T_{ref}

When the filler material is solidified, the ends of the bars are kept at the same relative position $X = l_0 \cdot \left[\alpha_1(T_{melt}) - \alpha_2(T_{ref})\right] \cdot (T_{melt} - T_{ref})$. The relative distance X is also kept during the following cooling down phase and the relation $X = X1 + X2 + X3$ is valid for any intermediate temperature during this phase. In particular, looking at Figure 59 it is possible to write $X1 = \frac{F \cdot l_o}{A_1 \cdot E_1}$, $X3 = \frac{F \cdot l_o}{A_2 \cdot E_2}$ and $X_2 = l_0 \cdot \left[\alpha_1(T) - \alpha_2(T_{ref})\right] \cdot (T - T_{ref})$. After few simple calculations eq. (46) and eq. (47) are obtained:

$$F = \frac{\left[\alpha_1 \cdot (T_{melt}) - \alpha_2(T_{ref})\right] \cdot (T_{melt} - T_{ref}) - \left[\alpha_1(T) - \alpha_2(T)\right] \cdot (T - T_{ref})}{\left(\frac{1}{A_1 \cdot E_1} + \frac{1}{A_2 \cdot E_2}\right)} \quad \textbf{(46)}$$

$$\sigma_1 = \frac{F}{A_1} = \frac{\left[\alpha_1 \cdot (T_{melt}) - \alpha_2(T_{ref})\right] \cdot (T_{melt} - T_{ref}) - \left[\alpha_1(T) - \alpha_2(T)\right] \cdot (T - T_{ref})}{\left(\frac{1}{E_1} + \frac{A_1}{A_2 \cdot E_2}\right)} \quad \textbf{(47)}$$

The general result that can be obtained by the proposed model is that each stress field σ for two linear elastic materials is proportional to the driven term D.

$$D = \left[\alpha_1(T_{melt}) - \alpha_2(T_{ref})\right] \cdot (T_{melt} - T_{ref}) - \left[\alpha_1(T) - \alpha_2(T)\right] \cdot (T - T_{ref}) \quad \textbf{(48)}$$

The proportionality $\sigma \propto D$ has been verified by FEM analyses (Figure 60). The model has been developed in presence and in absence of the thin interlayer material that simulates the brazing alloy, the figure shows the linear correlation between a generic stress component and D, being the results obtained by finite element analysis.

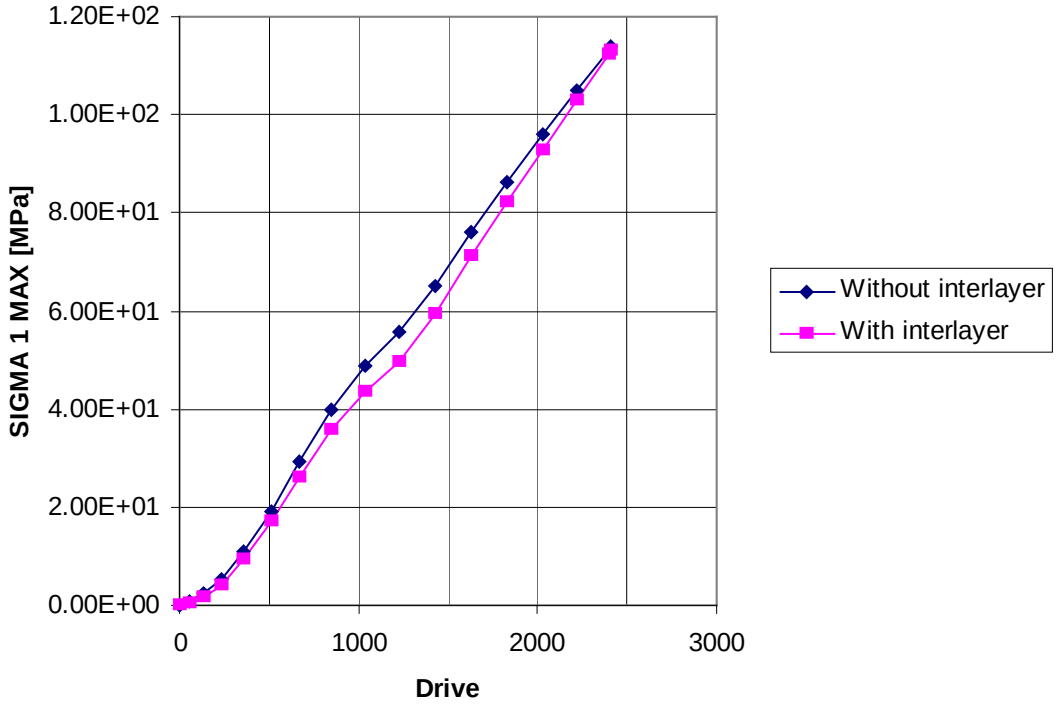

Figure 60 Linear correlation between D and a generic stress component in a suitable FEM

Imposing null stresses at room temperature (Tref) would mean to set equal to zero the numerator of eq. (47) when T=Tref. It is then possible to conclude that the condition with no stresses at T=Tref is obtained cancelling the relative displacement at the solidification temperature; in other words, a criterion to choose the couple metal-ceramic in order to minimize the stresses at room temperature is represented in eq. (49)

$$\alpha_{ceramic}\left(T_{melt}\right)=\alpha_{metal}\left(T_{melt}\right) \tag{49}$$

Singularity treatment and estimation of the crack length

The stress distribution in correspondence of the brazed interface presents high local stresses and stress gradients at the edges of the joint interface. The numerical values calculated with F.E. analyses are affected by large errors due to numerical approximations. The errors can be almost negligible or very important depending on geometry, material properties and mesh refinement. It has to be noted that the stress values should be actually infinite in case of linear elastic materials [61] and anyway highly localized in case of non-linear materials and/or non-linear complying interlayer.

Since the failure probability calculated using Weibull's criteria is influenced by stress singularities and mesh refinement, a specific procedure is needed to overcome the problem. A method to adjust the local peak stresses has been proposed in [62]. The main assumption is to limit or neglect stresses at a distance from the edge lower than half of the average flaw size in ceramic material (hundredths of mm). In fact the statistic Weibull's method can be only applied to volumes that contain a large number of flaws or defects, and would give wrong estimates considering very high stresses in regions having dimensions comparable with the average flaw size. Anyway a perfect sharp corner as adopted in the model does not correspond to the actual geometry where a smoothed corner is indeed present and local plastic deformations or debonding can adjust the peak stresses in very small areas. For these reasons the failure probabilities of the rings have been calculated taking into account the whole ceramic volume with the exception of the elements located inside two small edge areas identified by a circle centred on the corner and having a radius equal to the average flaw size in ceramic material. Figure 61 shows the effect of the excluded area on the failure probability computation. If the failure probability is constant within a radius lower than the average flaws size, the criterion affirms that this is the actual failure probability.

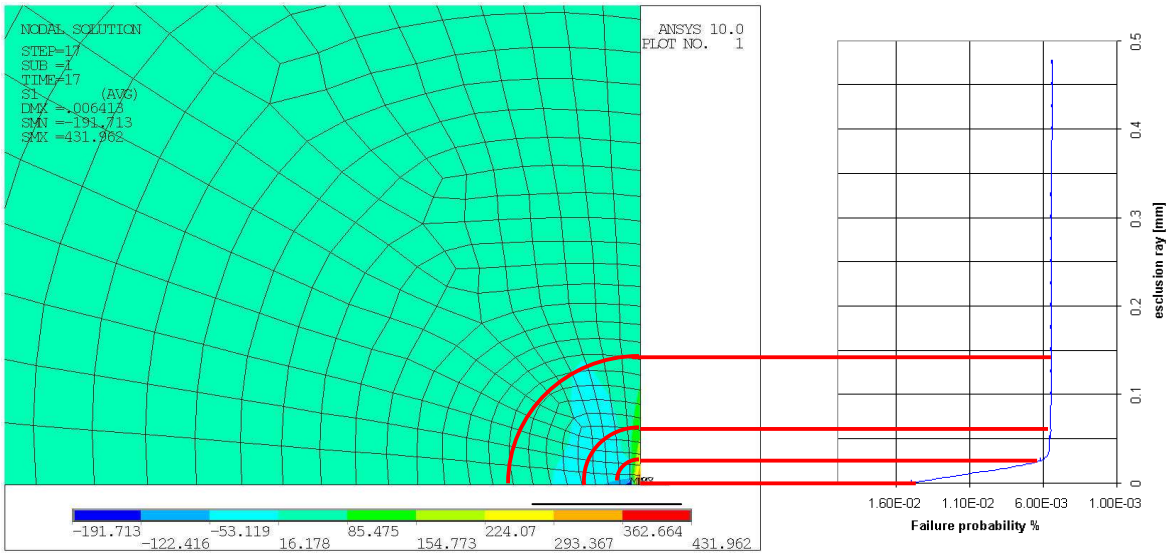

Figure 61 Effect of the exclusion area on the failure probability computation

The critical flaw size of ceramics can be obtained experimentally or by a numerical approach adopting eq (44). Checks have been carried out comparing the results obtained with different mesh refinements and radius of exclusion area. Independence of failure probability on mesh refinement is achieved neglecting a corner volume having the extension comparable with the critical flaw size as shown in Figure 61.

Chapter 3: Structural analyses of accelerator ceramic insulators

3.1 Introduction

The high dielectric strength, the chemical stability, the vacuum compatibility and the relatively high mechanical strength, make the advanced ceramic the appropriate material to link parts at different potentials. The high purity alumina is the material that satisfies the mentioned requirements. It is commonly used to fabricate small and medium size parts for vacuum applications.
Several ceramic components are parts of the ITER NBI accelerator and high voltage bushing.
In detail there are:

- five large ceramic rings in the high voltage bushing to insulate each stage;
- 64 post insulators, placed inside the accelerator to insulate the grid support frames;
- Several little ceramic breakers and feedthroughs in the plasma source and the vacuum vessel.

3.2 The large ceramic rings for the 1MV bushing

The high voltage bushing shown in Figure 62 is the interface between the gas insulated transmission line and the ITER primary vacuum. It provides all the electrical, gas and cooling water services to the beam source coming from the transmission line.

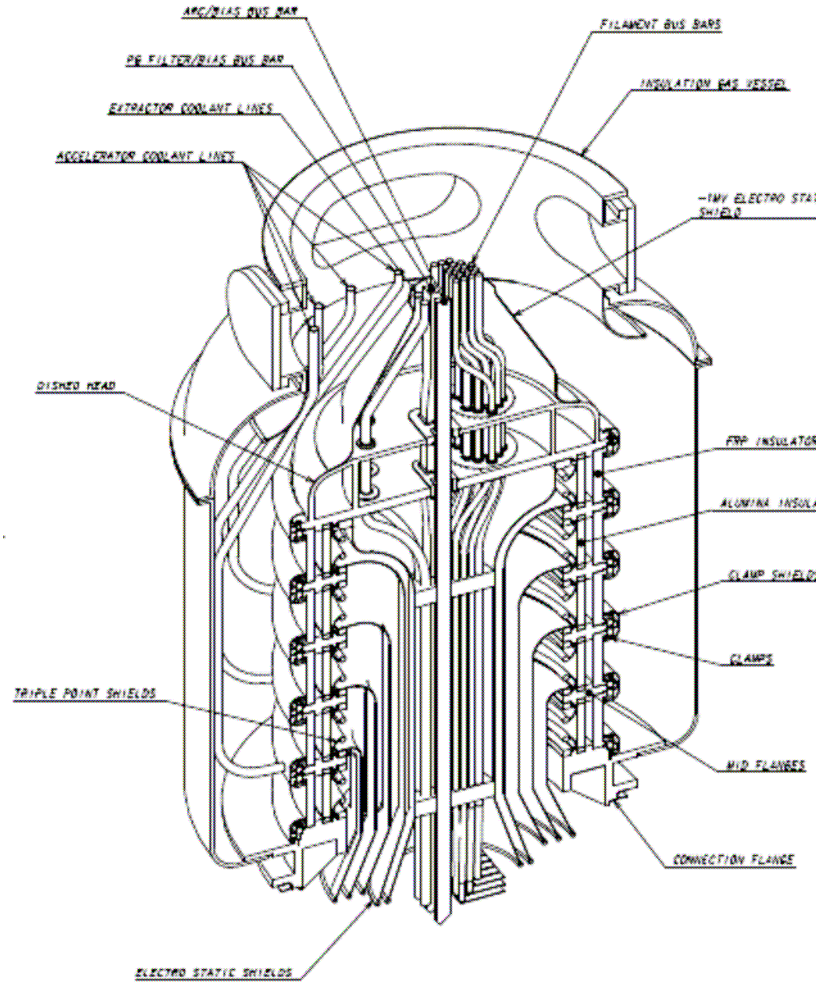

Figure 62 HV bushing cutaway isometric view

The high voltage bushing is composed by five insulated stages; each stage includes:

- An inner insulator ring joined and sealed to the stainless steel flange;
- An outer insulator ring joined and sealed on the flange using an elastomer o-ring seal.

The inner ring has the function of electrical insulation and containment barrier withstanding the pressure difference between vacuum and the interspace guard gas (N2 at 1.0 MPa pressure).

The internal insulator ring of the HV bushing is shown in Figure 63.

It is composed of:

• an alumina cylinder (outer diameter 1.56 m, thickness 50 mm, height 290 mm);

• Two kovar® sheets for vacuum sealing, to be welded in situ to the SS massive flanges;

• two alumina back-up rings (50x29 mm), having the function of limiting residual stresses during brazing.

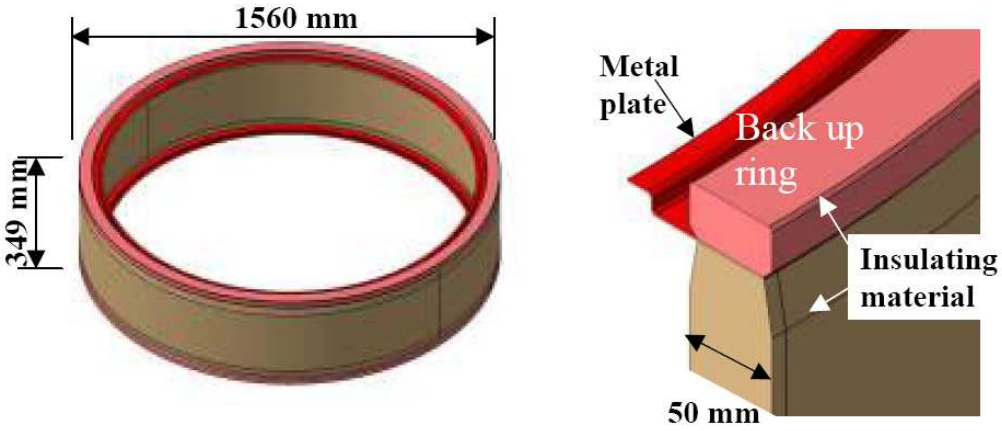

Figure 63 3D isometric view of the internal ceramic insulator ring for the high voltage bushing

The challenging problem related to the fabrication of large insulator rings has been recently solved by the JAEA NBI team. An innovative process for the fabrication of large ceramic rings has been developed in close collaboration with the manufacturers: a new procedure for the Cold Isostatic Pressing CIP, necessary before sintering, has been proposed [63]. A comparison between the conventional and the new CIP is shown in Figure 64:

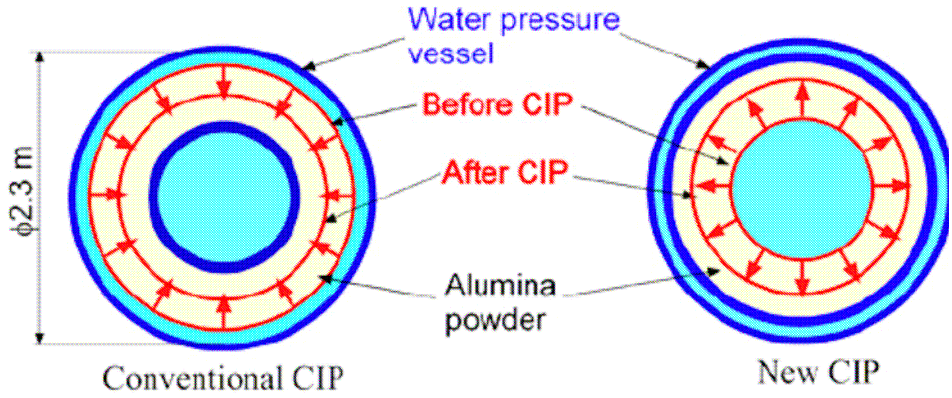

Figure 64 Schematic diagrams of the conventional and the new CIP [63]

Although the realization of large ceramic rings has been achieved, the problems related to the joint between metal plates and insulating materials is still under investigation and tests.

The two metal plates brazed to the alumina cylinder and to the back-up rings are shown in Figure 65.

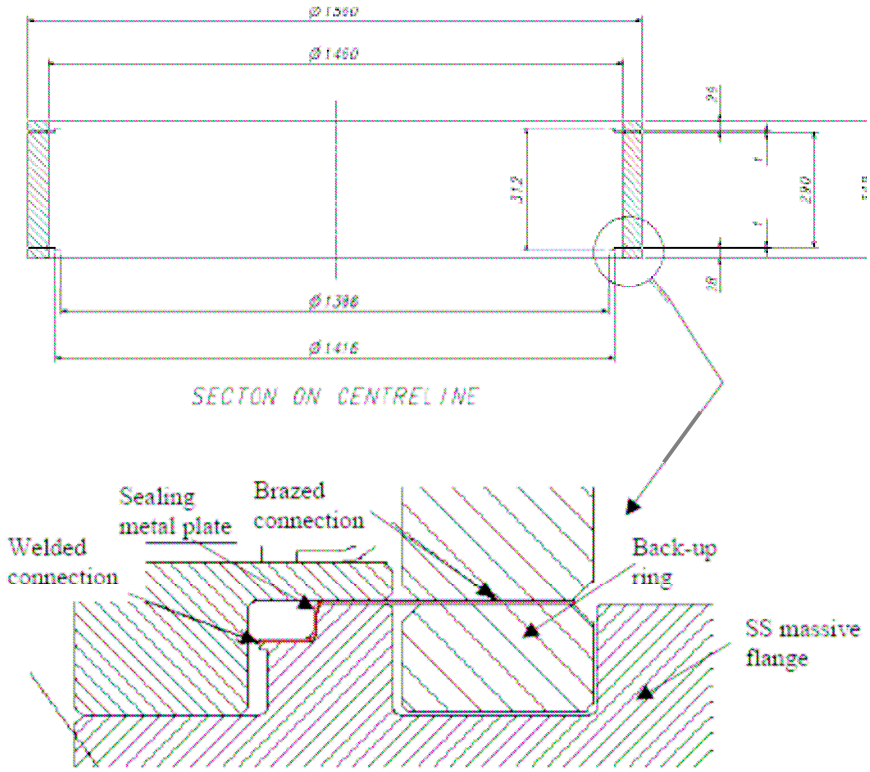

Figure 65 Detailed cross section for the brazed and welded connections of the ceramic insulator ring.

High-temperature vacuum brazing is considered as the neatest and most reliable solution for the metal – ceramic joints, as also experienced by manufacturers of high quality insulated feedthroughs. The brazed metal plates are then joined to the massive stainless steel flanges of the bushing by welding.

Although Titanium alloy metal plates would be a good solution for active brazing to ceramic rings, Kovar® has been preferred for the metal plates since it can be easily welded to SS flanges.

The rings are mainly subjected to the stress field induced by the brazing procedure and the compressive hoop and bending stresses applied during operations, as explained in sec. 2.4. The difference of the thermal expansion coefficients (CTE) between ceramic and metal is the cause of high residual stresses in both materials after brazing. Due to the poor thermal conductivity and the relatively low tensile strength of ceramics, care has to be taken to prevent cracking in the joint and in ceramic.

These are the reasons why the activities have been focused on the metal-ceramic joint by brazing. Applying the criteria and tools developed to carry out the simulation of the brazing procedure explained in 2.3, analyses started from the reference design of Figure 63 and Figure 65.

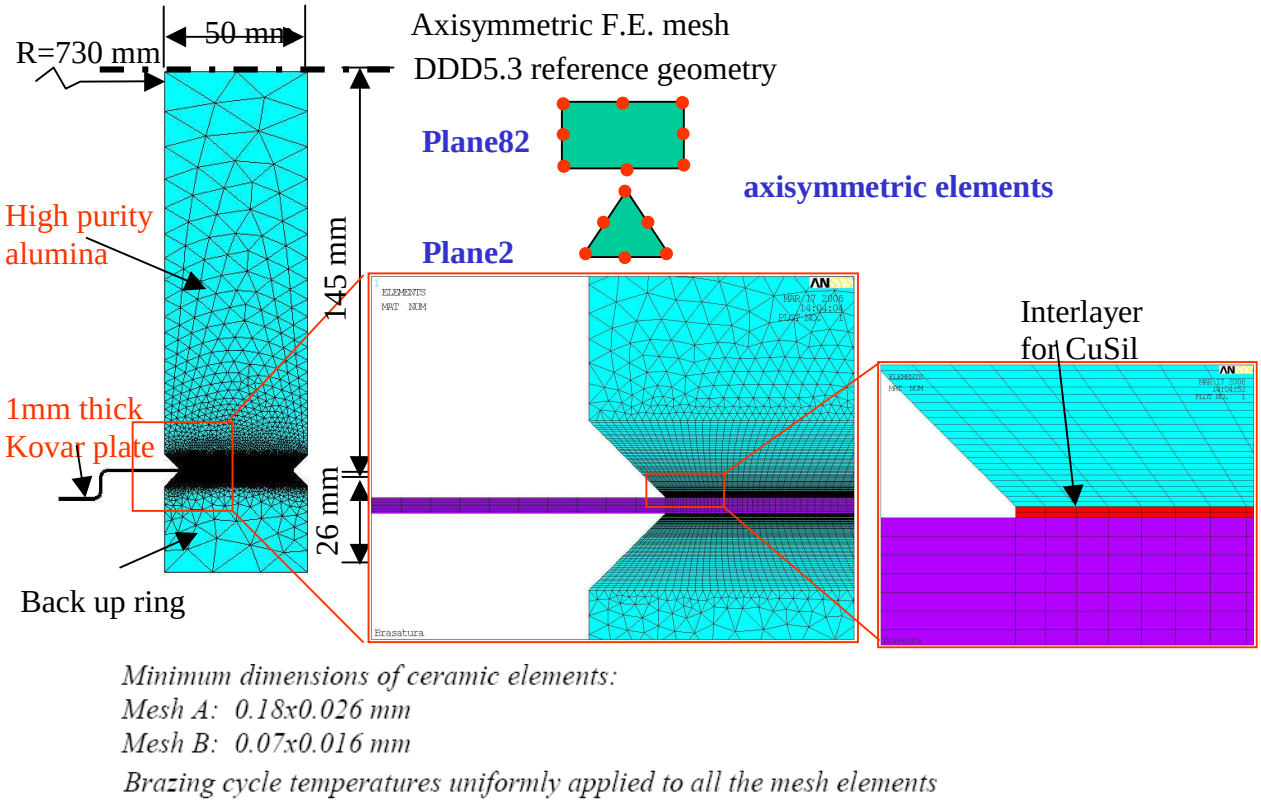

Figure 66 Axisymmetric finite element model for the analyses of ITER reference design insulator ring

The finite element model used to evaluate the failure probability during the brazing process is showed in figure 73.

The thermal expansion coefficients of alumina and kovar are shown in figure 66.

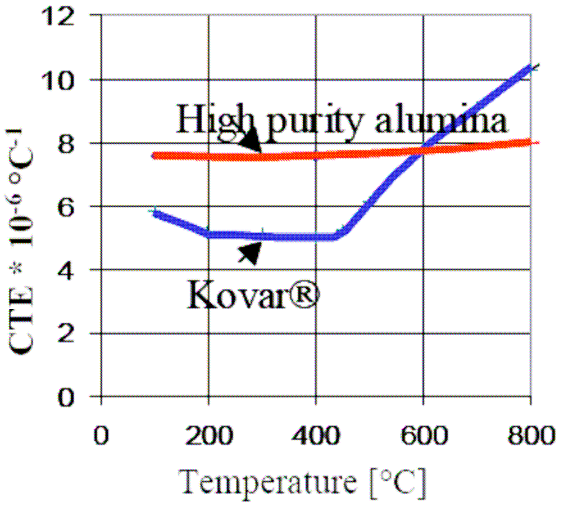

Figure 67 Thermal expansion coefficients of alumina and kovar

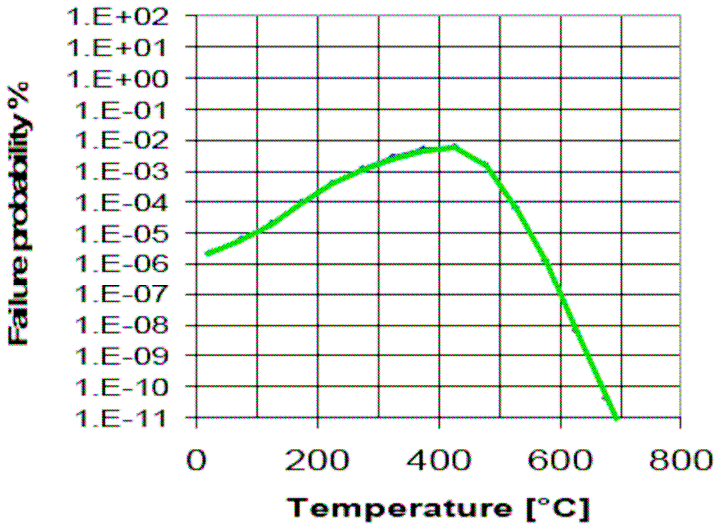

Figure 68 Failure probability during the brazing procedure

The failure probability calculated during the whole cooling phase of the brazing process is shown in figure 75. It is relatively low hence no cracks are expected. Similar analyses carried out considering different geometries (smaller rings) and materials (porcelain and titanium alloy) showed quite high failure probabilities during the cooling phases. Some R&D done in EU during past years demonstrated failures of such small prototypes during the cooling phase of brazing process.
Figure 79 and Figure 70 show respectively the deformation of the kovar plates during brazing and the Von Mises stresses at room temperature after brazing.

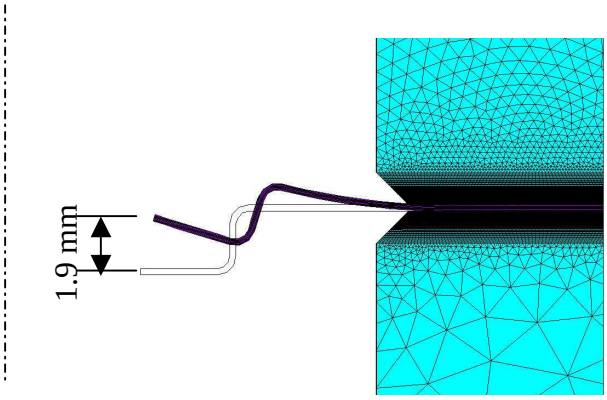

Figure 69 Amplified deformation of the kovar plates during brazing

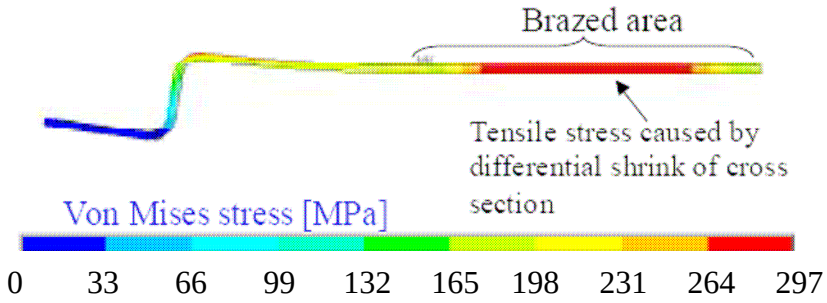

Figure 70 Von Mises stresses in the kovar® plate at the end of the brazing process

3.3 The ceramic post insulator between the accelerating stages

The insulators between each flange (see Figure 71 and Figure 72) are not only electrical components, but they have also a mechanical function; actually they withstand the weight of the whole accelerator and for this reason analyses and design optimisation are necessary.

Aim of the analyses performed as PhD activity was the verification of post insulators (PIs).

An analytic calculation of the maximum load acting on each PI has been first carried out and a FE numerical analysis of a single PI has been then carried out.

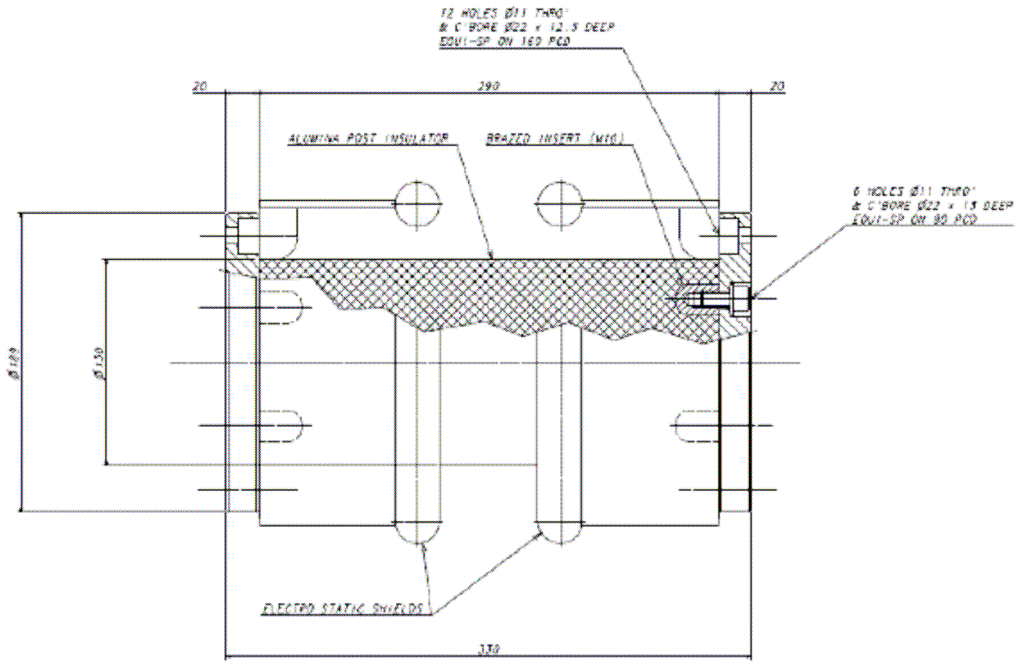

Figure 71 Post insulator reference design

The functionality of the post insulators from a mechanical point of view is shown in Figure 72.

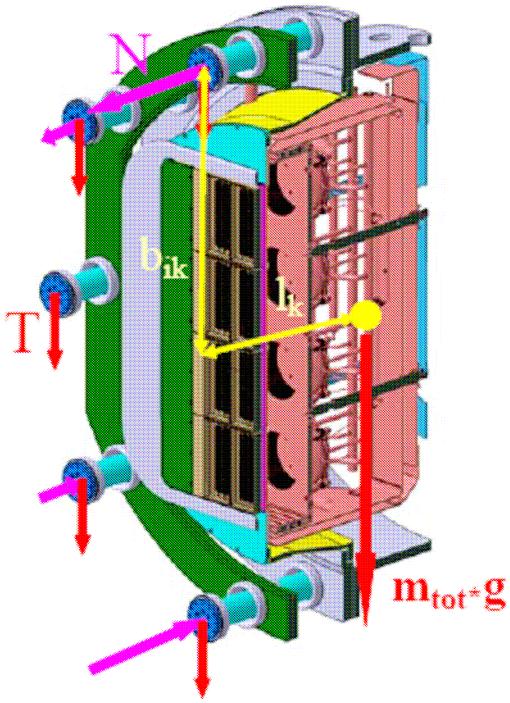

Figure 72 Isometric view of a vertical section of the beam source and accelerator

If each mounting flange is considered as a rigid body, the static equilibrium equations (50) allow estimating the axial N_{ik} and tangential T_{ik} loads acting on each cylindrical insulator. The subscript "k" indicates the stage to which the insulators belong. The subscript "i" indicates the insulator position inside the stage.

$$M_k = m_{tot} \cdot g \cdot l_i$$

$$N_{ik} = \frac{M_k \cdot b_{ik}}{\sum_{i=1}^{K\max} b_{ik}^2} \qquad \textbf{(50)}$$

$$T_{ik} = \frac{m_{tot} \cdot g \cdot l_k}{k_{\max}}$$

m_{tot} is the total mass of the accelerator, l_k is the distance between the plane k of the mounting flange and the gravity centre of the whole source. A safety margin assumption has been taken considering

the gravity centre of the system coincident with the one of the source alone, so the value of l_k has been overestimated. The gravity centre of the source has been assumed in the middle plane of the 1 MV mounting flange (see Figure 72). Mk is the moment due to the weight force evaluated in the plane k, N_{ik} is the axial load acting on the i-th insulator of the k-th plane, as well T_{ik} is the tangential load acting on the i-th insulator of the k-th plane and g is the acceleration of gravity.

The post insulators A and B (see Figure 73) are the most critical because they are placed at the longest distance b_i from the middle horizontal plane and for this reason they are subjected to the highest axial tensile force. While A is placed in a section with the highest value of M_k, B stays in a section which has only 10 insulators.

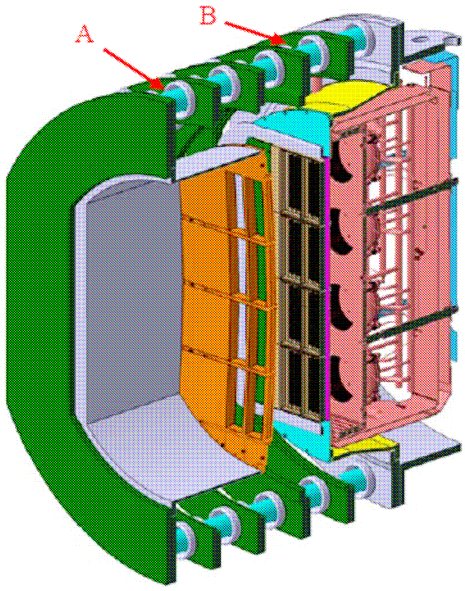

Figure 73 Isometric view of the beam source and accelerator

Insulator	"A"	"B"
Axial Load N [kN]	37.34	24.25
Tangential Load T [kN]	14.17	25.5
L_k[m]	1.8	1.4
B_k [m]	1.329	1.329

Table 3 Main parameters of ITER NBI

The material adopted for PIs is High Purity Alumina ST grade A456 in accordance with the reference design. The material properties assumed to carry out the analysis are σ_0=250 MPa for a volume of 1mm^3 and m=10. While the value of σ_0 can be easily obtained from materials data sheets, the Weibull's modulus m is hardly found in literature. The Weibull's modulus depends both on

material composition and fabrication procedure; the most conservative value for alumina (m=10) has been adopted.

To reduce the computing time, a linear FE analysis has been first carried out.

The load acting on each insulator can be thought as a linear combination of two cases: the first one is the case with only a pure axial load, while the second one is the case with a load orthogonal to the axis; moreover the FE model has been reduced to half the insulator, taking into account the symmetry with proper boundary conditions.

$$\sigma_{ij} = \alpha_1 \cdot \sigma_{ij1} + \alpha_2 \cdot \sigma_{ij2}$$

1° load case
(Symmetric load)

2° load case
(Antimetric load)

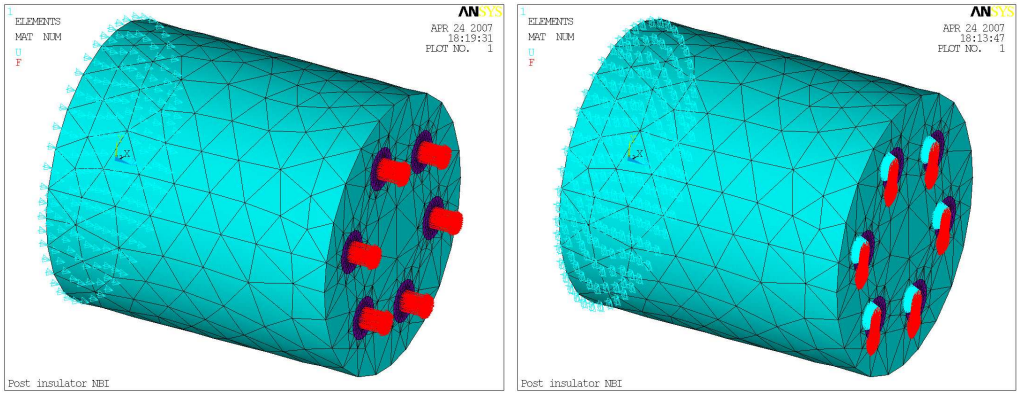

Figure 74 Symmetric and anti-symmetric load cases on PIs

α1 and α2 in Figure 74 are the weights adopted to calculate the applied load. σijk (k=1, 2) in Figure 74 are the stress fields for each load case when the applied loads N and T are equal to 10000 N.

The general results are reported in Figure 75 where the logarithm of failure probability is showed as a function of T and N.

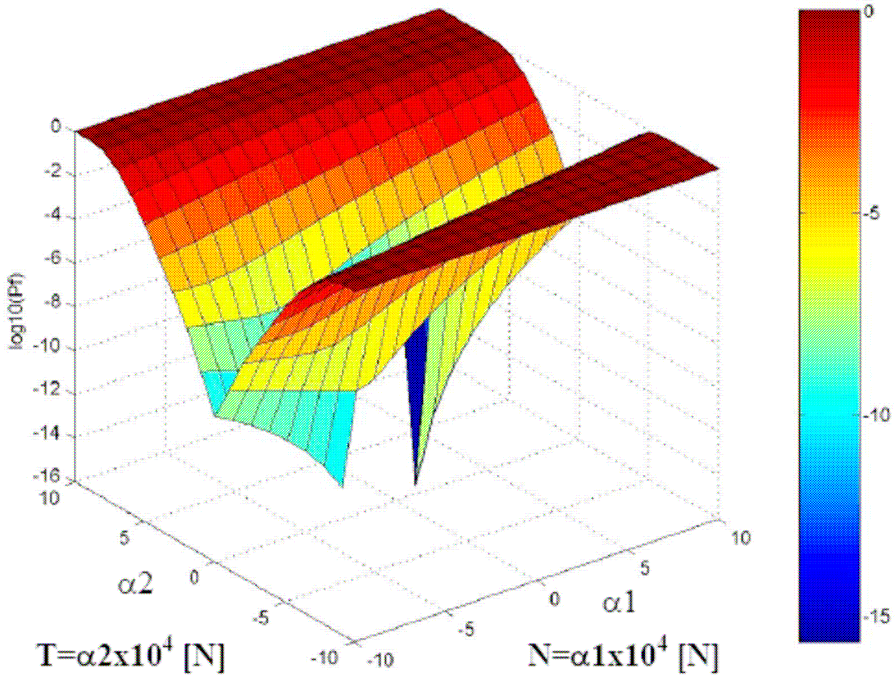

Figure 75 Failure probability vs the weight coefficients α1 and α2

The picture appears symmetric because the failure probability doesn't change if the tangential load is oriented upward rather than downward. Instead the failure probability Pf changes if α1 has positive values rather that negative; in other words $Pf(\alpha1,\alpha2) \neq Pf(-\alpha1,\alpha2)$ because the compression states ($\alpha1 < 0$) are less dangerous than the tensile ones.

The volume integral in eq.(41) required a mesh sensitivity analysis in order to guarantee that the mesh size is sufficiently small for a correct evaluation of the failure probability.

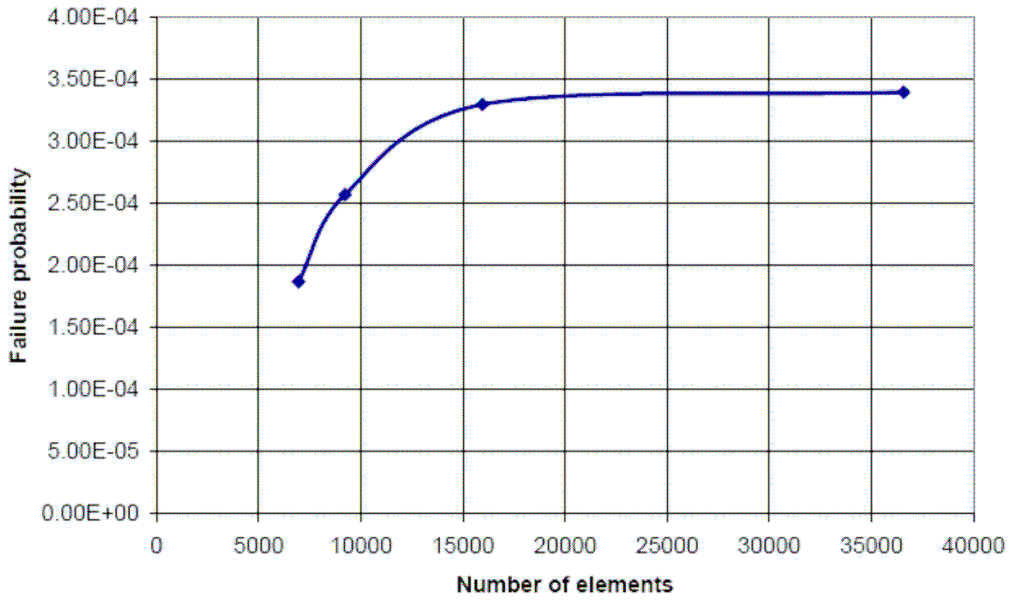

Figure 76 Failure probability vs the mesh size, for insulator "B" (α1=2.42 and α2=2.55)

Figure 76 shows that the failure probability tends to an asymptotic limit, for insulator "B" the limit is 3.4e-04, while for insulator "A" it is 6.4e-6; in both cases the value can be considered acceptable.
The failure probability, as described above, is a function of σ_0, m and the stress field. A good estimate of the failure probability could be carried out knowing a precise value of the Weibull modulus m. Actually this parameter has a big influence on the calculation and the value can be measured by means of tests on a significant number of samples. Nevertheless the adopted value (m=10) appear to be conservative.
It is also important to note that the stresses have been computed considering only the effect of dead weight, neglecting the residual thermal stresses induced by the brazing process. However the most critical state induced by the brazing process should be achieved in the oven during the cooling phase, when the different thermal expansion coefficients between metal inserts and alumina could cause the maximum stresses. The qualification of the brazing procedure and mechanical tests on base material and on insulator prototypes has to be carried out during manufacturing phases. These tests will support design and manufacturing and will confirm results obtained with numerical analyses.

Chapter 4: Charged particle dynamics and beam simulations

4.1 Introduction

In this chapter we discuss the results of the negative beam simulations. The Monte Carlo Code EAMCC [56] presented in chapter 2, has been applied to simulate the Megavolt Test Facility of Naka (MTF) during the experimental campaign to study the SINGAP configuration. EAMCC can simulate several physical phenomena as beam acceleration, the atomic reactions inside the beam and on the surfaces. The code requires the field maps from external codes to calculate the particles trajectories and the electric field maps solving for law of motion coupled with the Poisson's equation. SLACCAD is nowadays a reference code to solve this problem: it evaluates the meniscus and the potential field map in 2D axial symmetric, then the results are the input for EAMCC. Another similar code 2D Beam Orbit is used by the Japanese team to evaluate the space charge effect inside the beam. Recently a new code, Bypo, in which the particles trajectories is solved in a self consistent way with the electric and magnetic field has been developed [65]. All these codes can simulate only one beamlet, so they can not compute the reciprocal interaction, inside a group of beamlet due to the spatial charge. At present a commercial code (Vector Fields Opera) is applied to evaluate the beamlet-beamlet repulsion in a 3D map. In order to assess the results of Opera in a simplified geometry, I have developed a Matlab® tool to evaluate the reciprocal interaction between the negative beamlets: IRES.

4.2 EAMCC applied to the MTF in SINGAP configuration

Within the effort dedicated to investigate the performance of the accelerator in SINGAP configuration for the ITER NBI, two experimental campaigns at the 1MV have been carried out at the MTF in Naka. A device sketch is shown in Figure 77 it has adapted to host a two step accelerating system (SINGAP). A group of 3x5 beamlets have been accelerated from the plasma source toward the grounded grid. The currents at each stage was measured by ammeters, while an inertial and movable calorimeter positioned 2.3 m downward the grounded grid allowed the power deposited by the accelerated particles to be estimated. A suitable system of permanent magnets is mounted 150 mm downward the grounded grid (see Figure 78), to filter the stripped electrons from the negative ion beam. The deflected electrons are directed toward a couple of electron dumps while the negative ions and neutrals are intercepted by the instrumented calorimeter (see Figure 77).

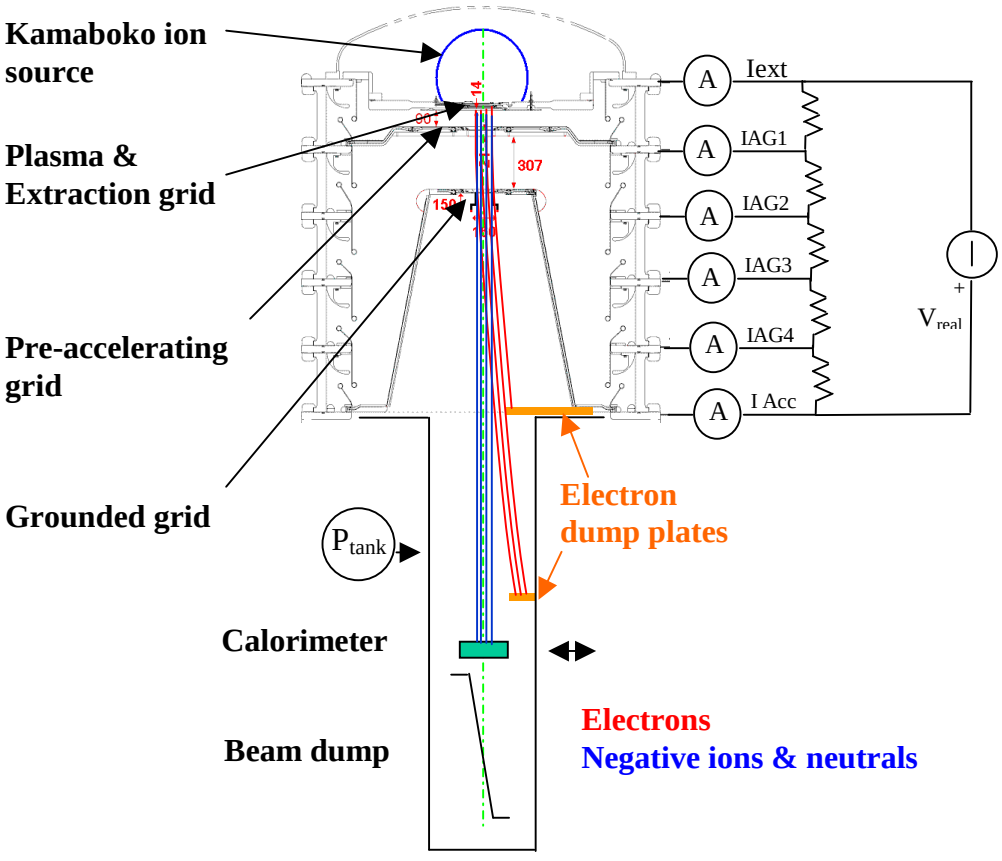

Figure 77 The MTF adapted to the SINGAP configuration. [26]

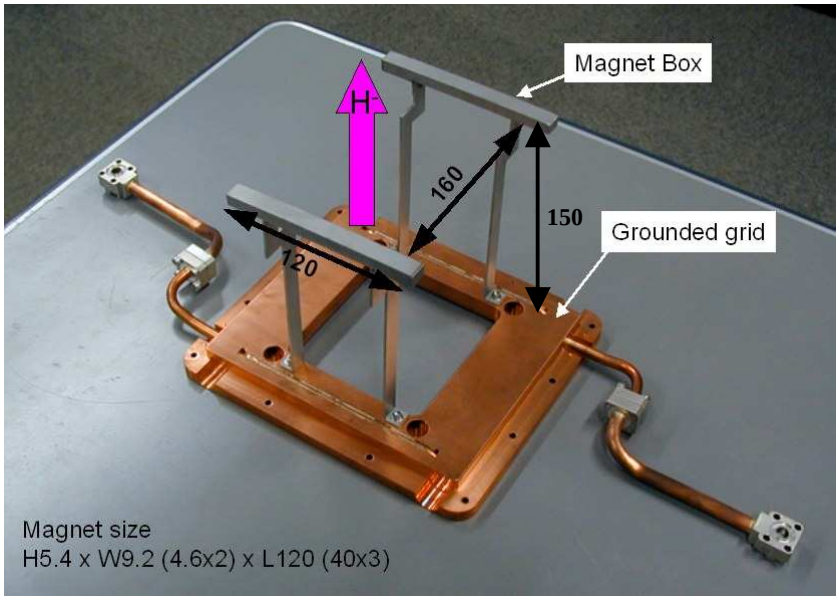

Figure 78 The permanent magnets adopted to deflect the accelerated electrons toward the electron dump plates. [26]

The experimental results have been analysed for 3 shots with similar perveance; the measured data are shown in Table 4 where the voltages, the grid currents, the pressures and the results of the instrumented calorimeter are shown.

Shoth #	Vext (kV)	Iex (mA)	Vreal (kV)	Iacc (mA)	I AG1 (mA)	$I_{thermal}$ (mA)	P_{source} (Pa)	P_{tank} (Pa)
437	2.77	365	700	310	5.9	109.5	0.15	0.087
414	2.8	352	603	280	9.6	113.8	0.15	0.087
390	2.81	322	433	269	-3.9	114.5	0.16	0.082

Table 4: Main measured data for 3 pulses

For all the shots the pulse duration is 0.2 s because the device wasn't actively cooled; this duration is sufficient to study beam physics without introducing the cooling pipes at high voltages. The terms V_{real} is the minimum (negative) voltage supplied by the Crofton-Walton generator (see Figure 77): the voltages at each grid are fixed and equally spaced by a resistive divider.

The current collected by each grid is measured by ammeters; only the Extraction Grid current is calculated by the other grids information by imposing total charge conservation. In the SINGAP

case the currents collected at the intermediate stages (IAG2, IAG3 IAG4) are negligible because the grids are not present (see Figure 77).

The data obtained by the instrumented calorimeter are used to define I_{th} (thermal current) which is the ratio between the beam power, measured by thermocouples, and Vreal; both charged and neutral particles contribute to form the thermal current; to separate the two contributions the information coming from the stripping profile is necessary to calculate the negative ion current. The pressure is measured in the tank in one point (see Figure 77), while the pressure in the source, P_{source} can be calculated by the conductance equation.

A comparison between experimental and numerical results has been carried out implementing the geometry of SINGAP in EAMCC V2.84; this version of the code simulates two beamlets among the group of 3x5 beamlet that are really present in the device; couples of periodicity conditions are applied on each rectangle side as shown in the left sketch of

Figure 79: a particle that exits on the upper side will be re injected with the same velocity on the bottom. This process is repeated for a number of times equal to the number of apertures in such direction. Of course in this way the outer holes are not well simulated.

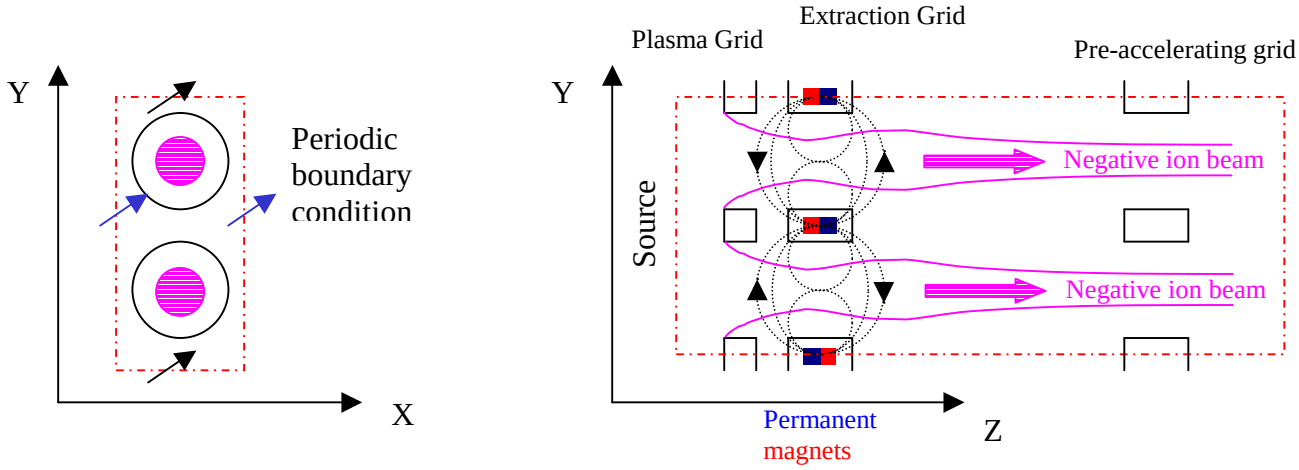

Figure 79 EAMCC simulation domain (orthogonal projections, front and lateral view, z axis directed along the beam)

The present analysis has been carried out considering a limited domain inside the accelerating gaps. The main results obtained by EAMCC concern the computation of particles trajectories together with the beam power load deposited on each grid. A full beam simulation, carried out by EAMCC, is composed by two independent simulations: the first one calculates the trajectories of negative ions extracted from the plasma grid, while the second one calculates the trajectories of the co-extracted electrons. Figure 80 summarizes both simulations, it is worth noticing how the permanent magnets embedded in the extraction grid are very efficient to trap the co extracted electrons in the first gap between plasma and extraction grid.

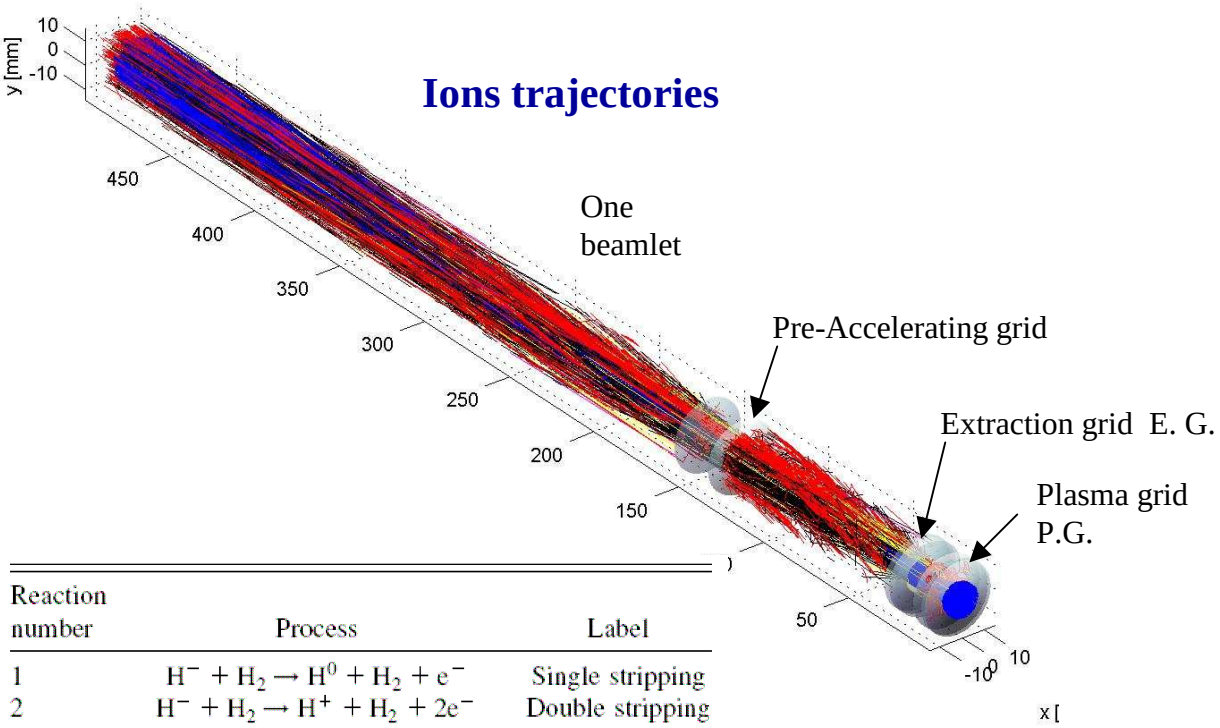

Reaction number	Process	Label
1	$H^- + H_2 \rightarrow H^0 + H_2 + e^-$	Single stripping
2	$H^- + H_2 \rightarrow H^+ + H_2 + 2e^-$	Double stripping
3	$H^- + H_2 \rightarrow H^- + H_2^+ + e^-$	Ionization
4	$H^0 + H_2 \rightarrow H^0 + H_2^+ + e^-$	Ionization

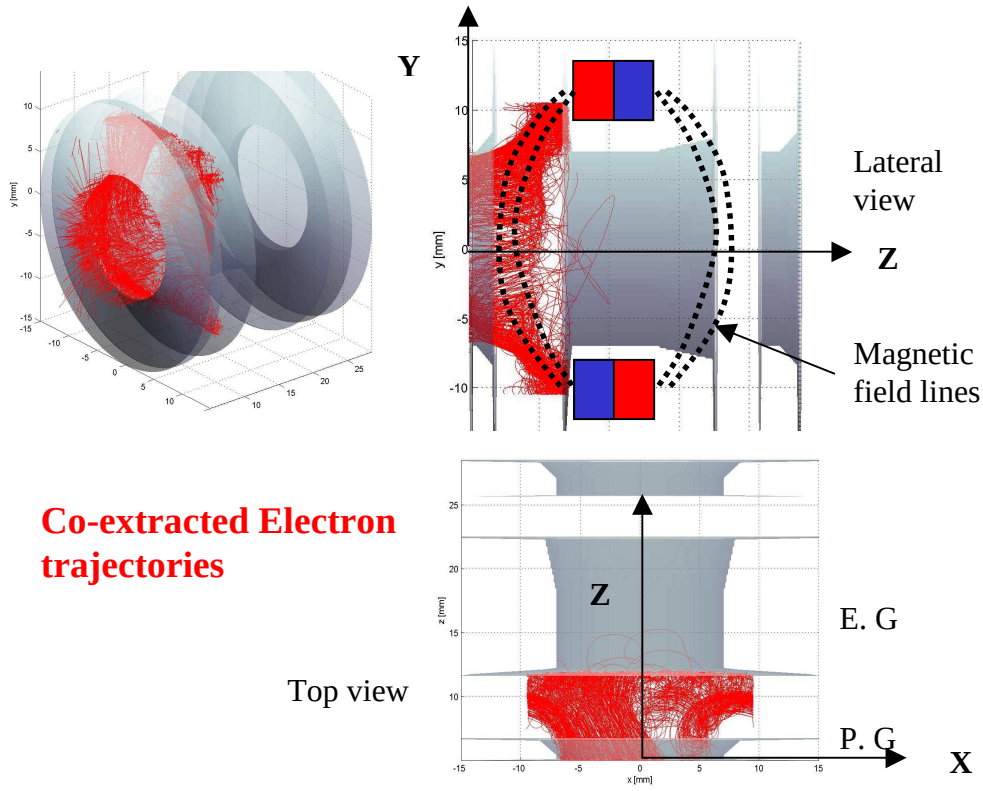

Figure 80 The particles trajectories computed by EAMCC

The red co-extracted electron trajectories, showed in Figure 80, orbit around the magnetic field lines produced by the permanent magnets embedded in the extraction grid thus they are trapped by the magnetic field lines and then they are drained by the Extraction Grid (EG) which is polarized positively respect to the plasma (grid previous grid).

Figure 81 shows the reconstruction of the heat flux for the whole group of beamlets at the accelerator exit (about 500 mm downward the plasma grid); the information obtained from the couple of beamlets has been replicated in space in order to obtain the heat flux map for the whole 5x3 array of accelerated beamlets . It is possible to appreciate from Figure 80 and Figure 81 , how the EG permanent magnets interacts not only with the co-extracted electrons but they also deflect the negative ion beamlets in horizontal direction; the white rectangle of Figure 81 represents the front view of the integration domain (see Figure 79) both peaks of heat flux are displaced from their nominal position, because the magnetic field, which acts mainly in vertical direction, has opposite orientation passing from the first beamlet to the second one.

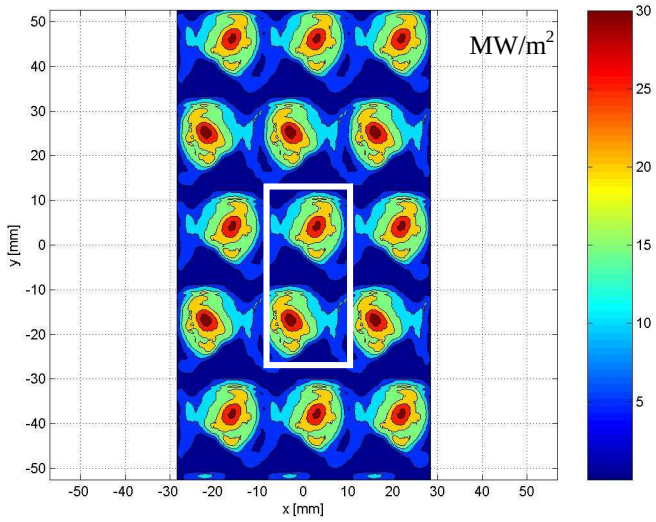

Figure 81 The beam heat flux reconstructed at the accelerator exit

It is important to note that both grid voltages and extracted current density are input parameters in the numerical simulations. While the grid voltages are treated as independent variables (and for this reason it is an input quantity), the current shouldn't be a free choice for the numeric simulations: following this, the way to calculate the current density should foresee a coupling between the physic inside the source with the one that controls the negative ion extraction. As mentioned in chapter 2, this kind of simulation is quite prohibitive because the power distributed inside the source, the formation and the transport phenomena for each species, the pre-sheath upward the meniscus have different length scales, so nowadays the physics simulations are mainly carried out separately . The

whole EAMCC package hence requires not only the grid voltages but also the extracted current; if we want to benchmark the code with the experimental results, it is necessary to obtain the current density information from the experiment. In this case, the extracted current has been reconstructed from the calorimetric measurements and by estimating the stripping profile.

Figure 82 shows the procedure adopted to carry out the comparison between the experimental and numerical results. The red boxes represent the information coming from the experiment, the blue box gives the cross section data for the beam reactions, the magenta box shows the assumption of the ratio between the ion and electron current density extracted from plasma. The green boxes represent the main steps carried out in the simulation from the numerical point of view.

The yellow ellipses represent the comparisons between information coming from different points, while the 1^{st} and 2^{nd} benchmarks are between intermediate steps of the numeric simulation, the 3^{rd} one has a particular relevance because it compares the currents collected at each potential, and measured by ammeters, with the ones obtained by EAMCC.

The analyses have been carried out considering 3 shots whose experimental results are reported in Table 4, although the voltages and the extracted currents are different, the conclusions are similar for all the cases.

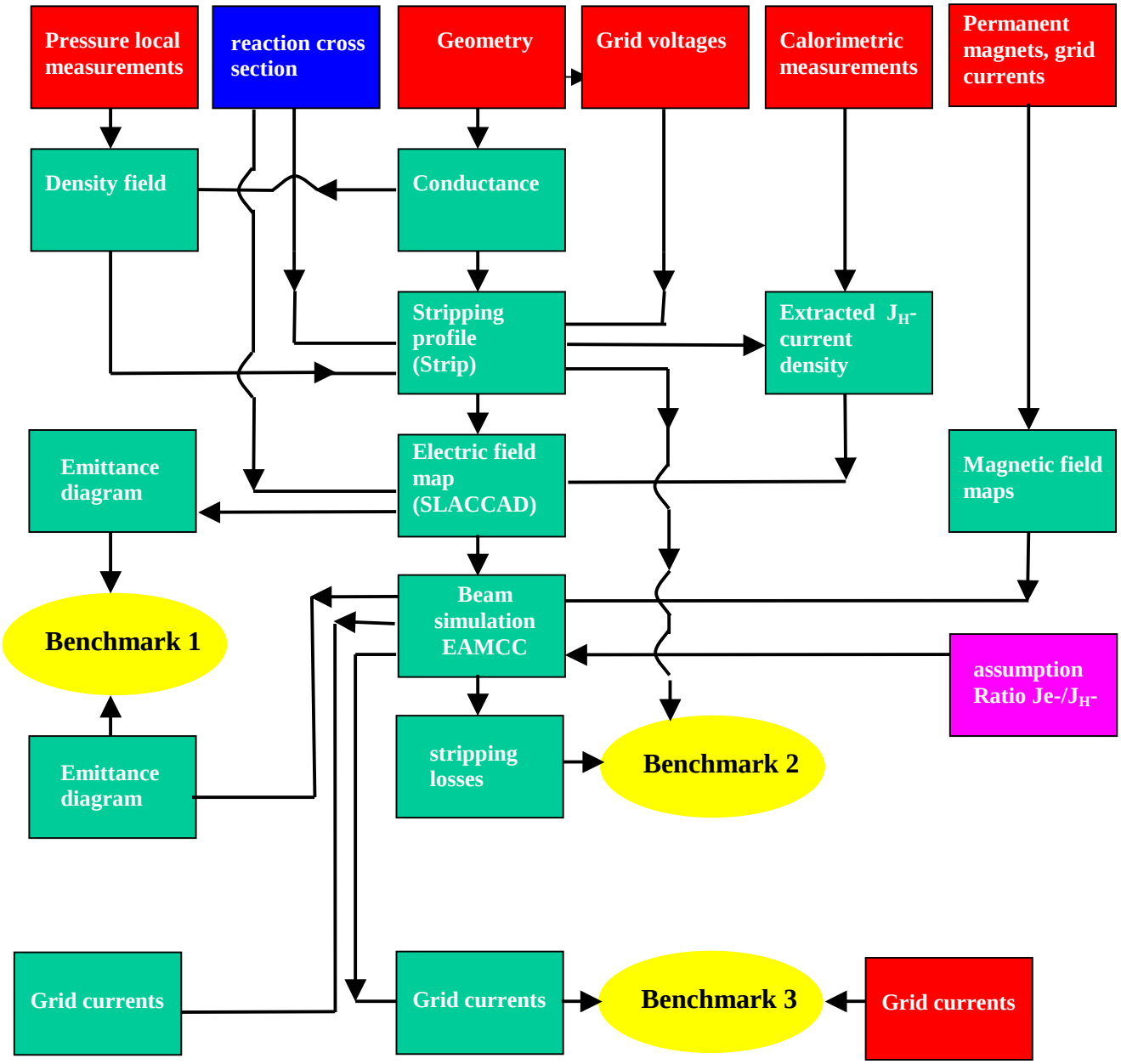

Figure 82 Flow chart followed to validate the numerical results of EAMCC by the data obtained on the MTF with the SINGAP configuration

The 1st benchmark compares the emittance diagram (introduced in chapter2) obtained by SLACCAD (the 2d axi-symmetric Poisson's equation solver) and by EAMCC, Figure 83 shows the two diagrams: although EAMCC can also simulate the initial beam temperature by a spread of initial velocity that will increase the beam emittance, (actually the blue cloud of data has a bigger dispersion) the two diagrams are similar, so the electric field maps imported into EAMCC (and

produced by SLACCAD) can be considered self consistent with the trajectories integrated by EAMCC. The double solution in terms of velocities for the left side of the second diagrams depends on the periodicity conditions that are not included in SLAC.

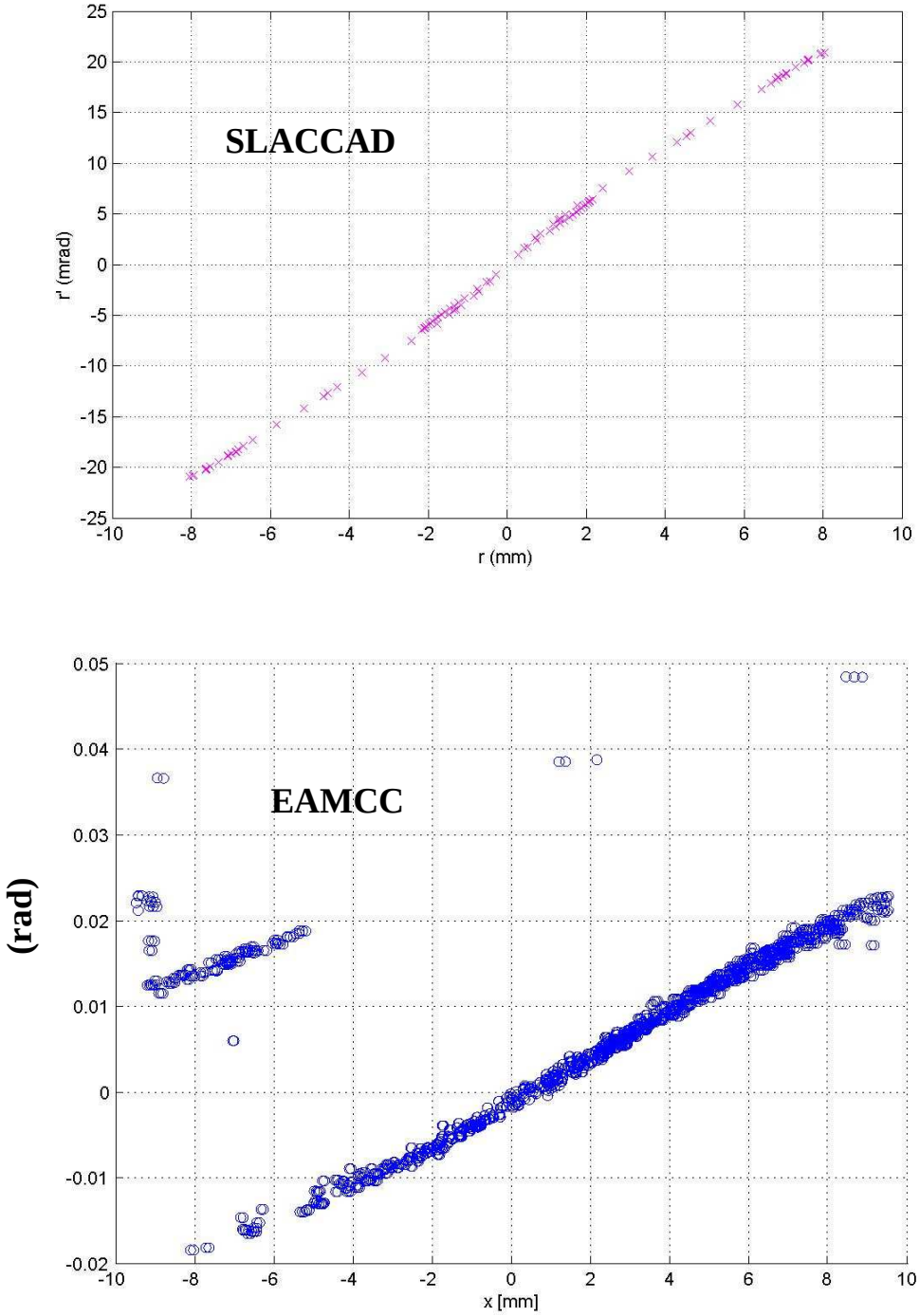

Figure 83 The emittance diagram evaluated by SLAC and by EAMCC (1st comparison) . (The results show a bad optic case with a divergent beam)

As far as the 2nd comparison is concerned, table 4 summarizes the last value of the stripping profile obtained by EAMCC and by the program Strip.exe [54], the code estimates the reduction of negative ions current along the beam integrating by a one-dimensional approach the equation $\frac{dn}{n} = N \cdot \sigma \cdot dx$ described in chapter 2 (see Figure 32). It is worth noticing that, the information concerning the stripping profile evaluated by strip, are an input parameter for SLACCAD (see. Figure 82) such information should be consistent with the results obtained by EAMCC.

Shot	EAMCC	Strip
# 437	67%	68%
# 414	62.5 %	63%
# 390	57.3 %	63%

Table 5 Comparison between the last value of the stripping profile (IH-out/IH-extracted) evaluated both EAMCC and Strip as well

The table shows the results are comparable. On the contrary, the last and more important cross check shows that a discrepancy exists.

Figure 83 is a sketch summarizing the results for shot #414 in terms of currents collected by each grid: both electron (red) and negative ion (blue) currents, obtained by EAMCC, are shown; black currents indicated in figure are the linear combination of the two simulation (red and blue ones). The ratio between the electron and negative ions extracted currents has been assumed by the user. In this case the ratio has been chosen equal to unity; this means that for each negative ion one electron is extracted [4].

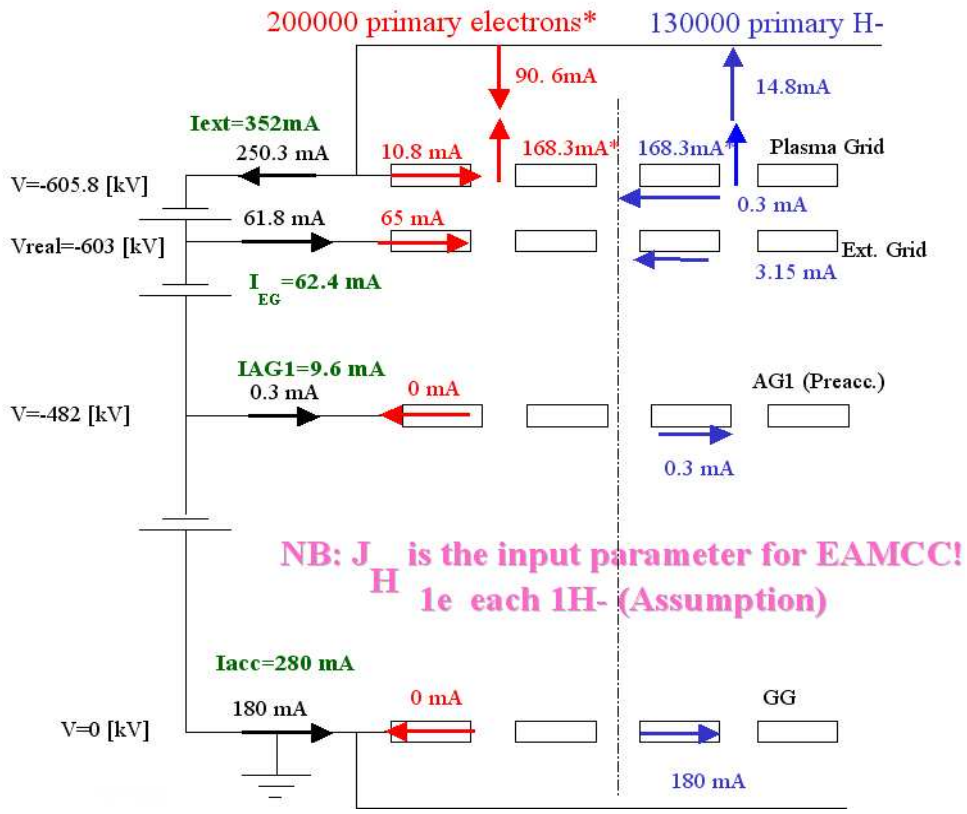

Figure 84 The current collected by each grid (shot #414) , (3rd comparison)

The currents measured by ammeters are shown in green. It can be noted that a difference of 100 mA exists between experimental data and numeric results; this difference is present more or less also for the other shots. The presence of positive ions downward the grounded grid and their acceleration toward the plasma source could justify this mismatch; while the negative ions are directed toward the grounded grid, a considerable amount of positive ions (formed by the ionization of background gas due to the negative ion beam) travel downstream the accelerator. It is important to notice that although EAMCC considers the background gas ionization (for this reason it could follow the positive ions trajectory), the limited domain adopted in the simulation isn't sufficient to correctly simulate this aspect: the domain length in the simulation is about 0.5 m, while the distance between plasma grid and calorimeter is about 2.8 m. Further analysis should be carried out in order to assess this hypothesis: an analytical model could be developed to estimate the positive ion density downward the grounded grid and the classic sheath theory could be used to estimate the positive ions flux toward the source, in this manner the difference between the numeric and measured results (showed in Figure 84 respectively in black and green) could be justified.

4.3 The code IRES

The beamlet-beamlet interaction is a process which has an important impact on the design of the grids for a multi-aperture electrostatic accelerator.
The charge effect leads to beamlet deflection, then increasing the divergence of the whole beamlet group. According to the beamlet deflection, the grid apertures should be properly aligned in order to provide the correct aiming of the beamlets and to avoid excessive thermal load on the grids.
Although Vector Field Opera (VFO) is the commercial code written to solve this problem [30], this code appears time consuming. A preliminary evaluation of the beamlet-beamlet interaction could be a useful way to focus the attention on important details concerning the beam optic, than further information, if necessary, could be obtained by VFO which can solve the Poisson's equation for the whole 3D problem considering more detailed geometry.
A new tool called IRES (Ions Relativistic Equation Solver) has been developed in Matlab® to simulate the 3D trajectories of a whole group of beamlets by integrating the relativistic equation of motion.

4.3.1 Code description

From the operational point of view, the IRES code starts from a three-dimensional map (at iteration 0) of magnetic and electric fields calculated by other software packages (e.g. ANSYS® or Comsol Multiphysics®) or, in case of simple configurations, it can be defined by the user; than the code computes for the particle trajectories.
The equation of motion (written in the laboratory reference system) has been solved taking into account the relativistic effect eq. (51) , where γ is the relativistic factor $\gamma = \left(1 - \frac{v^2}{c^2}\right)^{-\frac{1}{2}} = \left(1 - \frac{v_x^2 + v_y^2 + v_z^2}{c^2}\right)^{-\frac{1}{2}}$, c is the speed of light.

$$\overline{F} = \frac{d}{dt}\left(\gamma \cdot m \cdot \overline{v}\right) = \gamma \cdot m \cdot \frac{d\overline{v}}{dt} + \frac{d\gamma}{dt} \cdot m \cdot \overline{v} \qquad \textbf{(51)}$$

Second addend of eq. (51) has been developed considering eq. (52) which leads the time derivative of γ.

$$\frac{d\gamma}{dt} = \frac{\partial\gamma}{\partial v_x} \cdot \frac{dv_x}{dt} + \frac{\partial\gamma}{\partial v_y} \cdot \frac{dv_y}{dt} + \frac{\partial\gamma}{\partial v_z} \cdot \frac{dv_z}{dt} = \frac{\gamma^3}{c^2} \cdot \left(v_x \cdot \frac{dv_x}{dt} + v_y \cdot \frac{dv_y}{dt} + v_z \cdot \frac{dv_z}{dt}\right) \qquad \textbf{(52)}$$

Thus the eq. (51) has been rewritten expanding in vector components:

$$\frac{d}{dt}\left(\gamma \cdot m \cdot \bar{v}\right) = m \cdot \gamma \cdot \begin{bmatrix} 1 & 0 & 0 \\ 0 & 1 & 0 \\ 0 & 0 & 1 \end{bmatrix} \cdot \begin{Bmatrix} \dot{v}_x \\ \dot{v}_y \\ \dot{v}_z \end{Bmatrix} + \frac{m \cdot \gamma^3}{c^2} \cdot \begin{bmatrix} v_x^2 & v_x \cdot v_y & v_x \cdot v_z \\ v_y \cdot v_x & v_y^2 & v_y \cdot v_z \\ v_z \cdot v_x & v_z \cdot v_y & v_z^2 \end{bmatrix} \cdot \begin{Bmatrix} \dot{v}_x \\ \dot{v}_y \\ \dot{v}_z \end{Bmatrix} = [M] \cdot \begin{Bmatrix} \dot{v}_x \\ \dot{v}_y \\ \dot{v}_z \end{Bmatrix} = \overline{F} \qquad \textbf{(53)}$$

where F represents the electric and magnetic force that acts on the charged particles, eq. (54).

$$\overline{F} = q \cdot \begin{Bmatrix} E_x + v_y \cdot B_z - B_y \cdot v_z \\ E_y + v_x \cdot B_z - B_x \cdot v_z \\ E_z + v_x \cdot B_y - B_x \cdot v_y \end{Bmatrix} \qquad \textbf{(54)}$$

By inverting the matrix M of eq. (53), it is possible to solve in term of acceleration, as in eq. (55).

$$\begin{Bmatrix} \dot{v}_x \\ \dot{v}_y \\ \dot{v}_z \end{Bmatrix} = \left[M^{-1}\right] \cdot \overline{F} \qquad \textbf{(55)}$$

where M^{-1} is:

$$M^{-1} = \begin{bmatrix} \dfrac{c^2 + \gamma^2 \cdot \left(v_z^2 + v_y^2\right)}{m \cdot \gamma \cdot \beta} & -\dfrac{\gamma \cdot v_x \cdot v_y}{m \cdot \beta} & -\dfrac{\gamma \cdot v_x \cdot v_z}{m \cdot \beta} \\ -\dfrac{\gamma \cdot v_{x\cdot} \cdot v_y}{m \cdot \beta} & \dfrac{c^2 + \gamma^2 \cdot \left(v_z^2 + v_x^2\right)}{m \cdot \gamma \cdot \beta} & -\dfrac{\gamma \cdot v_y \cdot v_z}{m \cdot \beta} \\ -\dfrac{\gamma \cdot v_z \cdot v_x}{m\beta} & -\dfrac{\gamma \cdot v_y \cdot v_z}{m \cdot \beta} & \dfrac{c^2 + \gamma^2 \cdot \left(v_y^2 + v_x^2\right)}{m \cdot \gamma \cdot \beta} \end{bmatrix} \qquad \textbf{(56)}$$

$$\beta = c^2 + \gamma^2 \cdot \left(v_x^2 + v_y^2 + v_z^2\right)$$

Therefore the equation of motion has been integrated adopting the Matlab® ODE (Ordinary Differential Equation solver) functions rewriting the three equations of motion (51) in a first order system of six equations.

Then the code updates the field map by taking into account the effect of the spatial charge; the fields are updated in equally-spaced nodes in a 3D grid. During the trajectories integration, the electric and magnetic fields are obtained by an interpolation between the data stored in the grid nodes. The process is repeated up to final convergence which is monitored by the displacements of

the last particle positions step by step, the code converges when no appreciable difference between two successive steps appears (lower 3-4%) giving , in this way, the self-consistent solutions of field maps and trajectories of each beamlet centre.

4.3.2 The analytic model to validate the code

The code has been validated by comparing the results with those obtained for a simple configuration, where the analytical approach has been used to estimate the beamlet-beamlet interaction. The simplified approach used to carry out the simulation by IRES has been suggested considering the conclusion of the Gauss's theorem about the electric field produced by symmetric spatial charge distribution (e.g spherical and cylindrical) : the field, in the charge-free space, doesn't depend on the charge concentration . If we consider an array of accelerated beamlets, in the general case, there are no particular symmetry conditions that can be utilized, but if we assume a system of accelerated beams in paraxial approximation, the variation of the transverse dimension is not so significant, so we can imagine the beamlet composed by a series of charged disks (or rectangles in 2D approximation) elements placed along the beam direction (see Figure 85 a), each rectangular element has a thickness dz and a height D(z) that slowly changes along z. To approximate the beamlet with a line, each rectangle should be replaced by a charged point (lumped approach, see Figure 85 b)

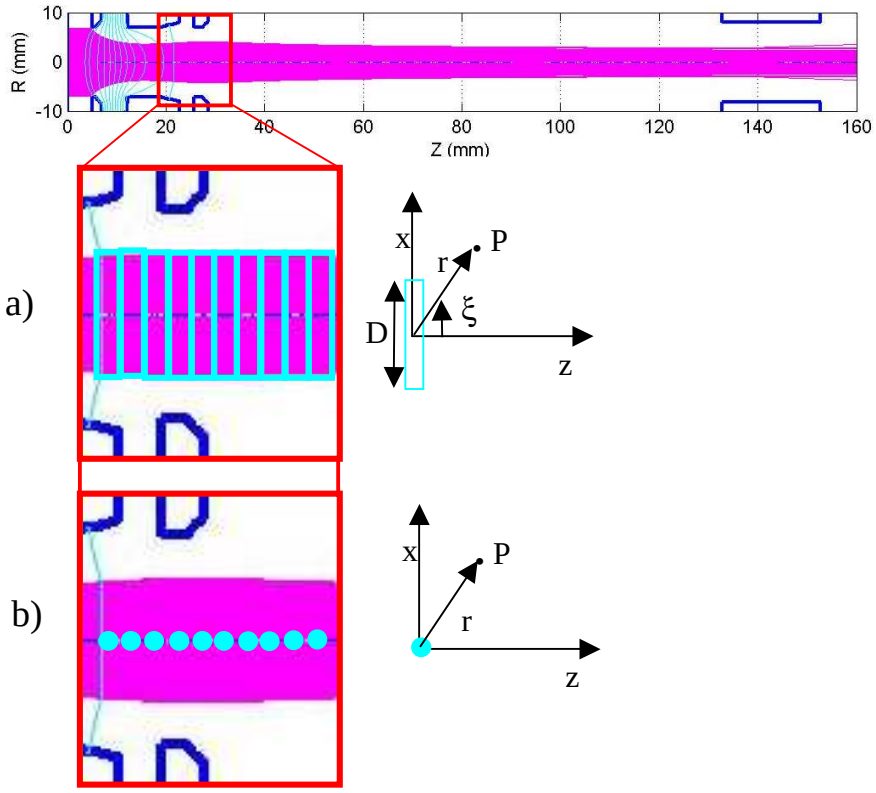

Figure 85 Two possible models of charge elements inside the beamlet: distributed and lumped approach

As usual the lumped approach scheme introduces errors; to estimate it, we can compare the potential map produced by each element in both cases, the analytic calculation has been carried out considering the 2D planar symmetry for the case a, in this manner an analytic expression for the electrostatic potential has been delivered. In both case the potential can be obtained by the elementary eq. (57) where r is the distance between the elementary charge dq and the point P in the space (see Figure 85) where we want to evaluate the potential V, $r = \sqrt{x_p^2 + z_p^2}$

$$dV = \frac{dq}{4 \cdot \pi \cdot \varepsilon_0 \cdot r} \tag{57}$$

In case a) if λ is the linear charge density along D and if we assume that λ is constant for each rectangular element shown in Figure 85, we have eq. (58):

$$dV = \frac{\lambda \cdot d\xi}{4 \cdot \pi \cdot \varepsilon_0 \cdot \sqrt{(x_P - \xi)^2 + z_P^2}} \tag{58}$$

The integration of eq. (58) between –D/2 and +D/2 along ξ leads to eq. (59)

$$V = \frac{\lambda}{4 \cdot \pi \cdot \varepsilon_0} \log\left[\frac{D - 2 \cdot z_p + \sqrt{\left(D - 2 \cdot x_p\right)^2 + 4 \cdot z_p^2}}{D + 2 \cdot z_p - \sqrt{\left(D + 2 \cdot x_p\right)^2 + 4 \cdot z_p^2}} \right] \tag{59}$$

This equation represents the contribution to the potential due to a single rectangular element whose charge is λ D=q . On the other hand the potential map for the lumped approach is simply expressed by eq. (60)

$$V_{lumped} = \frac{\lambda \cdot D}{4 \cdot \pi \cdot \varepsilon_0 \sqrt{x_p^2 + z_p^2}} \tag{60}$$

The contour plot of the relative error $\varepsilon = \frac{V_{lumped} - V}{V}$ is shown in Figure 86 where both axes have been normalized to D.

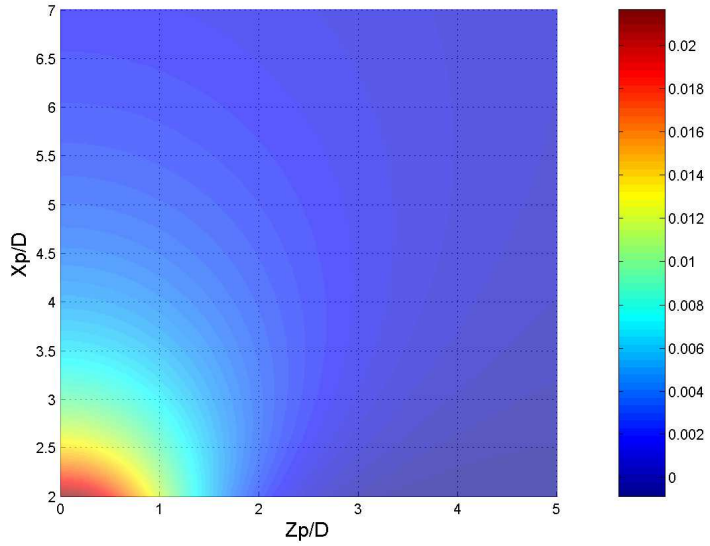

Figure 86 Relative error ε on the potential Map

In the case of the ITER NBI in SINGAP configuration, the distance between holes is approximately 20 mm both in the y and in the x directions, while the beam diameter is about 10 mm [21] in the pre-accelerating grid; this means that xp/D is greater that 2 and the error, for only one element, is lower that 2% (see Figure 86). As, the evaluation of the electric fields, concerns the relative errors on the transversal component Ex, which causes the beams divergence, it is some percent at the most, see Figure 87.

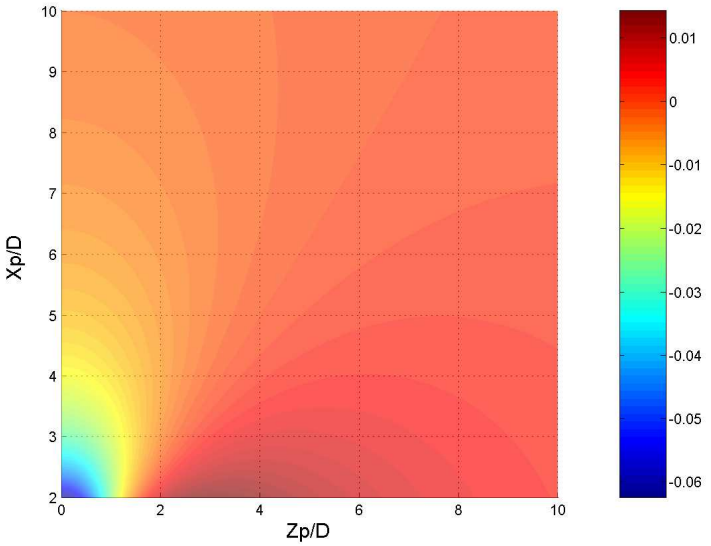

Figure 87 Relative error on the field component Ex

A more precise evaluation could be mad by integrating all the contributions of all the rectangular elements; the charge q=λ D on each rectangular element becomes function of z according with the spatial charge obtained by the Poisson's equation. A simplified approach can be carried out analytically considering the relationship $dq = \frac{dz \cdot I}{v}$ where I is the current of the beamlet and v is the particle velocity, the latter is related to the electrostatic potential by the energy equation $v = \sqrt{v_0^2 + \frac{q}{2 \cdot m} \cdot (U_0 - U)}$ (the ions are not relativistic so the motion equation can be written in the classic way) while the potential U distribution along the beam follows the solution of the Child-Langmuir's formula (which is the one dimensional solution of Poisson's coupled with the conservation of the total energy equation) ; of course the beamlet squeezing is not considered by this mono-dimensional approach, thus the beam dimension D became constant with z.

The effect of the magnetic field self produced by the beam currents is negligible for ions; on the other hand this field should be considered when the particles velocities are relativistic. A demonstration of this aspect could be developed considering the two indefinite parallel beamlets of Figure 88, both beamlets are schematised as indefinite wires crossed by a current I and placed at a relative distance d. The current on each beamlet depends on the motion of charge particles q, the particles have constant and parallel velocity v_{par} flowing in the same direction.

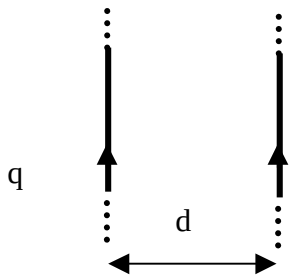

Figure 88 Two indefinite charged beams

A couple of external reactions are necessary to keep the beam parallel otherwise the charge particles can not travel along straight lines.

The effect of magnetic field is to attract the wires, it can be calculated by the Ampere's law in the laboratory reference system, see eq. (61).

$$B = \frac{I \cdot \mu_0}{2 \cdot \pi \cdot d} \tag{61}$$

The electric field can be evaluated by the Gauss's theorem considering that the spatial charge $\lambda = I / v_{par}$ [C/m] .

$$E = \frac{I}{2 \cdot \pi \cdot \varepsilon_0 \cdot d \cdot v_{par}} \tag{62}$$

Combining eq. (61) and eq. (62) and remembering the relationship between the speed of light, the dielectric permittivity ε0 and magnetic permeability μ0 $c^{-2} = \mu_0 \cdot \varepsilon_0$; the total force can be express by eq. (63) which proofs that the electric field action is always greater than the magnetic field one as $v_{par} < c$.

$$F = q \cdot \left(E - v_{par} \cdot B\right) = q \cdot \frac{I}{2 \cdot \pi \cdot \varepsilon_0 \cdot d \cdot v_{par}} \cdot \left(1 - \frac{v_{par}^2}{c^2}\right) \tag{63}$$

In case of D^- ions, accelerated up to 1MV, $\left(v_{par} / c\right)^2 << 1$ in this case the second addend of eq. (63) (due to magnetic field) became negligible and the force can be computed considering only the electric filed effect, moreover when $\left(v_{par} / c\right)^2 << 1$ the Newton's equation of motion can be used.

As concern the validation procedure to integrate the beamlet trajectories, the same simple case has been analysed.

If we cancel the external reactions (that keep the beams parallel) for a distance S along the wires direction, the beamlets will diverge as shown in Figure 89.

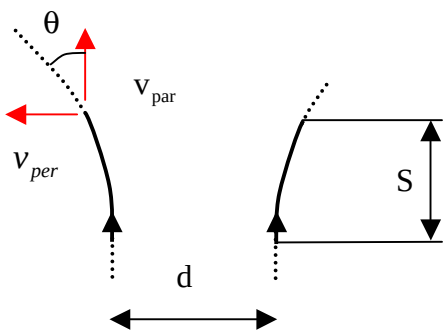

Figure 89 Two indefinite beam, lateral view

The parallel velocity v_{par} will not change so much, instead the perpendicular velocity will change from 0 to v_{per}. The time to cover the distance S is $\Delta t = S/v_{par}$, in the same time, the particle will be pushed outward by the electric field produced by the other particles, as first approximation (if $v_{per}/v_{par} << 1$) we can calculate the electric field acting on the charge particles by eq. (62). On the other hand, the velocity v_{per} can be computed integrating $F = q \cdot E = m \cdot a_{per}$, from 0 to Δt so it is possible to obtain the eq. (64) and (65)

$$v_{per} = \frac{q \cdot E}{m} \cdot \Delta t = \frac{q \cdot I \cdot S}{2 \cdot \pi \cdot v_{par}^2 \cdot \varepsilon_0 \cdot d \cdot m} \quad \textbf{(64)}$$

$$\frac{v_{per}}{v_{par}} = \frac{q \cdot I \cdot S}{2 \cdot \pi \cdot v_{par}^3 \cdot \varepsilon_0 \cdot d \cdot m} = \tan(\theta) \quad \textbf{(65)}$$

If the particles had been preventively accelerated from 0 to v_{par} by an electrostatic accelerator with a difference of potential U, we would have $\frac{1}{2} \cdot m \cdot v_{par}^2 = q \cdot U$ and so the eq. (65) can be rewritten in eq. (66)

$$\tan(\theta) = \frac{m^{0.5} \cdot I}{2^{2.5} \cdot \pi \cdot \varepsilon_0 \cdot q^{0.5} \cdot U^{1.5}} \cdot \frac{S}{d} \quad \textbf{(66)}$$

It is interesting to notice that the last expression includes the perveance P as defined in 2.2.3 ($P = \frac{\varepsilon_0 \cdot U^{3/2} \cdot q^{1/2}}{J \cdot L^2 \cdot M^{1/2}}$) ; this means that if the ratio $\frac{I}{U^{1.5}}$ doesn't change the reciprocal beam divergence does not change as well.

In case of 4 beamlets equally spaced, (see Figure 90) the beam divergence for one beamlet have to take into account not only the effect of one beamlet but three forces component should be added, this means to multiply the eq. (66) ,by a factor α=2.12 $\left(\sqrt{1^2+1^2} + 1/\sqrt{2}\right) \approx 2.12$.

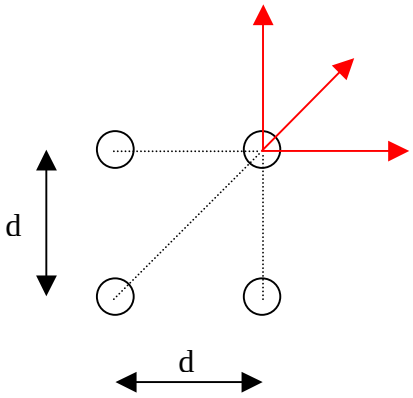

Figure 90 The 4 beamlet case , (top view) each force component acting on one beamlet is shown by red arrows

Figure 91 shows the beam deflection obtained both in analytical and numerical code for several parallel velocities $v_{par} = \sqrt{\frac{2 \cdot q \cdot U}{m}}$, the figure shows that analytical and numerical results are compatible confirming the reliability of the trajectories integration of IRES.

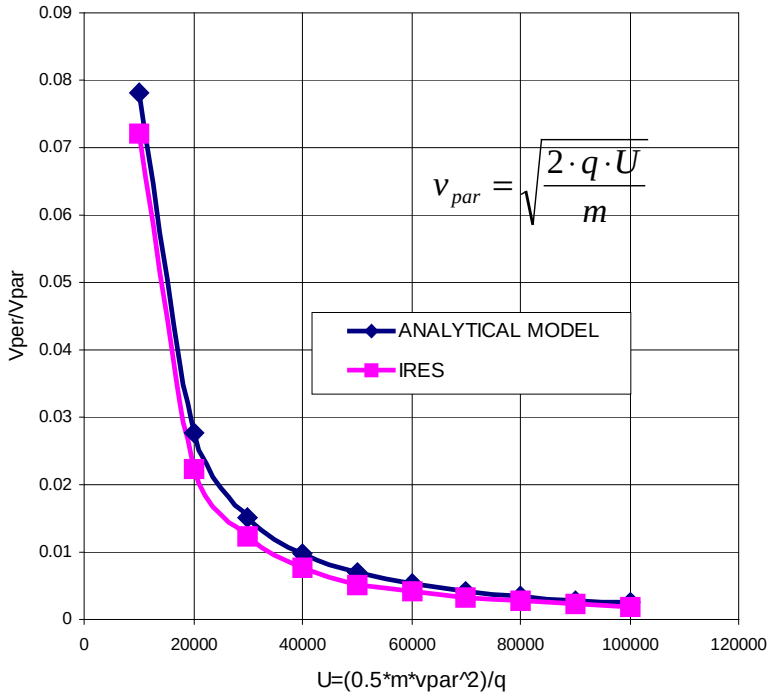

Figure 91 The beams deflections evaluated by the analytical approach and by IRES

4.3.3 The beamlet-beamlet interaction: the SINGAP configuration

IRES has been applied to the 1MV ITER accelerator with a single gap configuration (SINGAP) to study the trajectories of negative ions. In this case the simulation domain is included between the pre-acceleration grid and the grounded grid (see. Figure 16). The electrostatic field is not exactly uniform because the grounded grid of SINGAP is curved both in horizontal and vertical direction in order to focus the beamlet group (see Figure 92), the code has been tested starting from an uniform electric field map where $E_x = E_y = 0$ and $E_z = C$ everywhere. The analyses reported here don't reproduce the experimental conditions and are aimed to understand the importance of the beamlet-beamlet interaction in the SINGAP accelerating gap, before to proceed with more accurate simulation by OPERA.

The code, exploiting the double planar symmetry of the accelerator, simulates a quarter of the whole 1280 beamlets, it integrates the particles trajectories in the space between the pre-accelerating grid and the grounded grid. Figure 92 shows the front view of the grounded grid in SINGAP configuration, the vertical and horizontal symmetry planes are highlighted by the dotted lines.

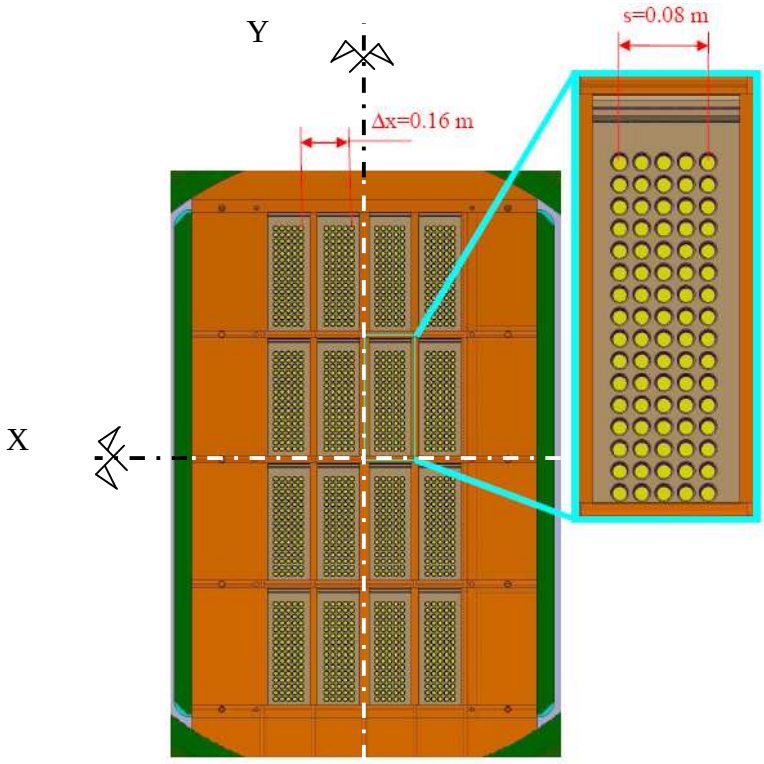

Figure 92 Grounded grid, front view

If the beamlets do not interact reciprocally, the components of displacements (respect to the initial position) in XY plane for the last particle positions is 0.

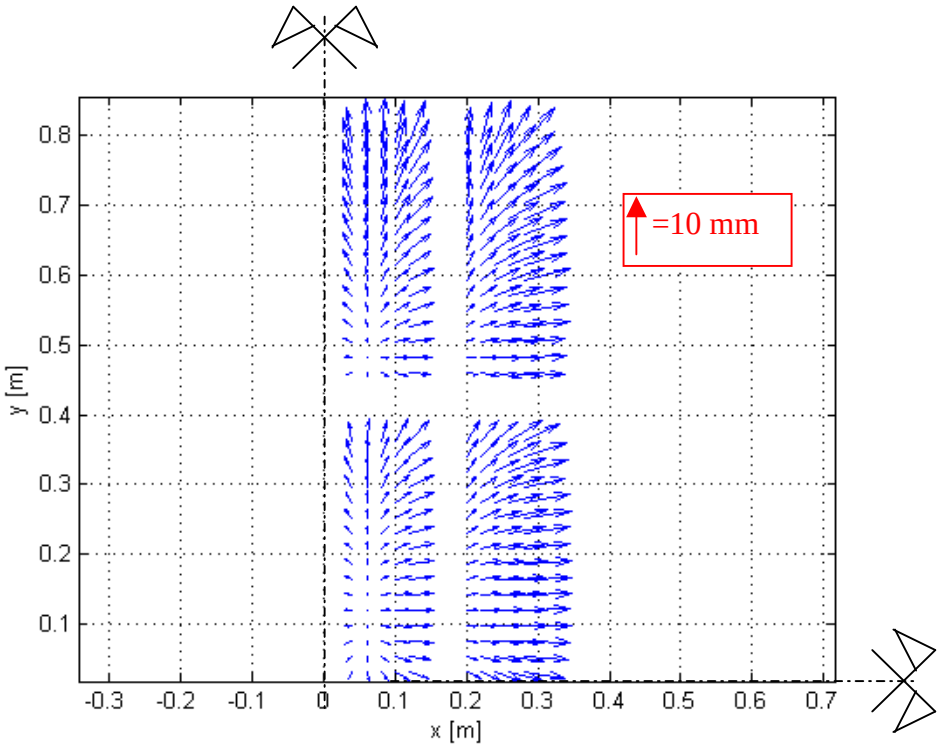

Figure 93 Displacement vector plot in the plane x-y (orthogonal to the beam direction) evaluated at the end of each trajectory. On the grounded grid

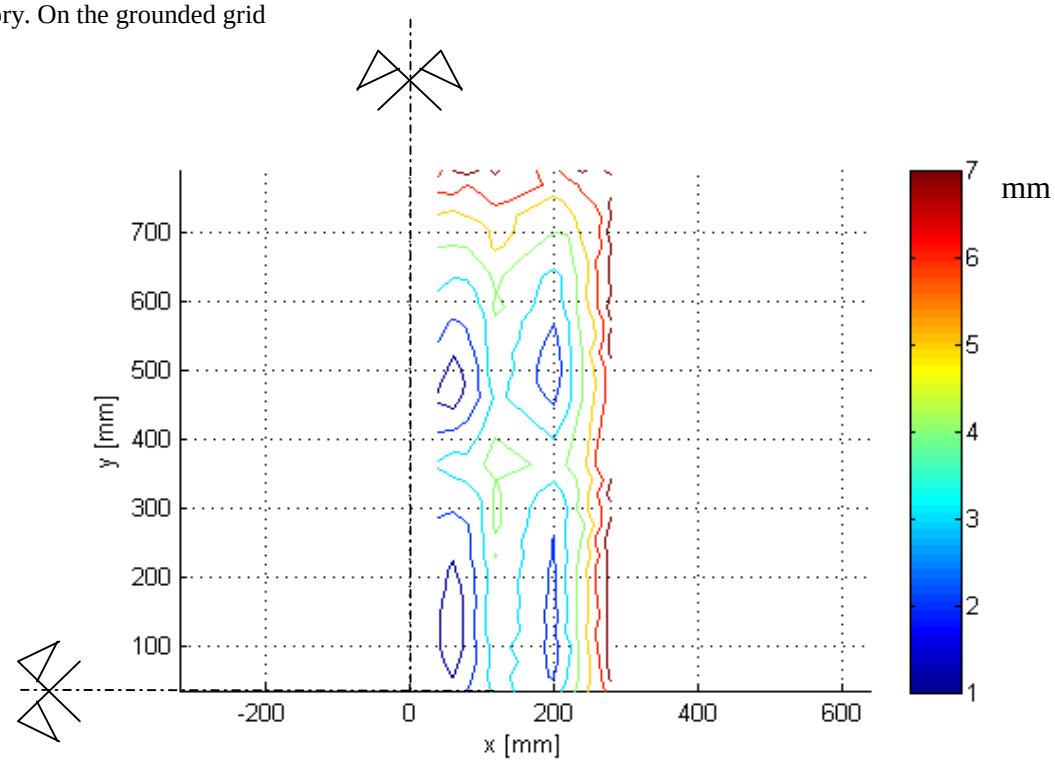

Figure 94 Displacement contour plot in the plane x-y (orthogonal to the beam direction) evaluated at the end of each trajectory (at $Z=Z_{GG}$)

Figure 93 and Figure 94 shows the displacements due to the beamlet-beamlet interaction, where a vector plot and a contour plot are respectively shown.

In both figures is shown a quarter of the whole beamlets group, the axis x=0 and y=0 correspond to the dotted line of Figure 92. It can be appreciated how the xy displacements are bigger in the outer part, in general, the beamlet deflection can be considered the sum of two effect: the first one concerns the interaction inside the beamlet group (array of 5x16, see Figure 92) while the second one considers the long range effect due to the interaction between each beamlet group; this is the reason why the beamlet closer to the symmetry planes have no lateral displacement.

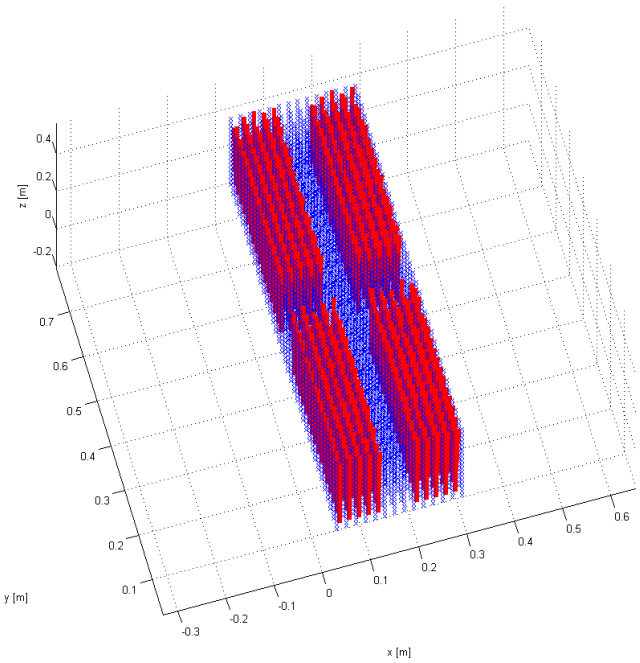

Figure 95 The integrated trajectories (red lines) and the node for the field computations (blue points).

Figure 95 shows a 3D plot of the integrated trajectories (red lines) while in blue are showed the 3D uniform grid of nodes where the electric field is updated at each code iteration.

The deflection in terms of v_{per}/v_{par} evaluated at the final position of each trajectories (where the particle reach the grounded grid) are shown in Figure 96 and Figure 97, respectively for $e_x = v_x/v_z$ and $e_y = v_y/v_z$. Although the simulation was carried out for the simple case where the external electric field was uniform and directed only along z, the results show a beam divergence of 20-25 mrad. This value is not compatible with the NBI requirements because it means not only to defocus the beam but also to deposit the beam power on the components placed downward the electrostatic

accelerator. To compensate this divergence a suitable grid shaping is applied to the grounded grid, in this manner, the equipotential lines inside the accelerator are curved.

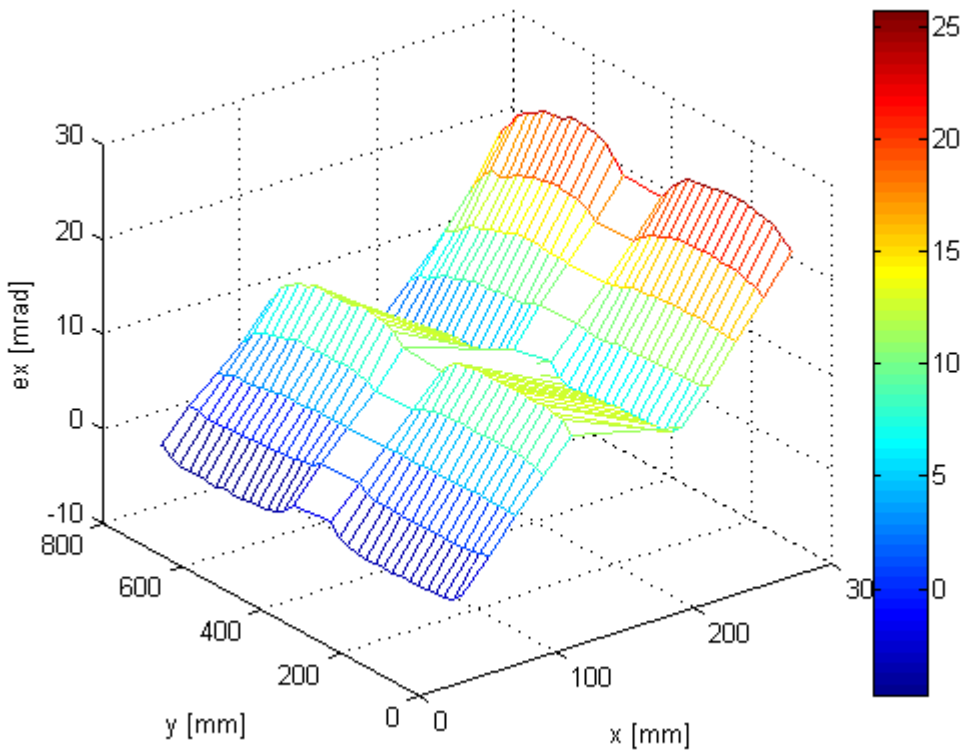

Figure 96 The deflection map $e_x = v_x / v_z$ evaluated at the end of each trajectory.

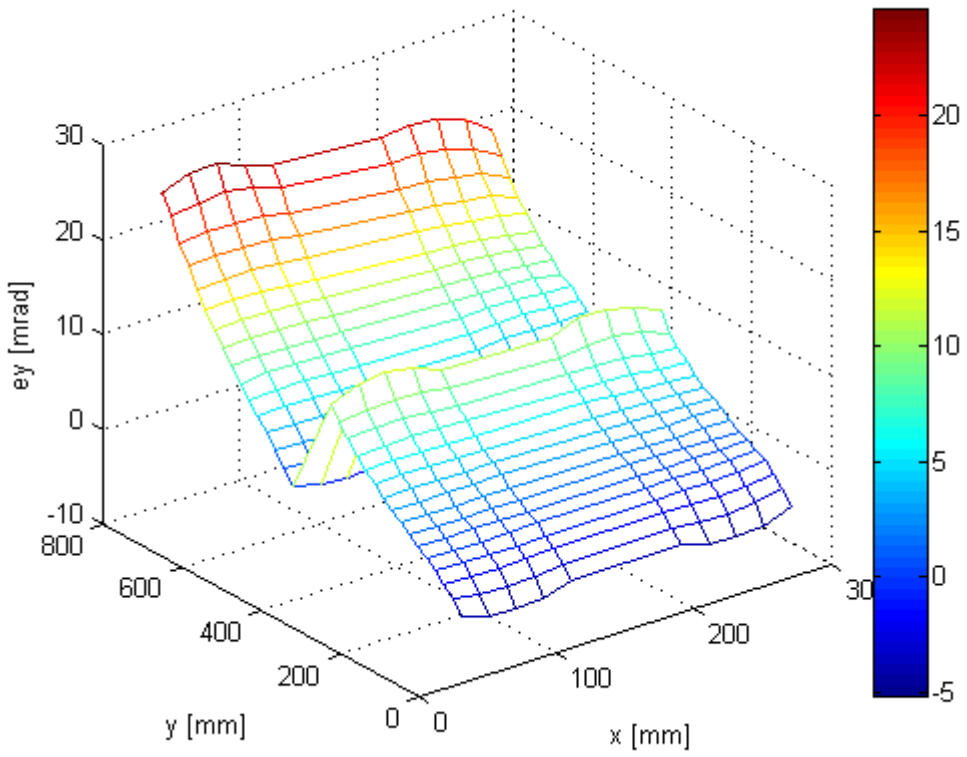

Figure 97 The deflection map $e_y = v_y / v_z$ evaluated at the end of each trajectory.

The effective geometry of the grounded grid is shown in Figure 98 where a curvature of few degrees is foreseen to focus the whole group of beamlets. In this case the effect of this offset should be calculated by IRES. The most convenient approach to carry out this effect is study the grid curvatures by 2D simulations, for this purpose, the 2D electrostatic finite element models solving the Laplace's equations should be used to carry out the analyses by IRES. The results of such models should be imported at iteration 0 and successively updated by IRES.

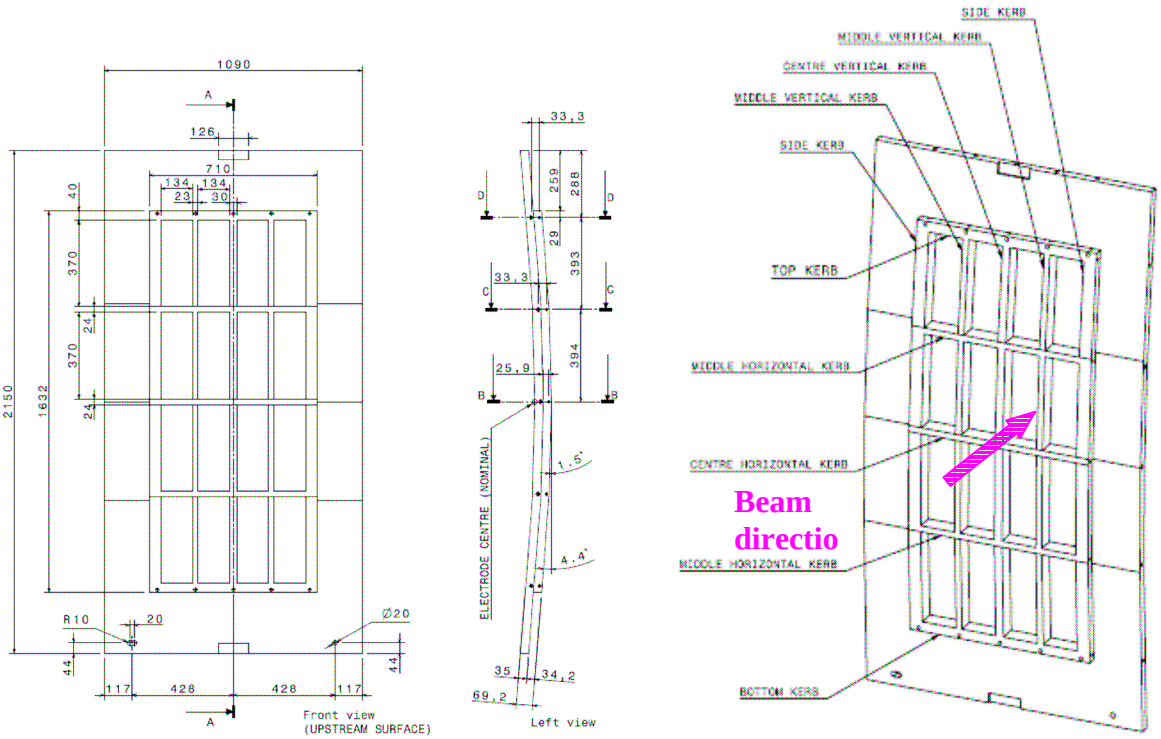

Figure 98 The SINGAP grounded grid design.

The electric field at the iteration 0 has been calculated by ANSYS, the results are shown in the following figures where both for the horizontal and the vertical accelerator sections, shown in Figure 99 and Figure 100, a two bi-dimensional finite element models has been developed. The figures from Figure 101 to Figure 104 show respectively the equipotential line and the electric field distribution for the horizontal and vertical cross section.

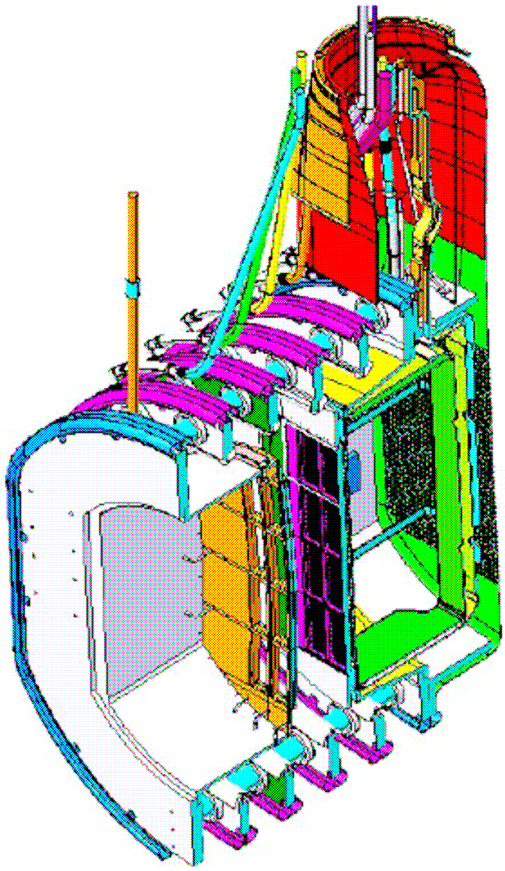

Figure 99 A 3D vertical cut view of the accelerator for the ITER NBI

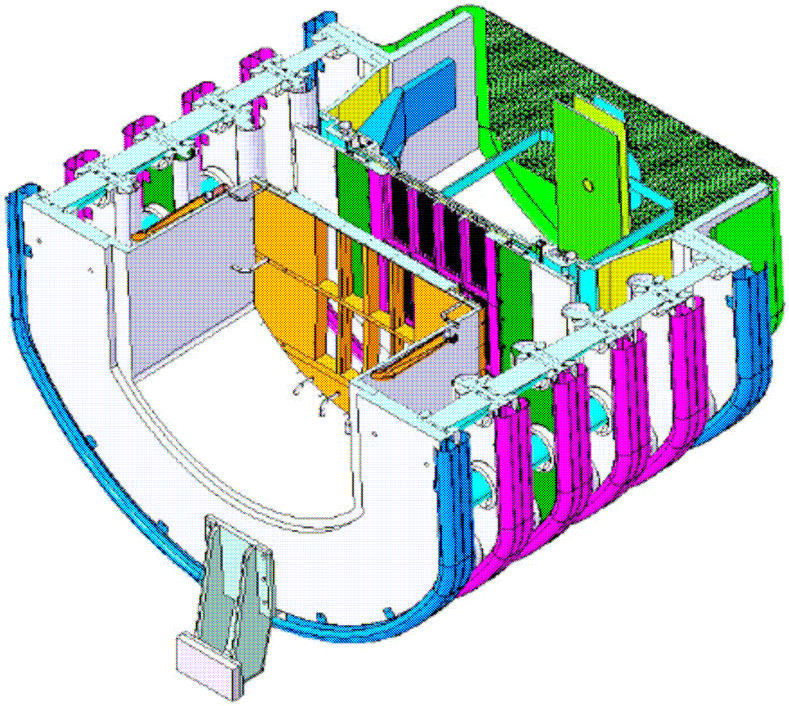

Figure 100 A 3D horizontal cut view of the accelerator for the ITER NBI

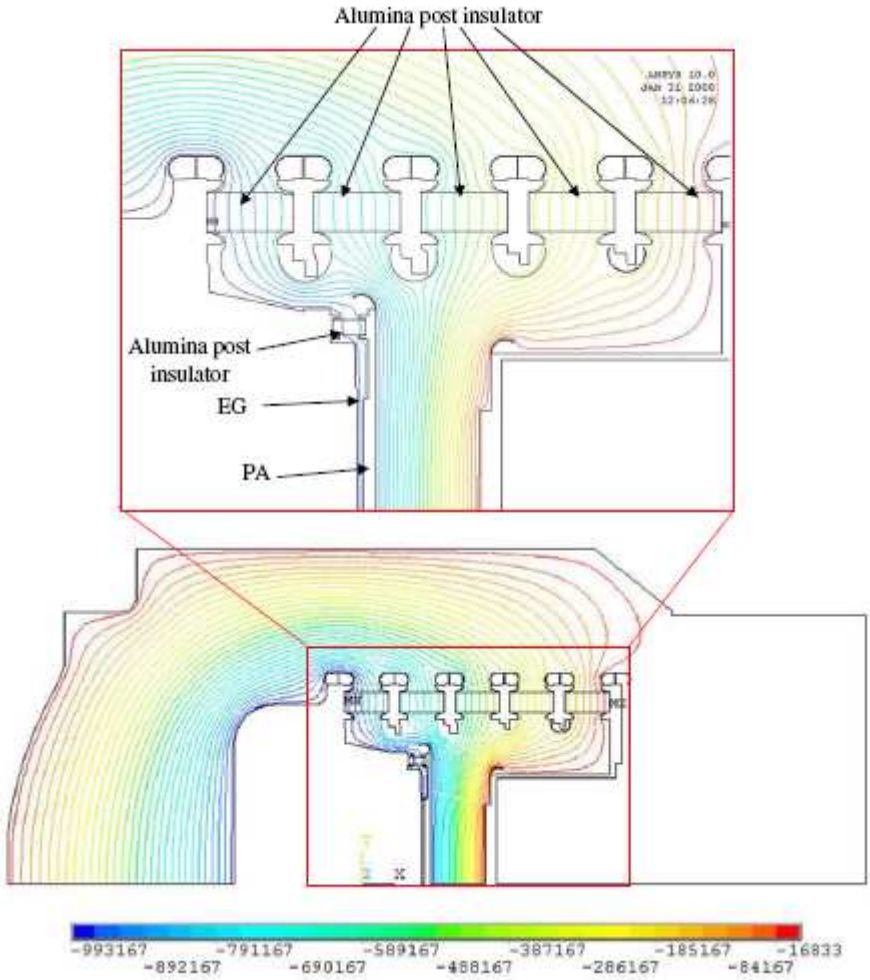

Figure 101 Equipotential line on the equatorial plane of the accelerator

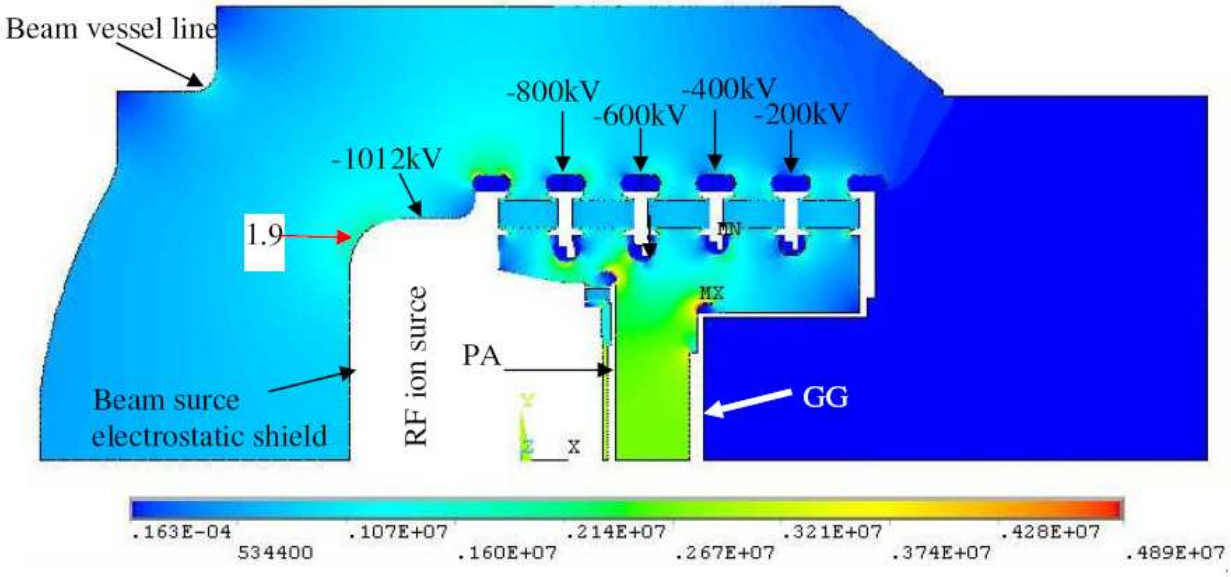

Figure 102 Electric field amplitude on the accelerator equatorial plane

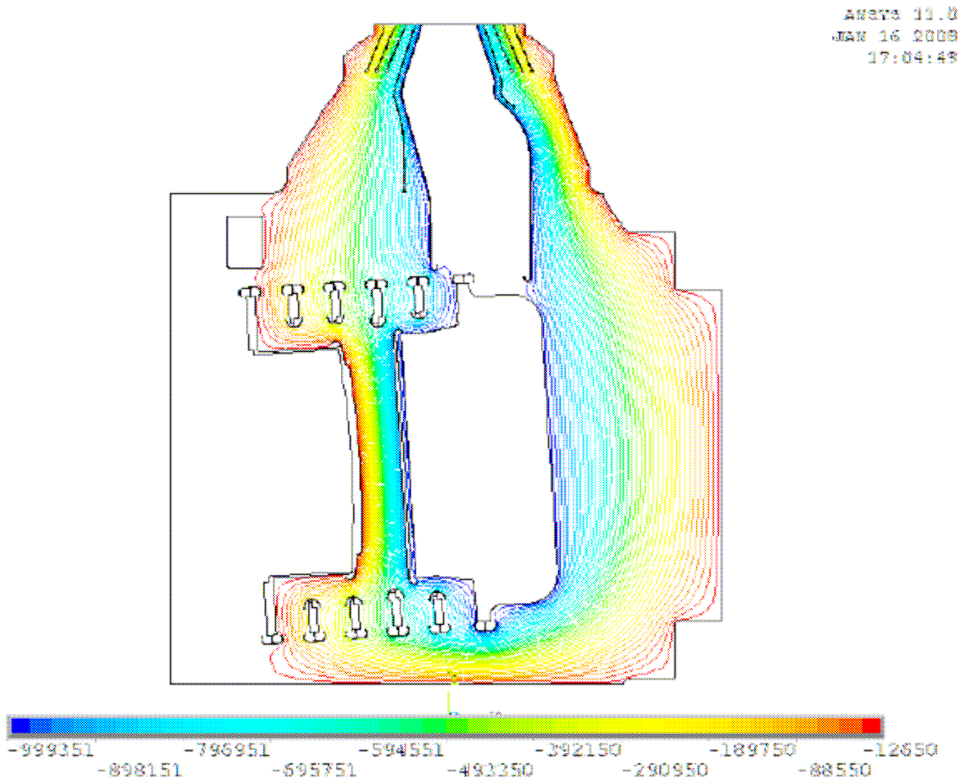

Figure 103 Equipotential line on the vertical section of the accelerator

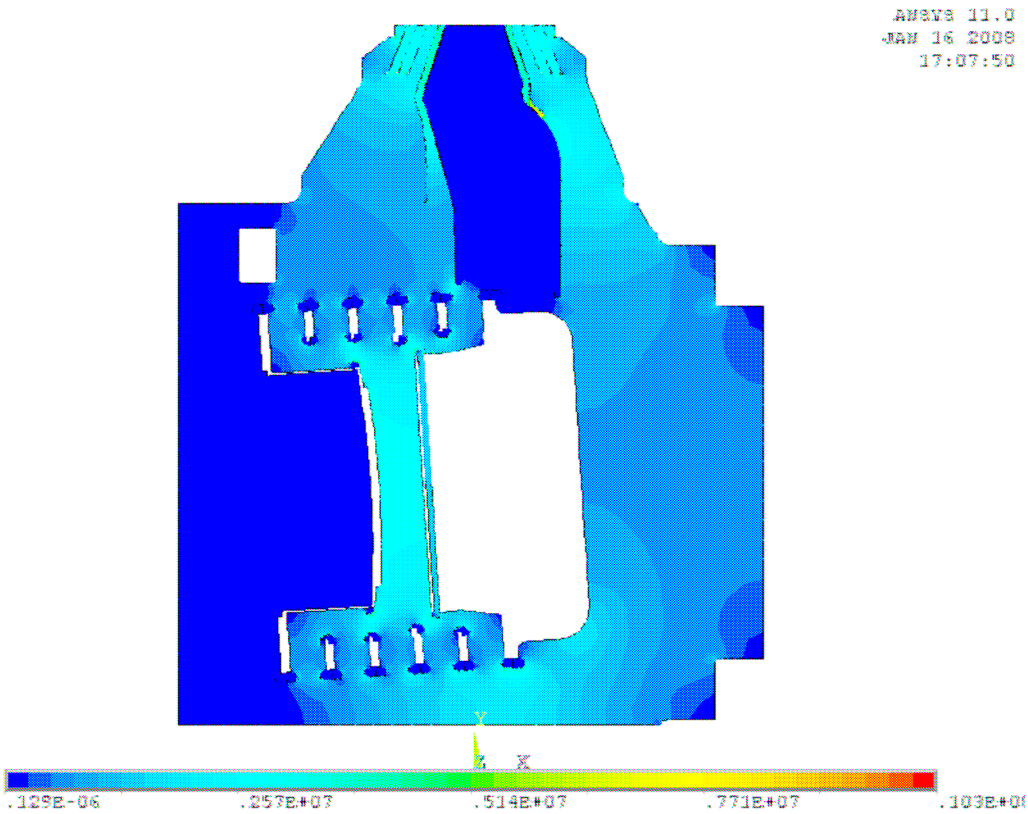

Figure 104 Electric field amplitude on the vertical plane of the accelerator

By Figure 103 it can be noted how a slight grounded grid curvature bends the equipotential lines inside the accelerating gap.

The results obtained by the finite element codes should be sampled by an equally spaced bi-dimensional grid and than they will be imported in a 2D version of IRES, in this case the beam divergence will be estimated considering both the spatial charge effect than the grounded grid curvature.

Chapter 5: Beam steering and thermal load handling

5.1 Introduction

The possibility of tilting the beam both in the vertical and on the horizontal planes, without opening the vessel, is the main motivation for the conceptual study of an active steerer. A steering system based on magnetic fields generated by internal coils can in principle allow these operations. The conceptual design of such a system should demonstrate the capability of providing steering for the angles required for the on-off axis injection and at the same time should demonstrate that the steering is accurate enough to correct for small misalignments of the components. Such a system should also demonstrate the capability of handling the power load due to the electrons generated by stripping and ionization losses [55] inside the accelerator. These electrons are subjected to a stronger deflection by magnetic field, so that the system should be equipped with an in-built Electron Dump system. In order to be effective such a system should be placed in the space between accelerator and neutralizer. In this way an integrated Electron Dump and Steering System (EDSS) can also protect the Neutralizer leading edge.

5.2 Scheme of an active steering system

The active steering concept is based on a system by which negative ions and electrons are deflected by a magnetic field produced by a suitable set of active coils. The system should provide negative ion steering both in vertical and horizontal directions and at the same time should remove the unwanted electrons produced and accelerated inside the accelerator. To provide this double function, two different schemes have been considered, the Single Stage Steerer (SSS) and the Double Stage Steerer (DSS).

The Single Stage Steerer (SSS) is a system based on a single deflection. In

Figure 105 a top view of the SSS scheme applied to ion steering is shown. The electrons leaving the accelerator are also deflected and intercepted by a dump. The main advantage of such a system is the limited space allocated for magnetic field coils. The main drawback is that the electron deflection changes with the negative ion deflection therefore the ion steering capability is constrained by the dimensions of the panels intercepting the electrons along the beam direction.

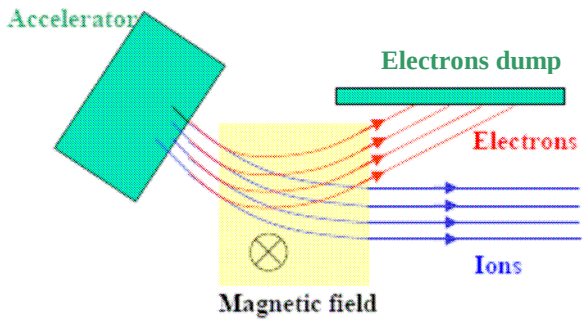

Figure 105 Electron dump and steering system concept for the Single Stage Steerer

The scheme of the Double Stage Steerer (DSS) is shown in Figure 106. In this scheme, the first stage magnetic field filters the electrons deflecting them towards the electron damp, while the second stage compensates the deflection undergone by the negative ion trajectory to the selected value.

This scheme allows the electron heat flux deposition to be decoupled from the beam steering as the two set of coils can produce different magnetic fields; a misalignment of the order of 6mm is produced between inlet and outlet.

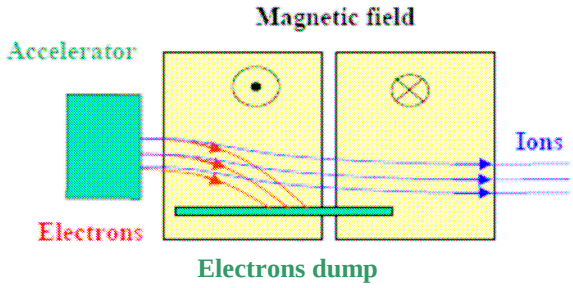

Figure 106 Electron dump and steering system concept for the Double Stage Steerer

In both schemes an iron yoke is necessary to prevent the stray magnetic field produced by the active coils from penetrating the acceleration region. It is worth noting that the iron yoke could also act as

a protection for the cryo-panels, intercepting the secondary electrons emitted by the electrons dump panels.

In order to verify the feasibility of a steerer system, three key aspects have been addressed: the compatibility with the available space between the Ground Grid of the Accelerator and the Neutralizer, the coil size requirements to provide the magnetic field configuration necessary for an uniform steering of the beam and the cooling requirements to handle the heat power load deposited by the electrons on the dump plates. These aspects are addressed in the following.

5.3 Overall dimension requirement

The system should be placed between the Ground Grid (GG) of the Accelerator and the Neutralizer. The SINGAP configuration and the corresponding mechanical support designed for the grids have been taken as the reference design. In Figure 107 and Figure 108 a horizontal and a lateral cut-view of the whole accelerator and of the neutralizer are shown. Since the active steerer should be integrated with the Accelerator, it should be fixed to the Grounded Grid (GG) support structure, so that the lateral and vertical dimensions are constrained by that.

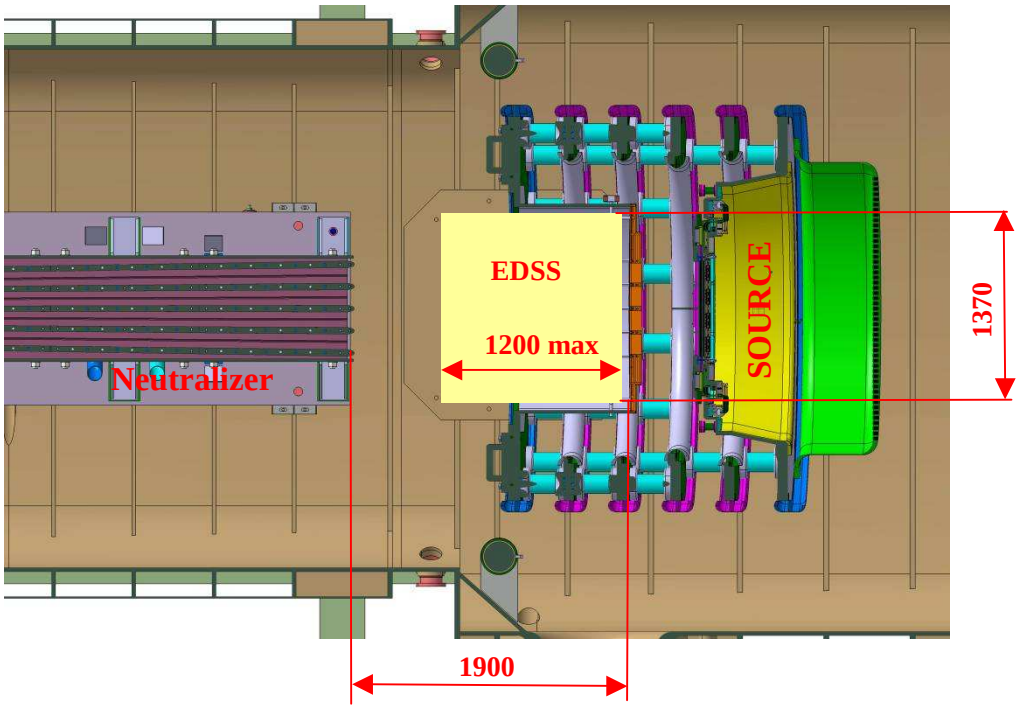

Figure 107 Beam source, accelerator and neutralizer top cut-view

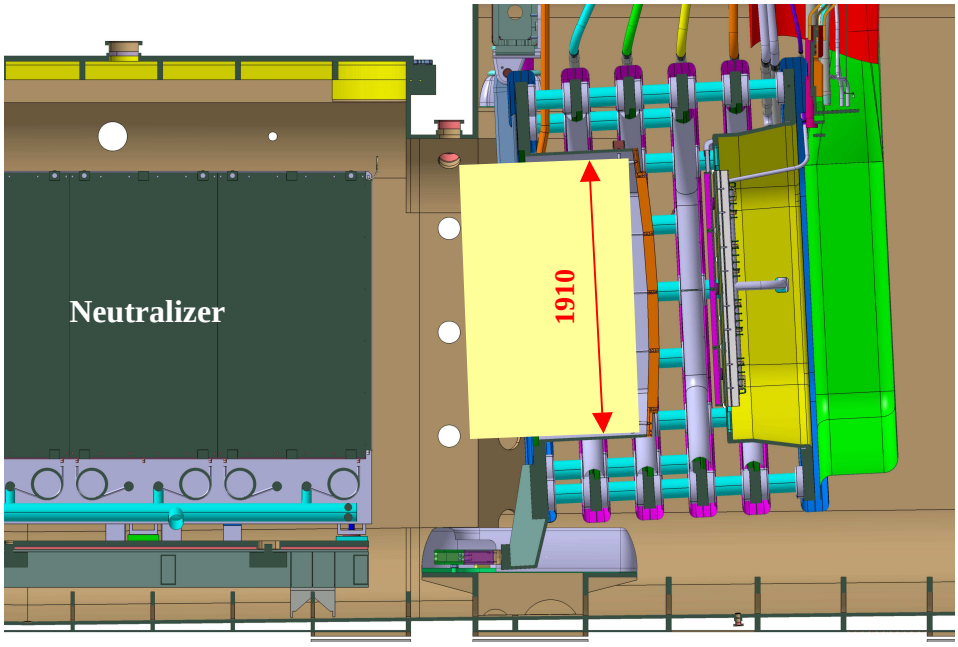

Figure 108 Beam source, accelerator and neutralizer lateral cut-view

According to the present design of the accelerator (see reference [64]) , the maximum dimensions of the steerer are 1910mm in the vertical direction and 1370mm in the horizontal direction, in order to position the system inside the grounded grid frame. The distance between grounded grid and neutralizer leading edge is 1900mm. According to Figure 107, a maximum extension of 1200mm has been assumed, but further investigations on pumping efficiency should be carried out.

5.4 Magnetic field and related coil requirements

An analytical study describing the electron and negative ion deflection in an uniform magnetic field has been carried out in order to estimate the magnetic field necessary for a deflection compatible with the maximum dimensions of the system deriving from the considerations in the previous section. The model cannot deal with the effect of the non uniformity of the magnetic field; however it can provide useful guidelines to design the single stage steerer. For this purpose, a model describing the deflection undergone by electrons and negative ions in a uniform magnetic field has been developed and applied to the horizontal deflection. In particular the model has been applied to horizontal steering, to study the effect on the electrons of an ion beam deflection of 3 mrad. The analysis is aimed to verify the feasibility of an electron dump system in a space compatible with the

maximum dimensions available for the dumping plates. The model is based on a simple evaluation of the trajectory made by using circumference arcs where the uniform field applies and straight line elsewhere. The incidence and deflection angles are related through the relationship: $R_L \cdot \sin(\alpha_1) = \Delta Z = a + R_L \cdot \sin(\alpha_2)$.

The Larmor Radius $R_L = \frac{\gamma \cdot m \cdot v}{q \cdot B}$ includes the relativistic factor $\gamma = 1 \Big/ \sqrt{1 - v^2 / c^2}$. It is worth noting that in this case γ is constant as the particles are subjected only to magnetic field. The minimum and maximum magnetic field corresponding to the minimum and maximum deflection angle for a given incidence angle can be derived by geometrical considerations

$$By_{\min} = \frac{\gamma_i \cdot m_i \cdot v_i \cdot [\sin(\alpha_{2i\min}) - \sin(\alpha_1)]}{a \cdot q} \qquad By_{\max} = \frac{\gamma_i \cdot m_i \cdot v_i \cdot [\sin(\alpha_{2i\max}) - \sin(\alpha_1)]}{a \cdot q} \qquad \textbf{(67)}$$

The consequence of the horizontal steering of the ions in the SSS is that the electrons are also deflected, so that they can be intercepted by dumping plates placed in a suitable position.

The model for ions and electrons is shown in Figure 105. In particular in Figure 109 the trajectories are shown for the ions in a range of magnetic field amplitude By. In this case the uniform magnetic field is assumed to apply in the region 0<z<a.

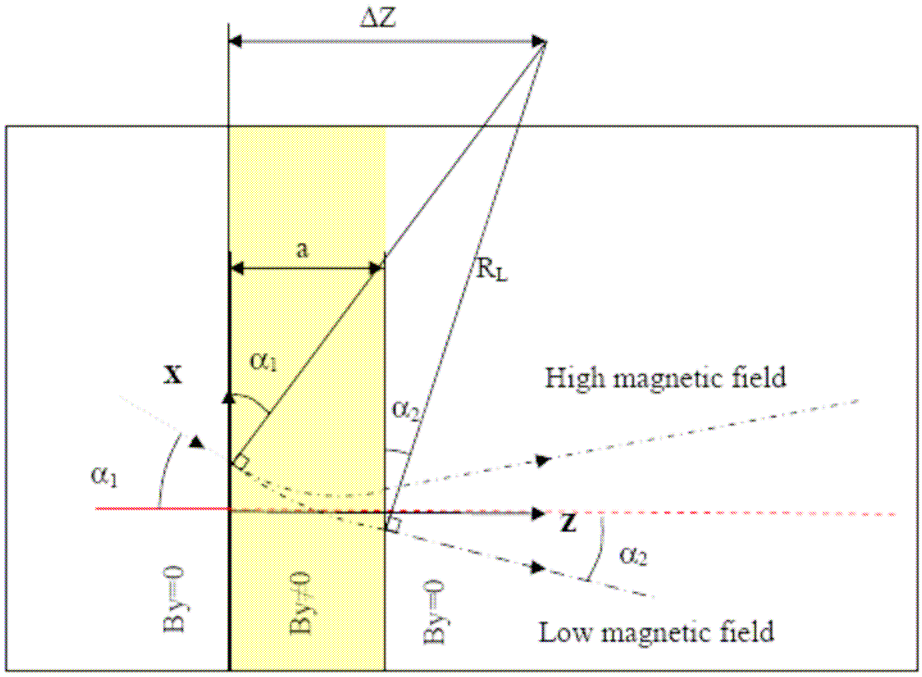

Figure 109 Ions trajectories (dotted lines) with high and low magnetic field By for the single stage steerer

As the location and extension of the electron dump plate are constrained by the dimensions discussed above, the magnetic field required to achieve the ion deflection and to intercept the electrons has been estimated by substituting those numbers in eq.(67). For this estimate the ion energy has been assumed 1MeV, while the electron energy has been assumed to be 0.96 MeV, according to the results of numerical simulations of SINGAP at 1MV (pag.33 of [22]). The beamlet group width "s" and the distance between beamlet groups "Δx" have been set equal to those in the Grounded Grid (GG) design (shown in Figure 92), namely s=0.08 m and Δx=0.16 m.

As a consequence, the space between each couple of electron dump plates "c" must be lower than the horizontal periodicity Δx=0.16 m, and in this case it has been set to c=0.12 m.

Therefore the study of the SSS has been carried out as a function of two parameters: the incidence angle of the beam α_1 and the extension a of the area where the magnetic field By is applied. By setting a=0.6 m to minimize as much as possible the overall dimension of the electron damping plates, the minimum ad maximum values of magnetic field required for ion deflection , the max and min Z and relative incidence angle for the electrons have been obtained for minimum ad maximum ion deflection angles α_{2max} and α_{2min}. The results for α_{2max}=+3 mrad and α_{2min}=-3 mrad are shown in Figure 110.

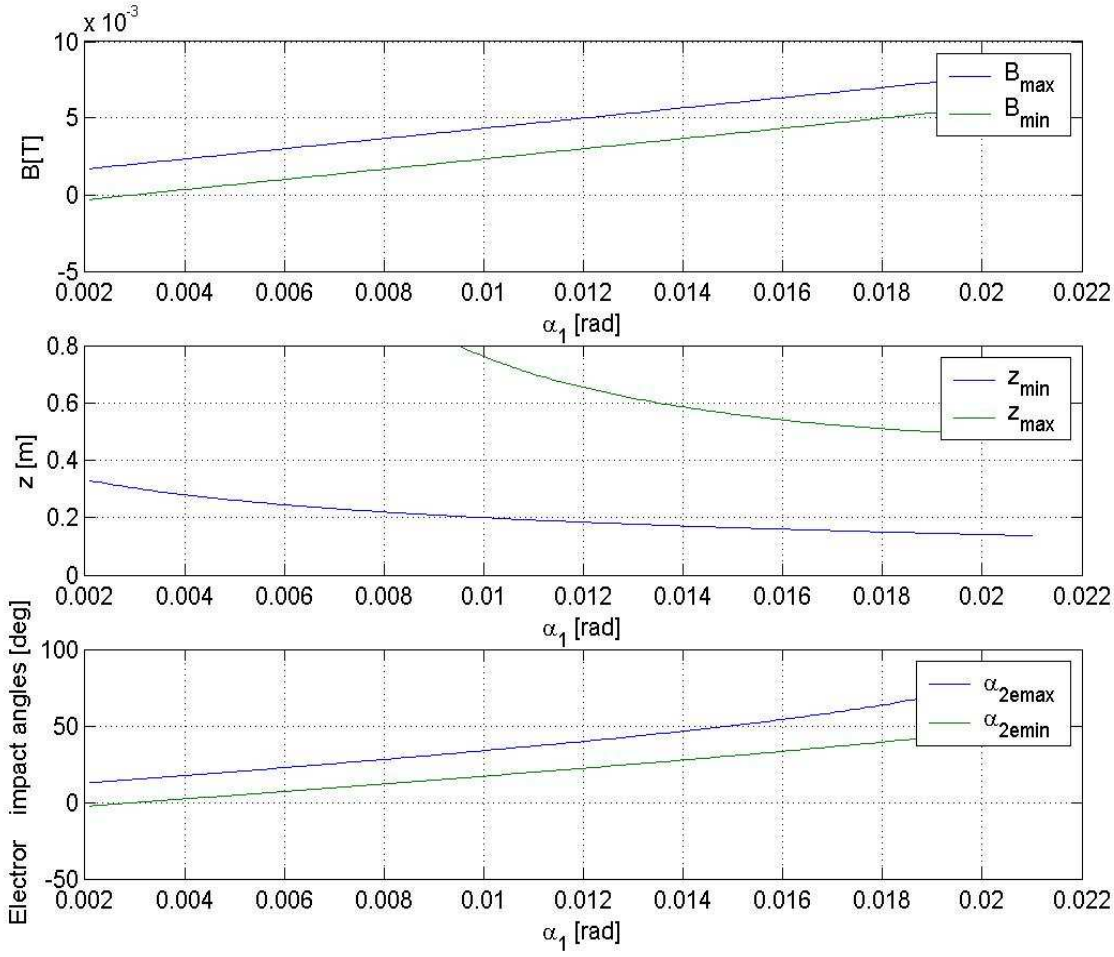

Figure 110 Results of the analytic model for the single stage solution

All the diagrams of Figure 110 show two plots for each α1 , the green lines belong to the case with ions deflected by +3mrad, while the blue ones correspond to the case with ions deflected by -3mrad in the horizontal plane. It is found that the magnetic field has to be within the range 0 to 10mT. It is also found that for an incidence angle lower than 0.014 rad, the electron trajectories exceed the overall dimensions of the electron damping plates. The model gives useful indications about the criteria to be applied to design the system, as lower values of a1 mean longer dump dimensions, while higher values of a1 could cause excessive heat flux deposition due to the smaller impact angle of the electrons on the plates.

A model has also been developed to study the beam deflection on the horizontal plane due to the combination of two set of coils as in the Double Stage Steerer. In this model a limited number (nine) of trajectories has been calculated using an ANSYS macro (PLTRACK) and a Newton Raphson algorithm has been implemented to compute the particle trajectory inside each element. The exit point from an element is the point where the particle trajectory meets the plane of

bounding surface of the elements; the algorithm is based on Gyimesi et al. [66] and applied to each array of beamlets. This tool allows particle tracing within an element accurate up to machine precision. In this model no spatial charge effect has been considered. In Figure 111 a scheme of the Grounded Grid as seen from the neutralizer is shown. The ions exit orthogonally to the plane that contains the grounded grid. The ratio between the two transverse velocities (vx, vy) and vz, has been evaluated in a plane located 3.66 m downstream with respect to the Grounded Grid (GG).

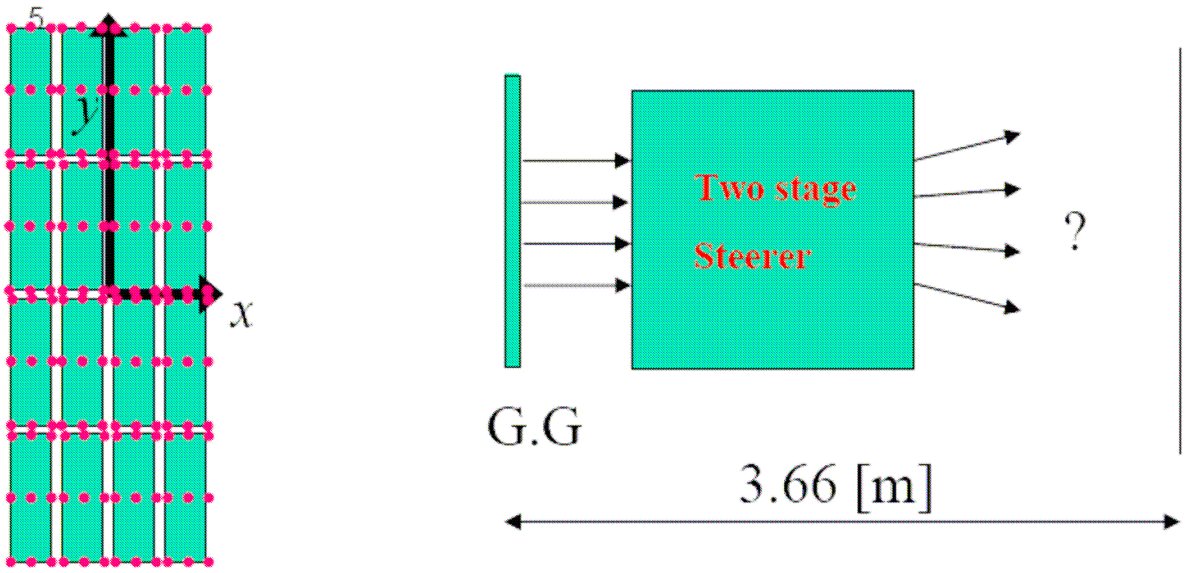

Figure 111 Scheme of the Grounded Grid, of the DSS and of the plane where is computed the emittance.

The ion trajectory, for the double stage solution, results in a double bend; in Figure 112 the results are plotted as a function of the current difference in the two sets of coils. The central point with $\Delta I=0$ corresponds to equal and opposite currents in the coils (namely 1780A), the corresponding deflection is near to 0. The diagram also shows the error bar that represents the standard deviation evaluate for the whole set of 144 proof beamlets (9x16=144). Although the results shown in Figure 112 has been obtained with a laminar model, it is possible to appreciate how the influence of the magnetic field produced by several discrete coils causes a spread of the beam on a large scale: this surely means an increase of the beam emittance as defined in chapter 2.

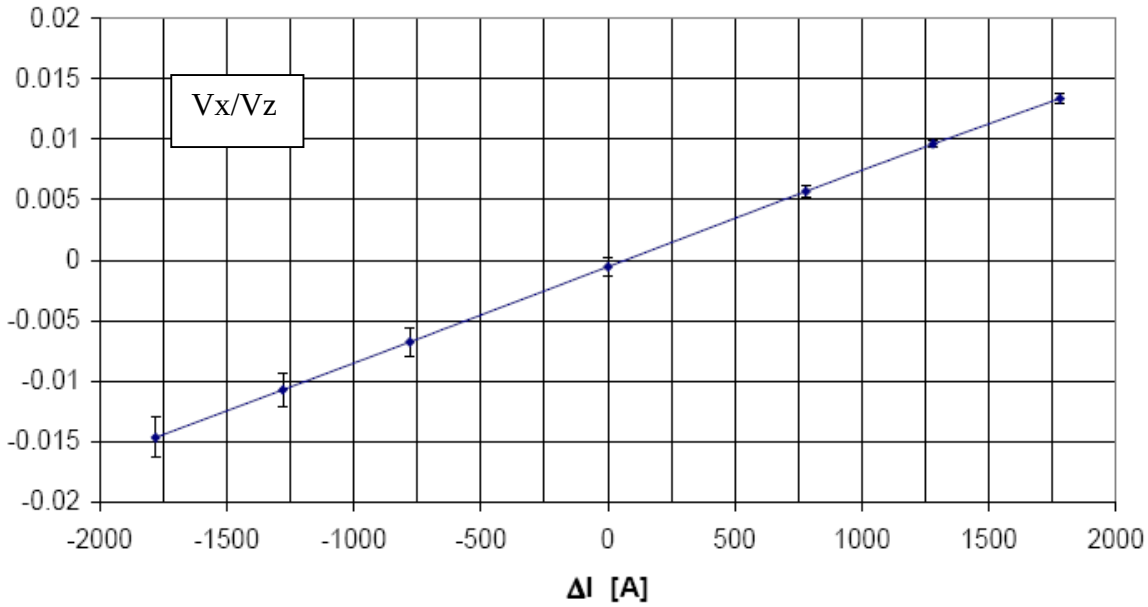

Figure 112 Horizontal spread of the ratio between transverse and longitudinal velocity evaluated at different current unbalances

The results shown in each diagram indicate that the horizontal steering capability of the system easily fulfils the requirements, the standard deviation σ is 0.796 mrad for ΔI=0. The non vanishing σ has been interpreted as due to the non uniformity of the magnetic field, so that a suitably shaped coil system is needed to reduce this effect. The results presented in this section have been obtained by the particle tracing implemented in ANSYS, further improvements could be carried out using IRES; the code could be applied to re-calculate the results shown in Figure 112 taking into account the effect of the spatial charge on the beamlet divergence.

5.5 The conceptual designs

In order to study the optics uniformity of the steerer, the magnetic field produced by realistic coils should be considered to take into account the effects due to the non uniformity of the magnetic field and neglected in the analytical model. The front view and a 3D view of the scheme of the SSS are shown in Figure 113.

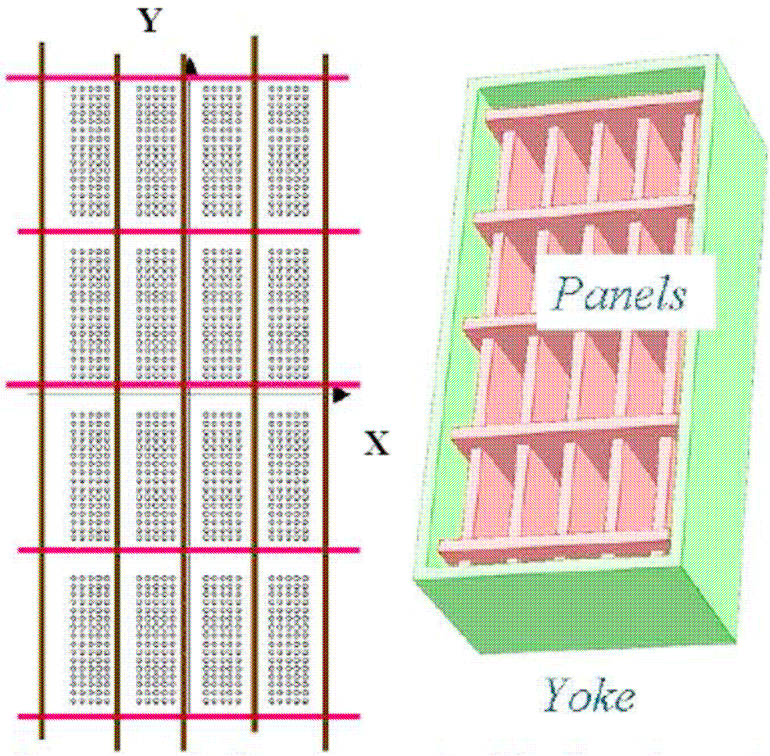

Figure 113 Single stage solution

The single stage steerer is a system based on two sets of coils: the first one, as explained above, is aimed to generate a vertical field that filters the electrons and deflects horizontally the ions, while the second set of coils, integrated with the electron dump panels, is aimed to generate a horizontal magnetic field B which controls the vertical tilting of the beam.

In Figure 114 the Finite Element model for the DSS developed for the emittance and thermal load analysis is shown. The DSS consists of three sets of coils, two sets are aimed to generate a vertical magnetic field to deflect the electrons and to re-align the beam in the horizontal plane and one set is aimed to produce a horizontal magnetic field for vertical beam steering.

In both concepts, coils and plates are surrounded by an iron yoke.

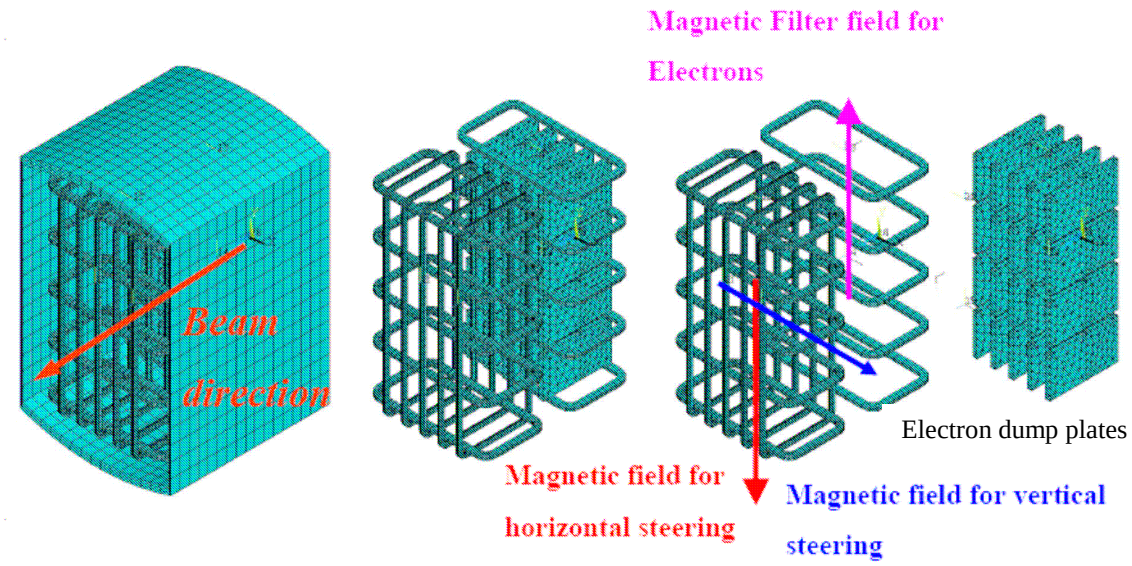

Figure 114 Finite element model for the double stage solution

The resulting magnetic field distribution for a DSS is shown in Figure 115. In the region close to the coils the vertical magnetic field appears non uniform so that some effects on the beam optics and electron power deposition are expected.

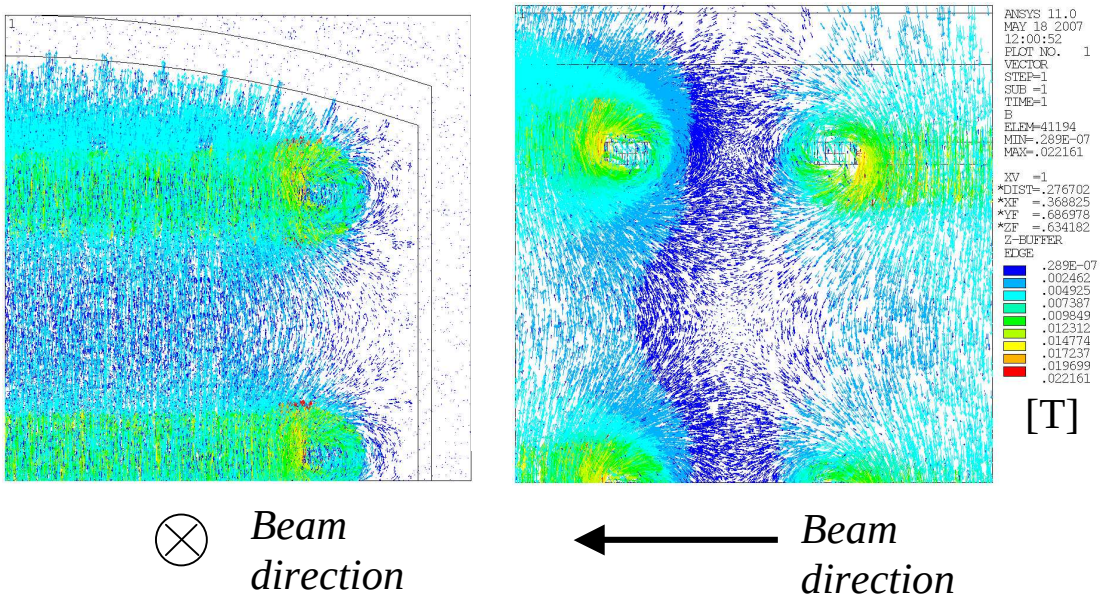

Figure 115 3D Magnetic field vector plot for the DSS shown in Figure 114. The vector field plots are shown respectively for a front and lateral view

5.6 Uniform beam steering and magnetic field requirements

The deflection angle of a charge moving in a magnetic field can be described in paraxial approximation considering the sketch of Figure 116 where the ion deflection has been considered in a zone where the magnetic field exists and it is orthogonal to the plane defined by the trajectory curvature.

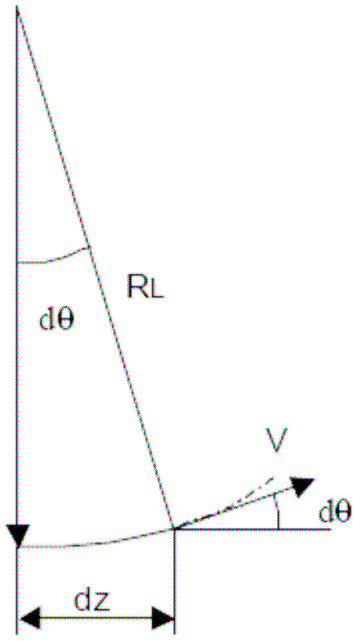

Figure 116 Ion deflection scheme in paraxial approximation

The small deflection angle q, in paraxial approximation, can be approximated by the velocity ratio vy/vz, in principle it should be obtained integrating the law of motion in time. It is possible to demonstrate that the same result can be obtained using eq. (68), where the velocity is derived by energy conservation q ×U = m×c^2 ×(γ -1) , U is the particle acceleration voltage, q the particle charge and $T_x = \int B_x \cdot dz$.

$$\Delta\theta = \frac{c \cdot sign(q) \cdot T_x}{\left(U^2 + 2 \cdot m \cdot c^2 \cdot \left|U/q\right|\right)^{1/2}} \qquad \textbf{(68)}$$

It is worth noting that in the presence of a non uniform magnetic field the deflection angle depends on the integral of the magnetic field T, so if we calculate T for each beamlet it is possible to obtain a map in the plane x-y (orthogonal to the beam direction) which is proportional to the beam

deflection. Optimising the Steering System means obtaining a uniform deflection for each beamlet; this requires producing obtain a uniform map of T.

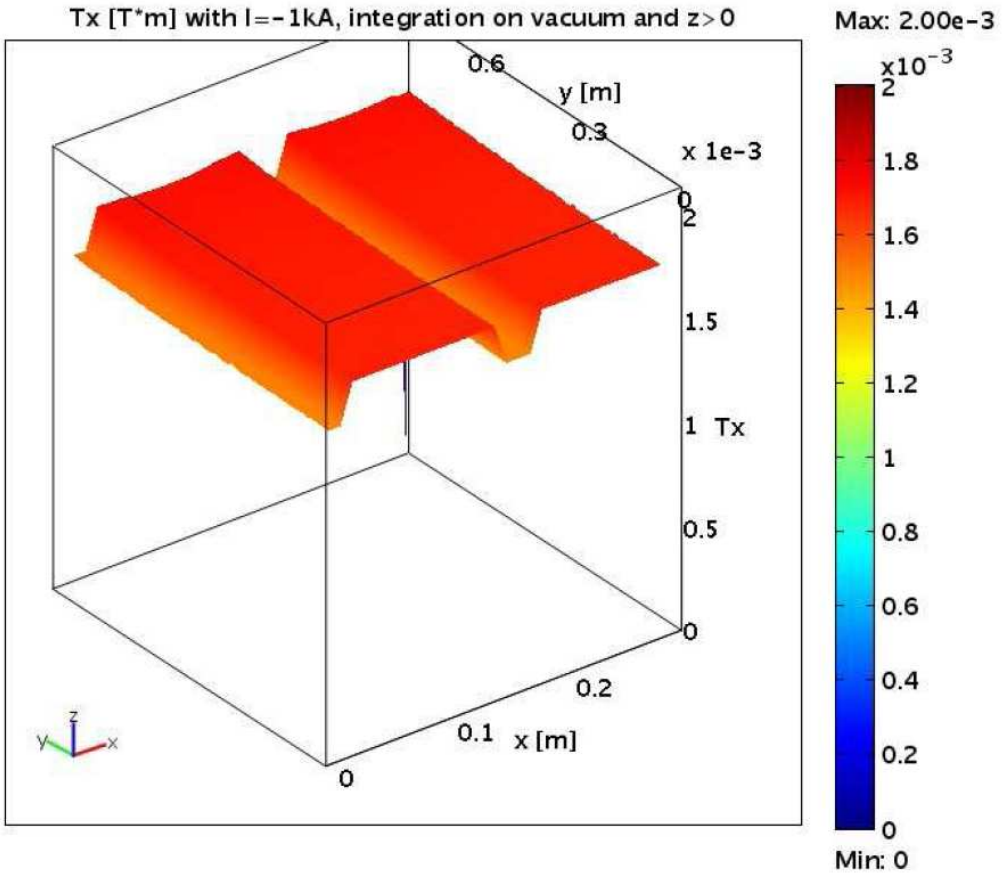

Figure 117 Map of T(x,y) . Uniform deflection for the vertical beam deflection [46]

Figure 117 shows the map of T calculated for the vertical deflection of the negative ion beam. It can be noted that T appears uniform; the grooves in the figure depend on the fact that the integral has been interrupted inside the coils, so are not correct in these two zones.

5.7 Power load deposition on the electron dump plates

In order to estimate the heat power load deposited on the electron dump plates, the deterministic model explained in chapter 2 has been used. The calculation has been performed according to eq (17). In Figure 118 a top view for the DSS is shown, the red trajectories hit the plate for which the heat load power has been evaluated.

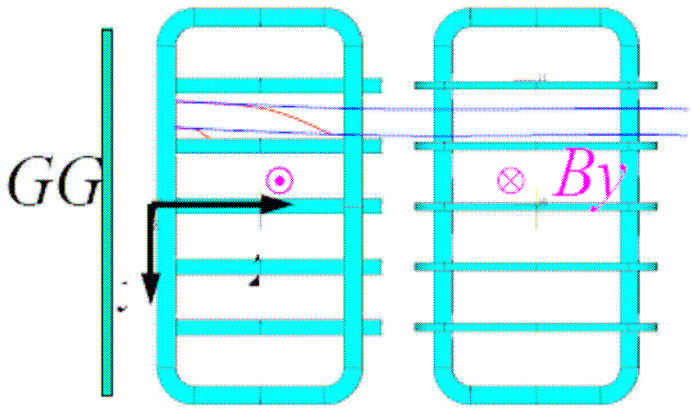

Figure 118 Top view for the double stage solution

Figure 119 shows the footprint map for the 5x16 array of beamlets: the mapped points appear bent, as the magnetic field (By), which deflects the electrons on the horizontal plane, is lower in the mid plane between the coils so the electron curvature radius is higher.

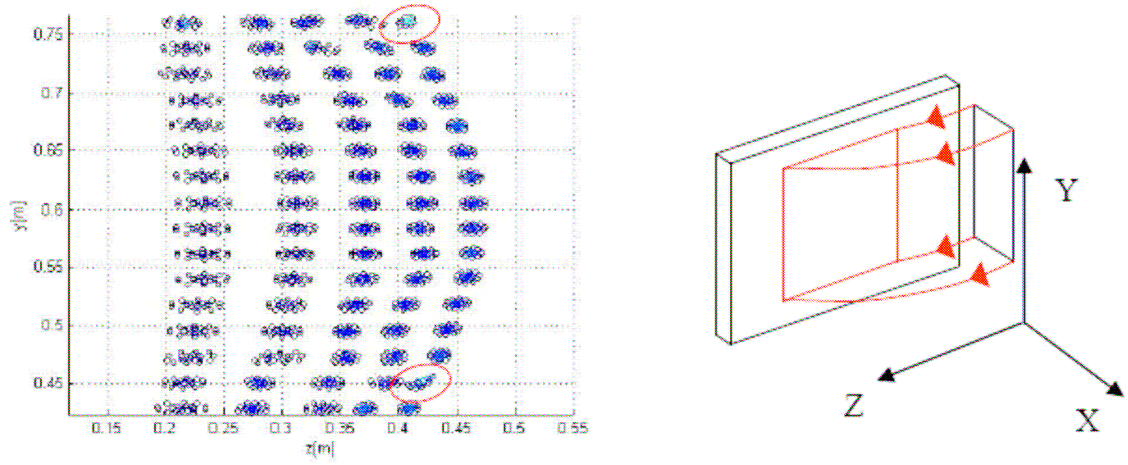

Figure 119 Power load deposited on the electron dump plate

In Figure 120 the map of the power load is shown. In the figure the two hot spots, highlighted in Figure 119 by the red circles, have been cut, these spots depend on the focalisation effect as shown in Figure 35 and by a non uniform magnetic field. The map shows that the remaining peaks in the power deposition are below 10 MW/m^2 i.e. compatible with the cooling system. It is worth noting that non uniformity and hot spots have been calculated with mono-energetic electrons at 1MV, so that a different energy distribution of the electrons is expected to spread the power load. In that sense a more detailed analysis can be performed adopting eq. (18) shown in chapter 2. Finally the optimisation of the magnetic configuration is expected to result in a better power load uniformity, possibly mitigating the hot spots.

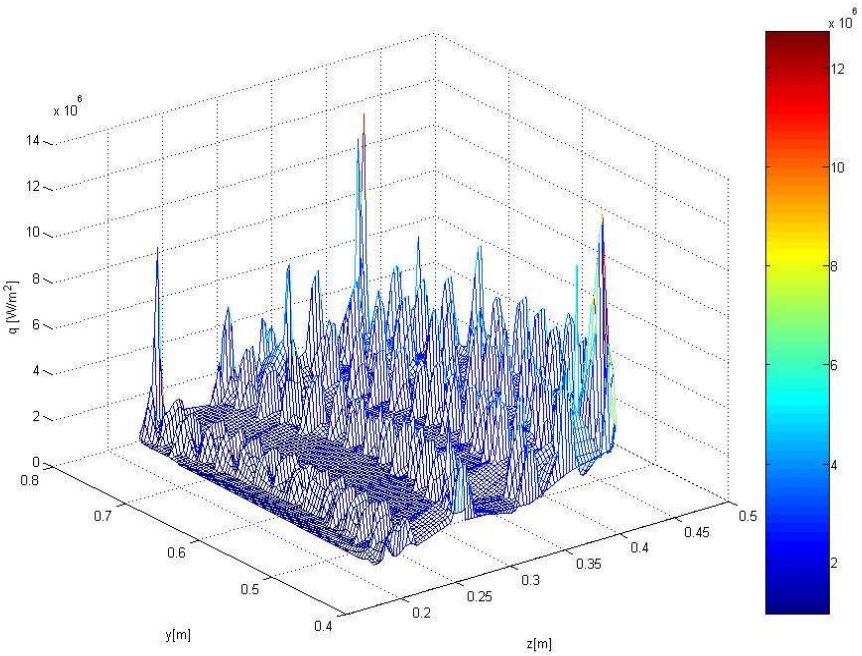

Figure 120 Heat flux on an electron dump plate

5.8 Feasibility and remaining issues for the EDSS

Two concepts for an active steerer have been studied: a Single Stage Steerer (SSS) and a Double Stage Steerer (DSS). Both concepts have been demonstrated to fulfil the beam deflection requirements and to be feasible. In both cases the system shows several advantages and appears to be more flexible if compared with a non active system. In particular:

- No mechanical tilting and positioning for vertical steering are required to the Beam Source (BS), so that no flexible connections between bushing and BS must to be developed and implemented.
- The electrons can be efficiently removed from the negative ion beam reducing the risk of re-ionisation inside the neutralizer and the associated heat power deposited on the dump plates can be removed by a cooling system.
- A higher operational flexibility with respect to the solutions based on permanent magnets (in particular for operations with voltages different from the nominal one) can be achieved.
- The iron yoke necessary to confine the magnetic field screens the cryopanel from heat and secondary electrons emitted by the plates.

In the case of the Single Stage Steerer (SSS), in order to deflect only the electrons it is necessary to rotate the ion source by a suitable angle. In Figure 121, two different source rotations by an angle $\alpha 1$ are compared. In both cases the system allows the ions to be accelerated along the axis z towards the confined plasma. As shown in the figure, the main impact is on the location and incidence angle of electrons deflected towards the plates. For the scheme "a", with an angle $\alpha 1$ lower than the scheme "b", the electrons impact on the plate with a smaller angle so that the heat flux is spread over a larger surface. On the other hand the scheme "a" requires longer plates.

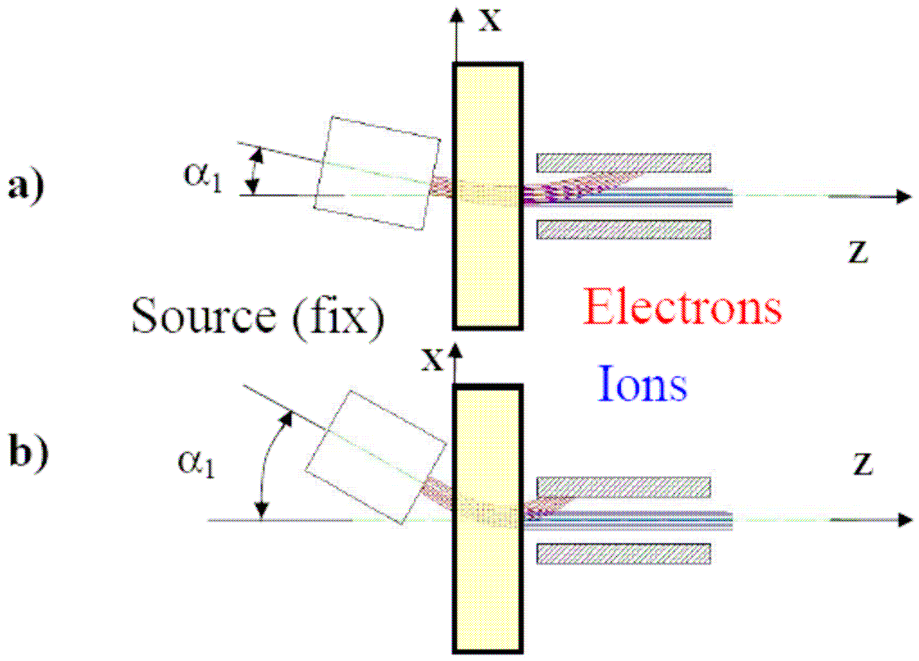

Figure 121 Two configurations with different source rotation

An optimum angle $\alpha_1 \approx 12$ mrad results the best trade-off between the overall dimensions of the system and the heat flux deposited on the plates.

As far as the double Stage Stereer is concerned, the higher complexity is compensated by a better flexibility; actually the main advantage is the possibility to work with ion energy different from the nominal one. The two stages of coils for horizontal deflection can always produce a suitable magnetic field to accommodate both ions and electrons.

In conclusion, the main drawbacks of the SSS are the overall dimensions and the limited flexibility in case of different acceleration voltages. Moreover, in the case of ITER an ion source rotated with respect to the other Beam Line Components could result in difficult installation mounting and poor accessibility for maintenance.

The successive steps in the EDSS design should consider another important aspects: first of all the evaluation of the decreased conductance between cryopanels and beam source is necessary not only to verify the pressure profile inside the accelerator, but also to evaluate the gas density level inside the steerer. In case of high density, the stripping reactions could enhance neutralization before the action of the magnetic field; in this case aberration of the negative ion beam can result.

Conclusions

This Doctorate Thesis has presented models studied and analyses addressed to design the electrostatic accelerator for the ITER Neutral Beam Injector.

The voltage holding and the negative ion beam acceleration issues are considered the most demanding to converge toward a reliable electrostatic accelerator design.

The ceramic components needed to insulate the multistage accelerating grids are certainly among the most critical: they has been analysed from the structural point of view. Two aspects have been treated: the first one concerned the studies and application of the design criteria for brittle components by a statistical approach, the second one the R&D activities related to the fabrication of large ceramic insulated rings brazed on metallic plates. These studies led to develop an ANSYS® routine to estimate the failure probability during the brazing process.

The insulations system has been also investigated from the point of view of the voltage holding capability. The high voltage electrostatic accelerator is insulated by vacuum; the investigation was oriented to understand the physics processes behind the high voltage holding in vacuum, in order to adopt reliable design criteria for large gap, multi-electrode high voltage vacuum devices. Moreover, the statistical approach used to evaluate the failure probability for the brittle materials has been proposed and adapted to estimate the breakdown probability of a complex multi electrode system. The research activity concerning the voltage holding issues has been completed by the participation to the MAMuG experiments at the JAEA Megavolt Test Facility in Naka (Japan), with particular involvement in high voltage conditioning, measurements and related operational issues.

Concerning the beam acceleration, numeric simulations of charged particle dynamics are important not only to predict the negative ion beam quality but also to carry out the accelerator design; in this context, a Monte Carlo code was adopted to benchmark the experimental results obtained at the Megavolt Test Facility in SINGAP configuration. Moreover, a new code IRES has been developed in order to integrate the equations of motion for charged particles, also considering the beamlet-beamlet interaction due to the spatial charge.

Finally, the need to filter the high electron flux produced inside the accelerator and the requirements of beam steering were considered in the conceptual design of an active magnetic steering system; an ANSYS® subroutine has been developed and applied to estimate the heat flux deposited on an electron dump plate by a deterministic method.

Acknowledgements

There are many people that I wish to thank for valuable help they gave me during the course of my PhD. It was overall a great experience for me, I learned a lot in many areas and this work confirmed my deep passion for science in general. My great thanks to the RFX NBI group: physicists and engineer, involved in the NBI project have given me the opportunities to develop my proposals contributing to sustain my ideas.

I wish to thank the NBI Group of Naka to give me a kind hospitality in Japan and for the fruitful experience that I spent participating at the experimental campaign and attending the group meetings.

I wish thank the others colleagues Phd students keen on research, they spent with me a lot of time, discussing and helping me to carry out my activities.

I would dedicate this work to all the young guys that want begin the scientific research way following their passion and enjoying to organize the knowledge in elegant and fruitful formulations.

Padova, January 2009

Nicola Pilan

Appendix A

The triple junction can be schematised with different levels of accuracy. Figure 122 shows three possible approaches to carry out the finite element analyses.

a)

b)

c)

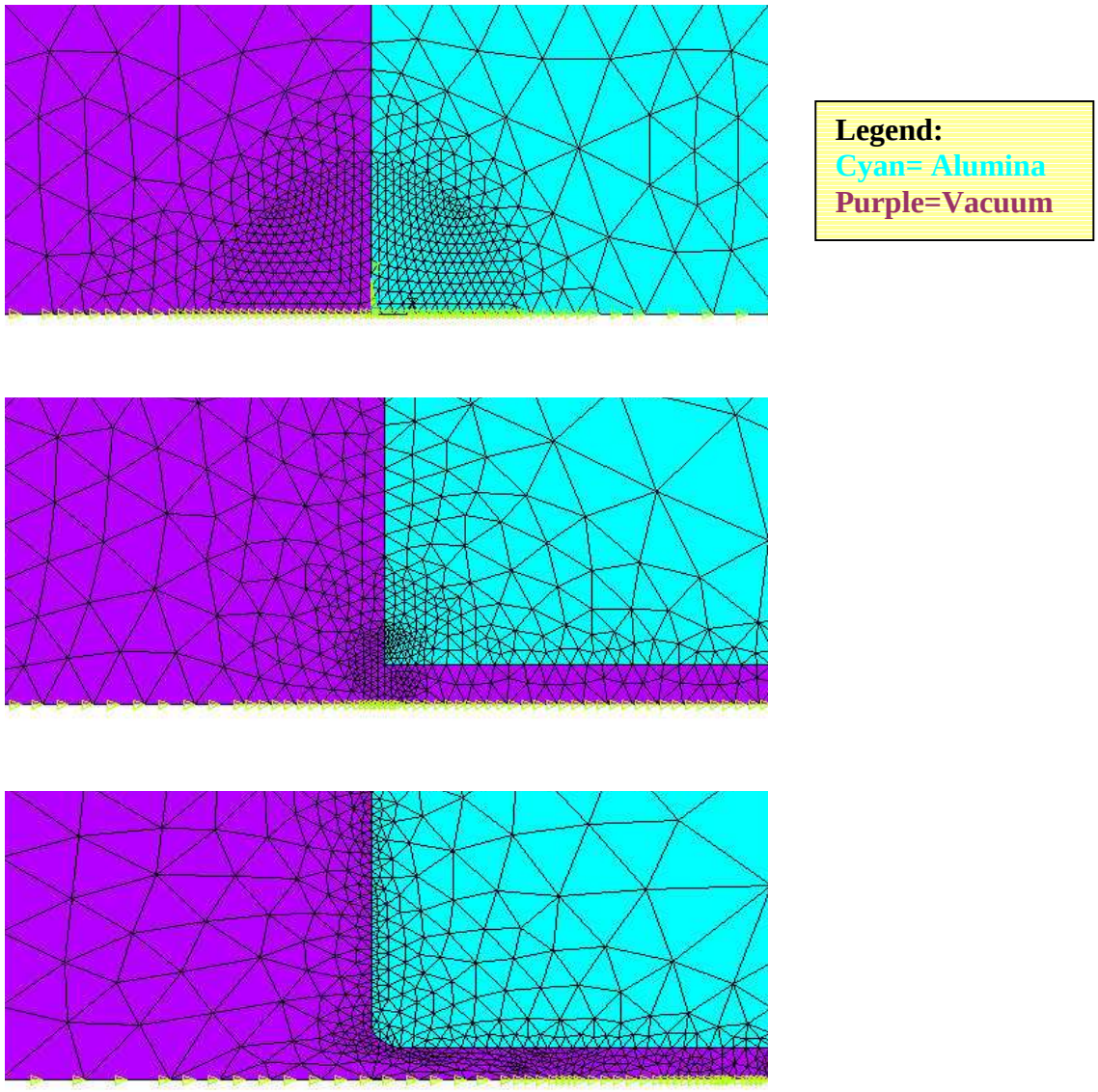

Figure 122 Three meshes used to estimate the electric field on the triple junction by FEM

The presence of a singularity in the interface between insulator and vacuum should be carefully considered for the Finite Element Analyses.

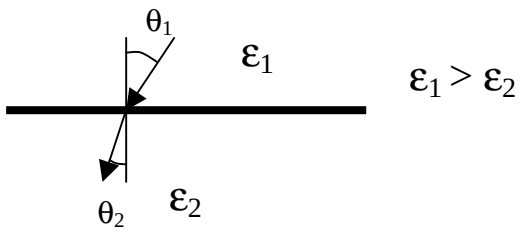

Figure 123 Changing of direction for the electric field through an interface

The sketch shown in Figure 124 illustrates a case where the numerical model finds a singularity at point "A": this is due to the well-known relationship $\frac{\tan\theta_1}{\tan\theta_2} = \frac{\varepsilon_1}{\varepsilon_2}$ sketched in fig. 122, and to the sharp interface corner. When $B \to A$ and $C \to A$, we should have in Figure 124 both $\theta_1 + \theta_1^I \to \pi/2$ and $\theta_2 + \theta_2^I \to \pi/2$, but these constraints are not consistent with the permittivity relationship. In other words, the FEM for this case is mesh-sensitive.

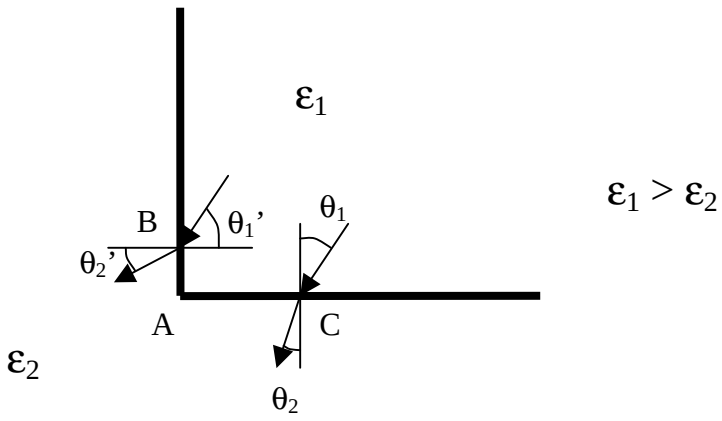

Figure 124 An example of numerical singularity in the electric field computation

This means that the local FE model of Figure 122-a, must not only take into account the little gap between the materials, but also it should consider the "real" fillet radius on the corner as shown in Figure 122-c; unfortunately, the accuracy of the analysis is poor because the little gap, and the local geometry, are difficult to fix in the design phase or to measure.

For these reasons, these more sophisticated meshes do not significantly improve information, so it is suggest to treat the triple points as shown in Figure 122-a.

Bibliography

[1] http://www.efda.org.

[2] http://en.wikipedia.org/wiki/Magnetic_confinement_fusion

[3] P. Caldirola, Pozzoli Roberto, Sindoni Elio, *Il fuoco della fusione termonucleare controllata,* Mondadori 1984

[4] E. Speth et al. *Overview of the RF source development at programme at IPP Garching* Nucl. Fusion 46 (2006) 220-238

[6] http://www.ipp.mpg.de/ippcms/eng/for/bereiche/technologie/projekte/nbi.html

[7] M. Hanada, M. Kashiwagi, T. Inoue, K. Watanabe, and T. Imai. *Experimental comparison between plasma and gas neutralization of high-energy negative ion beams*. Rev. Sci. Inst. 75 (2004) 1813-1815.

[8] J. Pamela. *The physics of production, acceleration and neutralization of large negative ion beams*. Plasma Phys. Control. Fusion 37 (1995) 325-336.

[9] T. Inoue, M. Taniguchi, T. Morishita, M. Dairaku, M. Hanada, T. Imai, M. Kashiwagi, K. Sakamoto, T. Seki and K. Watanabe. *R&D on a high energy accelerator and a large negative ion source for ITER*. Nucl. Fusion 45 (2005) 790-795.

[10] Y. Takeiri, O. Kaneko, K. Tsumori, Y. Oka, K. Ikeda, M. Osakabe, K. Nagaoka, E. Asano, T. Kondo, M. Sato and M. Shibuya. *High-power and long-pulse injection with negative-ion-based neutral beam injectors in the Large Helical Device*. Nucl. Fusion 46
(2006) 119-210.

[11] Y. Ikeda, N. Umeda, N. Akino, N. Ebisawa, L.Grisham, M. Hanada, A. Honda, T. Inoue, M. Kawai, M. Kazawa, K. Kikuchi, M. Komata, K. Mogaki, K. Noto, F. Okano, T. Ohga, K. Oshima, T. Takenouchi, Y. Tanai, K. Usui, H. Yamazaki and T. Yamamoto. *Present status of the negative ion based NBI system for long pulse operation on JT-60U*. Nucl. Fusion 46 (2006) 211-219.

[12] R. S. Hemsworth, J.-H. Feist, M. Hanada, B. Heinemann, T. Inoue, E. Kussel, A. Krylov, P. Lotte, K. Miyamoto, N. Miyamoto, D. Murdoch, A. Nagase, Y. Ohara, Y. Okumura, J. Paméla, A. Panasenkov, K. Shibata, M. Tanii, and M. Watson. *Neutral beams for ITER*. Rev. Sci. Instrum. 67, Issue 3, 1120 (1996).

[13] P.L. Mondino, P. Bayetti, E. Di Pietro, R.S. Hemsworth, H. Iida, T. Inoue, K. Ioki, G. Johnson, A.I. Krylov, V.M. Kulygin, P. Massmann, K. Miyamoto, Y. Okumura, A.A. Panasenkov, R.T. Santoro, M. Sironi, Y. Utin, K. Watanabe and M. Yamada. *ITER neutral beam system*. Nuclear Fusion, Vol. 40, No. 3Y.

[14] P. Franzen, U. Fantz, W. Kraus, H. Falter, B. Heinemann, R. Nocentini and the NNBI Team *Physical And Experimental Background Of The Design Of The ELISE Test Facility,* Proceedings of the NIBS conference , 2008

[15] M. Hanada, M. Kashiwagi, T. Morishita, M. Taniguchi, Y. Okumura, T. Takayanagi and K. Watanabe. *Development of negative ion sources for the ITER neutral beam injector*. Fusion Eng. Des. 56 (2001) 505-509.

[16] P. Franzen, H.D. Falter, U. Fantz, W. Kraus, M. Berger, S. Christ-Koch, M. Fröschle, R. Gutser, B. Heinemann, S. Hilbert, S. Leyer, C. Martens, P. McNeely, R. Riedl, E. Speth and D. Wünderlich. *Progress of the development of the IPP RF negative ion source for the ITER neutral beam system*. Nucl. Fusion 47 (2007) 264-270.

[17] W. Kraus, P. McNeely, P. Franzen, A. Entscheva, M. Bandyopadhyay, B. Heinemann, R. Riedl, E. Speth and R. Wilhelm. *Development of large RF driven negative ion sources for neutral beam injection*. Fusion Eng. Des. 66-68 (2003) 491-495.

[18] W. Kraus, B. Heinemann, H.D. Falter, P. Franzen, E. Speth, A. Entscheva, U. Fantz, T. Franke, D. Holtum, Ch. Martens, P. McNeely, R. Riedl and R. Wilhelm. RFsource development for ITER: *Large area H- beam extraction, modifications for long pulse operation and design of a half size ITER source*. Fusion Eng. Des. 74 (2005) 337-341.

[19] Y. Okumura, M. Hanada, T. Inoue, M. Mizuno, Y. Ohara, Y. Suzuki, H. Tanaka, M. Tanaka, and K. Watanabe. *Long pulse operation of a cesium-seeded multicusp H- ion source.* Rev. Sci. Instrum. Vol. 64, No. 3, April (1992).

[20] http://www.fieldp.com/cpa.html

[21] H.P.L. de Esch, *A new pre-accelerator for SINGAP based on a 3 mm wide extraction gap* , 6 August 2001 CEA Report

[22] H.P.L. de Esch, R.S. Hemsworth and P. Massmann. *SINGAP: the European concept for negative ion acceleration in the ITER neutral injectors*. Rev. Sci. Inst. 73 (2002) 1045.

[23] H.P.L. de Esch, R.S. Hemsworth and P. Massmann. *Updated physics design ITERSINGAP accelerator*. Fusion Eng. Des. 73 (2005) 329.

[25] ITER_Baseline_Documentation *DDD 5.3 Neutral_beam_H&CD*

[26] H.P.L. de Esch, *SINGAP operation* Mission report 41 for Naka

[28] E. Zilli *Elementi di fisica del plasma*

[29] H.P.L de Esch, et. al., S*INGAP: the european Concept for Negative Ion Acceleration in the Neutral Beam Injector,* Rev.Sci. Inst. 73 (2002) 1045.

[30] M. Kashiwagi, T. Inoue, L.R. Grisham, M. Hanada, M. Kamada, M. Taniguchi, N. Umeda and K. Watanabe, *Compensation of beamlet repulsion in a large negative ion source with a multi aperture accelerator,* Proceedings of the NIBS conference , 2008

[31] T. Inoue, M. Kashiwagi, M. Taniguchi, M. Dairaku, M. Hanada, K. Watanabe and K. Sakamoto *1 MeV, ampere class accelerator R&D for ITER,* Nucl. Fusion 46 S379-S385

[32] E. Buckingham *On Physically Similar Systems; Illustrations of the Use of Dimensional Equations* Phys. Rev. 4, 345 - 376 (1914)

[33] Townsend, J. S. 1947, *Electrons in Gases* (London: Hutchinson).

[34] T. Inoue, M. Taniguchi, T. Morishita, M. Dairaku, M. Hanada, T. Imai, M. Kashiwagi, K. Sakamoto, T. Seki and K. Watanabe *R&D on a high energy accelerator and a large negative ion source for ITER* 2005 Nucl. Fusion 45 790-795

[35] P. Spolaore, G. Bisoffi, F. Cervellera, R. Pengo and F. Scarpa, *The Large Gap Case for the HV Insulation in Vacuum,* IEEE Transaction on Dielectrics and Electrical Insulation Vol. 4 No.4, August 1997

[36] R. H Fowler and L. Nordheim, *Electron Emission in Intense Electric Fields*, Proc. Roy.Soc. Vol.A119, pp. 173-181,1928.

[37] M. Cavenago, V. Antoni, F. Sattin, A. Tanga, *Analysis of Multigrid Extraction Plasma Meniscus Formation*. Proceeding of 2005 Particles Accelerator Conference Knoxville Texas

[38] L. Cranberg, *The Initiation of Electrical Breakdown in Vacuum Journal of Applied Physics* May 1952 Vol. 23, N. 5

[39] F. M. Charbonnier, *A brief review of a vacuum breakdown initiation processes* Proc. of the 3rd Int. Symp. on Discharges and Electrical Insulation in Vacuum, Paris, Septemper 1968.

[40] K. Watanabe, M. Mizuno and Y. Ohara, *DC voltage holding of vacuum gap for high-energy ion sources* J. Appl. Phys. 72 (9) , 1 November 1992

[41] G. A. Farral *Electrical breakdown in vacuum* IEEE Transaction on Insulation Vol. EI No. 5, October 1985

[42] C. Germain and F. Rorhbach, *High Voltage breakdown in vacuum*. Vacuum Vol. 18 number 7 Pergamon Press Ltd/ Printed in Great Britain

[43] F. Rohrbach, *Isolation sous vide* CERN report 71-5 1971

[44] H. Toya, N. Ueno, T. Okada, Y. Murai, *Statistical property of breakdown between metal electrodes in vacuum* IEEE Transaction on Power Apparatus Systems, Vol.4, No. 4, April 1981.

[45] F.Rohrbach *Pre-Breakdown currents and microdischarges across large gaps in clean vacuum* Proc II, p. 83 (1966)

[46] M. Cavenago, V. Antoni, R. Cavazzana, A. Masiello, N. Pilan, S. Petrenko, F. Sattin, G. Serianni, M. Spolaore, P. Zaccaria *Steering of large size ion beams for NBI,* Comsol Conference, 23-24 October 2007, Grenoble.

[47] P. Agostinetti, S. Dal Bello, M. Dalla Palma, P. Zaccaria. *Thermo-mechanical design of the SINGAP accelerator grids for ITER NB Injectors.* Fusion Eng. Des. 82 (2007) 860-866.

[48] M. Taniguchi et al. *Development of 1 MeV H- accelerator at JAEA for ITER NB*, to be published in Conf. Proc. of American Inst. Phys., 2008.

[49] U. Shumann, M. Kurrat, *Breakdown voltage of electrode arrangements in vacuum in consideration of surface area* 20th International Symposium on Discharges and Electrical Insulation in Vacuum Tours 2002

[51] Rod Latham High Voltage Vacuum Insulation, Basic Concepts and Technological practice ACADEMIC PRESS 1995 London

[52] P. Agostinetti, *Overview on the magnetic configuration of negative ion sources*, Consorzio RFX, internal presentation 2008.

[53] A. Masiello*, Adaptation of the 1MV Bushing to the SINGAP Concept for the ITER NB Injector Test Bed*, Nuclear Fusion, 2006

[54] H. P. L. de Esch. *Private comunications*

[55] De Esch H.P.L et al. "Results of the SINGAP neutral beam accelerator experiment at JAEA", to be published to Fusion Eng. Design.

[56] G. Fubiani, H. P. L. de Esch, and A. Simonin *Modeling of secondary emission processes in the negative ion based electrostatic accelerator of the International Thermonuclear Experimental Reactor,* Physical Review Special Topics - Accelerator and beams 11, 014202

[57] P. Stanley, A.D. Sivill, H. Fessler, *Applications of the four function Weibull equation in the design of brittle components,* Fracture Mechanics of Ceramics – Flaws and Testing, Vol. 3, Plenum Press, New York, 1978, pp. 51-66

[58] Weibull W. *A statistical Theory of the Strength of Material.* In: Ingeniors Vetenskap Akademiens, Handlinger, Stockholm, Sweden, 1939, No. 151, 1-45.

[59] J.L. Chermant, A. Descanvres and F.Osterstock, *Toughness and fractography of Tic and WC* Fracture Mechanics of Ceramics – Flaws and Testing, Vol. 4,Plenum Press, New York, 1978, pp. 891-901

[60] L.M. Barker, *Short rod KIC measurements of Al_20_3*, Fracture Mechanics of Ceramics – Flaws and Testing, Vol. 3 ,Plenum Press, New York, 1978, pp. 483-494

[61] D.B. Bogy, *Two edge bonded elastic wedges of different materials and wedge angles under surface traction,* Journal of Applied Mechanics, Vol.38 , pp. 377-386, 1971

[62] Wellman G. W. *FAILPROB--A Computer Program to Compute the Probability of Failure of a Brittle Component*. Sandia Report, No. SAND2002-0409.

[63] M. Hanada, T. Inoue, M. Kashiwagi, M. Taniguchi, H. Tobari, K.Watanabe, N. Umeda, M. Dairaku, Y. Ikeda and K. Sakamoto *R&D progress at JAEA towards production of high power and large-area negative ion beams for ITER* Nucl. Fusion 47 (2007) 1142–1146

[64] A. Krylov et al., AIP Conference Proceedings, 439, (1998) 199.

[65] Marco Cavenago, Pierluigi Veltri, Fabio Sattin, Gianluigi Serianni, and Vanni Antoni, *Negative Ion Extraction With Finite Element Solvers and Ray Maps*. IEEE Transaction on plasma sience , Vol.36, No. 4, August 2008.

[66] Gymesi,Mikolos,Zhulin,Vladimir and Ostergaard, Dale, *Particle Trajectory Tracing in ANSYS*, Fifth International Conference on Charge Particles Optics, Delft University, Netherlands. To be published in Nuclear Instruments and Methods in Physics Research, Section A (1998).

[67] prEN (euro norm) 843-5 (draft): *Advanced technical ceramics – Monolithic ceramics. Mechanical properties at room temperature – Part 5: Statistical analysis*

[68] CEI EN 60672-1: Ceramic and glass insulating materials – Part 1*: Definition and classification*

[69] CEI EN 60672-2: Ceramic and glass insulating materials – Part 2: *Method of test*

[70] CEI EN 60672-3: Ceramic and glass insulating materials – Part 3: *Specification for individual materials*

[71] prEN 843-1 (draft): Advanced technical ceramics – Monolithic ceramics. Mechanical properties at room temperature – Part 1: *Determination of flexural strength*

[72] prEN 843-2 (draft): Advanced technical ceramics – Monolithic ceramics. Mechanical properties at room temperature – Part 2: *Determination of Young's modulus, shear modulus and Poisson's ratio*

[73] UNI ENV 1006: Advanced technical ceramics – Monolithic ceramics – *Guidance on the selection of test pieces for the evaluation of properties*

[74] CEN/TS 14425-3: Advanced technical ceramics – Test methods for determination of fracture toughness of monolithic ceramics – Part 3: *Chevron notched beam (CNB) method*

[75] CEN/TS 14425-5: Advanced technical ceramics – Test methods for determination of fracture toughness of monolithic ceramics – Part 3: *Single-edge notch beam (SEVNB) method*

[76] ISO 17562: Fine ceramics (advanced ceramics, technical ceramics) – *Test method for linear thermal expansion of monolithic ceramics by push-rod technique*

[77] UNI EN 820-3: Advanced technical ceramics – Methods of testing monolithic ceramics – Thermo-mechanical properties – Part 3: *Determination of resistance to thermal shock by water quenching*

[78] H. Toya, N. Ueno, T. Okada, Y. Murai, *Statistical property of breakdown between metal electrodes in vacuum* IEEE Transaction on Power Apparatus Systems, Vol.4, No. 4, April 1981.

[79] K. Watanabe et al. *Development of a large volume negative ion source for ITER neutral beam injector* Review of scientific Instrument Vol. 73, No. 2 , February 2002